Title
Measuring and Improving the Properties of Magnetic Nanoparticles.

Author
Kurish, Jeffrey Alexander

Publication Date
2022

Peer reviewed|Thesis/dissertation

UNIVERSITY OF CALIFORNIA

Los Angeles

Measuring and Improving the Properties of Magnetic Nanoparticles.

A dissertation submitted in partial satisfaction

of the requirements for the degree Doctor of Philosophy in Chemistry

by

Jeffrey Alexander Kurish

2022

ABSTRACT OF THE DISSERTATION

Measuring and Improving the Properties of Magnetic Nanoparticles.

by

Jeffrey Alexander Kurish

Doctor of Philosophy in Chemistry

University of California, Los Angeles, 2022

Professor Sarah H. Tolbert, Chair

Magnetic nanoparticles show promise in a vast array of devices that utilize control of nano magnetism. For these devices to properly function, the magnetic properties of the nanomaterials must be precise and uniform across the synthesized materials. The focus of the work that is presented here is to develop ways of characterizing nanoparticles to better understand the materials. Further to the work is to show how to create improved nanoparticles which can be used in eventual nanoscale magnetic devices.

The first three chapters of this work show ways to improve the nanoparticle materials used in eventual nanoparticle based magnetic devices. Chapter one is concerned with improving a method for adhering nanoparticles to surfaces to later manipulate their magnetic moments. The method alters a synthetic method for nickel nanoparticles to remove a phosphorus impurity allowing for an air-free adhesion method. Thus, the method avoids oxidation damage to the nanoparticle magnetic properties. The second chapter displays the development of a new nanoparticle synthetic method for cobalt ferrite nanoparticles. The new method improves size dispersity and shows a higher degree of size control. Further, the magnetic properties of these crystals are shown to be superior. The third

chapter shows the adaptation of a known magnetostrictive material galfenol, an iron gallium alloy, into a nanoparticle. This is the first synthesis of such a material as a processable solution nanoparticles and is shown to be able to be adhered to surfaces using the methodology in chapter 1.

The remainder of the chapters of this work are methodologies of measuring nanoparticles to generate a better understanding of the structure of those nanoparticles and how this can help improve magnetic nanoparticle systems downstream. Chapter 4 involves using combined surface sensitive and bulk stoichiometry measurements to create a picture of the nanoparticle atomic distribution. The example system of annealing of FePt nanoparticles is used to show the value of this method. Finally in Chapter 5 a novel mathematical fitting of nanoparticle anisotropy distributions is shown. This method is used to calculate a temperature dependent anisotropy constant inherent to the chemical structure of the nanoparticles revealing important information about the synthetic process. Further surface and shape anisotropies are propped to provide a fuller picture of nanoparticle quality and thus understand methods of improving synthesis.

The dissertation of Jeffrey Alexander Kurish is approved.

Gregory P. Carmen

Justin R. Caram

Louis S. Bouchard

Sarah H. Tolbert, Committee Chair

University of California, Los Angeles

This thesis is dedicated to Amy Lai for her endless support and for making the graduate school journey worthwhile.

TABLE OF CONTENTS

LIST OF TABLES AND FIGURES

represent an hour of synthesis whereas b) shows three hours of synthesis. Conventional particles presented are the same in each graph.

Figure 2.3. a) Average nanoparticle size as a function of time as determined by aliquot removal from an ongoing synthesis. All esterification based synthetic methods show continuous growth of nanoparticles over a long period. Growth is not affected by scale up of method. b) Time dependent volume growth of nanocrystals over time in both 180°C and 200 °C synthetic methods. At 180 °C growth follows a continuous kinetic-limited process within the studied region. For 200°C nanocrystal growth is linear but slows due to limited reagent.

Figure 2.4. a) TEM of CFO nanoparticles after heating seed CFO nanoparticles at 180° C for 30 minutes in a precursor solution with no decanol present. Most visible particles are large with some very small new particles being visible. b) TEM of CFO nanoparticles after heating seed CFO nanoparticles at 200° C for 30 minutes in a precursor solution with no decanol present. Some visible particles are large but the majority are very small new particles. c) Size histograms on a logarithmic scale through imageJ analysis of TEM images of nanoparticles generated through heating of seeds at 180° C or 200° C in oxo-metallic precursor solution as well as size histogram of the initial seed distribution. Distribution shows 200°C heating preference for nucleation and 180° C preference for growth.

Figure 2.5. a) Example FC and ZFC curves of nanoparticles synthesized through esterification at 180°C b) FC-ZFC curve (black) showing cumulative population distribution of un-blocked nanoparticles. Derivative curve (blue) showing population of blocking temperatures in an example sample.

Figure 2.6. d(ZFC-FC)/dT graphs are shown from SQUID magnetometry of three representative samples of conventional(a) esterification of CFO stoichiometry at 200° C (b) 180°C off stoic esterification (c) and 200°C stoichiometric CFO esterification synthesis(d). Fitting functions have been

applied to each of the curves in order to glean the average blocking temperature of the sample. The two peaks in conventional correspond to two peaks in the volumetric distribution and therefore have two average blocking temperatures and two anisotropy constants.

Figure 3.1 a),b) TEM of FeGa nanoparticles showing low dispersity of size. EDS confirms particles are $Fe_{0.9}Ga_{0.1}$ c) Histogram of nanoparticle diameters determined through imageJ d) XRD of synthesized particles

Figure 3.2 a) MH loops of as synthesized nanocrystals suspended n paraffin wax. At room temperature the particles are clearly superparamagnetic with no detectable coercivity. At 5K the ferromagnetic particles show a coercivity of around 500 oe. b) Zero field cooled (black) and field cooled (red) curves for $Fe_{0.9}Ga_{0.1}$ Particles. The ensemble blocking temperature from ZFC is 65K. blocking temperature distribution (-d[FC-ZFC]/dT) shows an average blocking temperature at 49K and a narrow distribution of blocking temperatures indicating good chemical uniformity of particles.

Figure 3.3 MH loops of nanoparticles after adhesion to a titania surface on a silicon substrate. a) a comparison of the as synthesized nanoparticles (red) and an in-plane measurement of the nanoparticles on a substrate. as synthesized nanoparticles are superparamagnetic, however, adhered particles have noticeable coercivity. b) comparison of magnetic properties in-plane and out-of-plane. The adhered particles show a preferential axis in plane.

Figure 4.1 XPS results for heat up method synthesized FePt nanoparticles. Despite EDS measurements showing the nanoparticles are 1:1 Pt:Fe, the XPS results show only 9% Pt against 91% Fe implying a core shell structure.

Figure 4.2 XPS results for hot injection method synthesized FePt nanoparticles. Despite EDS measurements showing the nanoparticles are 1:1 Pt:Fe, the XPS results show 38% Pt against 62% Fe much closer to a true randomized alloy.

Figure 4.3 a) TEM images of FePt nanoparticles showing small size dispersity and size. b) XRD pattern for FePt nanoparticles showing <111> and <200> peak clearly.

Figure 4.4 d(ZFC-FC)/dT graph for nanoparticles generated through a heat up method (black) vs a hot injection method (red). The hot injection method shows predominately one single peak of anisotropies implying one nanoparticle product, whereas the heat up method shows two clear peaks at extremely low temperature and another near 200K. This implies that in heat up methods multiple anisotropies exist due to the more complicated system of a core shell nanoparticle.

Figure 4.5 a) M-H loop out of plane of nanoparticle sample annealed at 550° C. Black curve is raw data showing 10kOe coercivity. Fitting of superparamagnetic unconverted signal (red) and ferromagnetic signal (blue) reveals true coercivity of ferromagnetic particles is ~13kOe and that conversion is 85%. b) results of annealing studies compared to literature values of nanoparticles synthesized via methods described by Sun et al. Hot injection nanoparticles show much lower required annealing temperatures.

Figure 5.1 a) Example zero-field cooled (ZFC) (black) and field cooled (FC) (red). Blocking temperature for a polysized sample is at the peak of the ZFC curve. b) Difference between FC and ZFC curve shown in a). Derivative curve of the difference curve is shown in blue. Average blocking temperature of the nanoparticles in the ensemble is the peak in this curve. Determination of blocking temperature through this method results in a much lower calculated blocking temperature than in the curve from a.

Figure 5.2. a) example TEM image of low temperature cobalt ferrite nanocrystals with low size dispersion and small size. b) high example TEM image of high temperature cobalt ferrite nanocrystals. Crystals remain small while having higher dispersity. C) XRD representative of those for CFO nanoparticle synthesis. d) TEM image of low temperature nickel nanocrystals after exposure to air. E TEM image of high temperature nickel nanocrystals after exposure to air.

Additional TEM images in justification of size distributions are available in the SI. f) XRD representative of both Ni nanoparticle data sets. Front shoulder of <111> peak is indicative of a semi crystalline. nickel oxide shell formed from air exposure.

Figure 5.3. a) ZFC(black) FC(red) and -d(FC-ZFC)/d*T* (blue) curve for low temperature CFO nanocrystal distribution. Despite the small size of the crystals the curve is broad and at a high average blocking temperature of 183K. The curve is noticeably not lognormal in shape. b) ZFC(black) FC(red) and -d(FC-ZFC)/d*T* (blue) curve for low temperature Ni nanocrystal distribution. The large nanocrystals have lower anisotropy and so peak occurs at 62K.

Figure 5.4. a) Fitting -d(FC-ZFC)/*dT* curve data by use of a log normal function where volume is calculated using equation 1. Blue curve uses the calculated average anisotropy constant of the distribution whereas the red curve the anisotropy constant is allowed to change to best fit the data. b) successful fitting of the same data set by use of a combined equation.

Figure 5.5. a) Fitting -d(FC-ZFC)/*dT* curve of stoichiometrically precise CFO from low temperature synthesis by use of a temperature dependent fitting function. b) Fitting -d(FC-ZFC)/*dT* curve of low cobalt CFO from low temperature synthesis by use of a temperature dependent fitting function.

Figure 5.6. a) Fitting -*d*(FC-ZFC)/*dT* curve of stoichiometrically precise CFO from low temperature synthesis by use of a temperature dependent fitting function. b) Fitting -*d*(FC-ZFC)/*dT* curve of stoichiometrically precise CFO from low temperature synthesis by use of a temperature dependent fitting function.

Figure 5.7. a) Fitting -*d*(FC-ZFC)/*dT* curve of nickel nanoparticles from low temperature synthesis by use of a temperature dependent fitting function. (blue) and the same function but with a shape anisotropy term added. b) Fitting -*d*(FC-ZFC)/*dT* curve of the same nickel np data, but with a

function including both surface and shape anisotropy with temperature dependent MCA. The fit is greatly improved in the green curve.

Figure 5.8 Size histogram for Low Temperature Nickel Nanocrystals showing the total distribution of sizes as well as the distribution of sizes for the data set split into four quadrants defined by aspect ratio. 1st quadrant being the 25% lowest aspect ratio particles of the original distribution etc. to the highest 25% aspect ratio in quadrant 4. All size distributions appear nearly identical meaning the same volumetric fitting function can be applied ubiquitously

Figure 5.9. a) Fitting -d(FC-ZFC)/*dT* curve of nickel nanoparticles from low temperature synthesis as in figure 5.7b with both temperature dependent and shape/surface additions. b) Fitting -d(FC-ZFC)/*dT* curve of high temperature nickel synthesis, with the same functional forms as low temperature.

ACKNOWLEDGEMENTS

I would like to thank all the people who were essential to my life as a scientist. I must acknowledge my first and best teacher, my mother, who taught me the most important lessons of all, how to read, how to seek out and find knowledge and where my knees are. Also, I have to thank my father for a sense of balance, but also for teaching me how to navigate the world of academia and for the sense of humor necessary for all of life. I'd like to thank my dog, Emby, for being a source of joy and normality during an otherwise difficult year. Finally, most importantly I must thank my wife, Amy Lai. Her endless support and our fantastic time together kept me going even when nothing else in graduate studies could motivate me. She put up with me coming home from SQUID measurements at 2 in the morning and somehow continues to put up with me today. I would not have made it through grad school without her, but now I have no regrets because of her.

I want to thank all the excellent faculty and scientist who have taught me so much to enable my studies here. My mentor, Dr. Stephen Sasaki, who's infectious attitude towards work continues to inspire me. Dr. Ignacio Martini who ran the Molecular Instrumentation Center and taught me how to use every instrument vital to my research, and even put up with my out of the box measurement ideas. I would also like to thank my excellent advisor, Sarah Tolbert, who taught me everything essential to the field of materials.

I want to especially thank the TANMS ERC and all the wonderful people there, especially Professor Greg Carmen who warned me to never listen to his advice, but still acts as a source of wisdom. Further, Michelle and Tsai-Tsai at TANMS for helping me immensely as I navigated being SLC president in my second year. As well, I want to thank many of the TANMS engineers for being tremendous sources of wisdom and help when trying to make viable samples.

Finally, I want to thank so many in the Tolbert lab that I cannot mention all of them specifically, but especially those who also endured magnetics research that I have not already mentioned—Ty Karaba, Shreya Patel, Kat Estoque and the undergraduates who helped me tremendously while putting up with my brand of mentorship style—Anica Pinongcos, and Sasha Gill- Ljunghammer. While I feel as though I am leaving the magnetics students in the trenches, I could not have made it through grad school without a sounding board to bounce ideas and opinions off of. Particularly, thank you to Shreya Patel who shared a great deal of my grad school experiences in both TANMS and the Tolbert lab.

My work here was supported by the NSF Nanosystems Engineering Research Center for Translational Applications of Nanoscale Multiferroic Systems (TANMS) under Cooperative Agreement Award EEC-116050

JEFFREY KURISH CURRICULUM VITAE

Education

PhD Candidate in Chemistry, University of California, Los Angeles — 2018 – present
MS in Chemistry, University of California, Los Angeles — 2016 – 2018
BS in Chemistry, Carnegie Mellon University — 2010 – 2014
summa cum laude, Minor in Chinese

Awards

ACS Division of Inorganic Chemistry Student Travel — May 2021

Publications

Covalent Bonding-Based Adhesion Method for Rigidly Coupling Metal Nanocrystals to Metal and Metal Oxide Surfaces. ACS Applied Nano Materials, Sasaki, S.; Kurish, J.; Robbennolt, S.; Yan, Y.; Garcia, E.; Tolbert, S. H. 2021, 4, 3426–3433.

Multiexcitation Fluorogenic Labeling of Surface, Intracellular, and Total Protein Pools in Living Cells. Bioconjugate Chemistry, Naganbabu, M.; Perkins, L. A.; Wang, Y.; Kurish, J.; Schmidt, B. F.; Bruchez, M. P. , 2016, 27, 1525–1531.

Tuning Exchange Coupling in a New Family of Nanocrystal-Based Granular Multiferroics Using an Applied Electric Field, S. S. Sasaki, O. G. Udalov, J. Kurish, M. Ishii , I. S. Beloborodov, S. H. Tolbert (approved)

Presentations

ACS National Meeting in San Diego, "Improving FePt/FePd nanoparticle synthesis for ease of magnetic processing" Aug 2019 (Oral Presentation)

2019 ERC Education, Culture of Inclusion, and Student Leadership Conference "Student Leadership as an Augmentation of Traditional Scientific Education" (Invited Talk)

2019 TANMS Student leadership Annual Retreat (Lead Retreat)

IMRC in Cancun 2018 "Student Leadership as an Augmentation of Traditional Scientific Education for the center for translational Applications of Multiferroic systems." (Invited Talk)

TANMS ERC 6th year NSF review, Student SWOT report (Oral Presentation)

TANMS Annual Research Strategy Meeting 2021, 2020(session chair), 2019, 2018 (poster)

Teaching Experience

Teaching Assistant, University of California, Los Angeles — 2016 – 2021

Organic Chemistry Laboratory II (30CL) F'16 F'17

General Chemistry for life Scientists (14A) W '17 W '21

General Chemistry Lab (20L) W'18

Materials Chemistry Laboratory (285) W'20

(Program for Excellence in Education Research in Sciences) Tutor: Gen Chem for Life Science II

TANMS Undergraduate Mentor Sp'19 Su '19, W '20

INTRODUCTION:

The creation of materials in the nano regime has led to profoundly unique emergent properties and thus countless recent developments. Many commonly understood physical properties of bulk materials fundamentally change when compressed into systems with countable numbers of atoms. This is particularly true of magnetic materials where the high surface area to volume ratio and increased degree of intersystem interaction inherent to nanoscale materials can cause a vastly altered menagerie of magnetic energies. Alteration of the relevant energy is particularly valuable to devices in a ferroic system, such as magnetism, where the property of the material is not linearly dependent on the application of a relevant field.

Outstanding among types of nano structures are magnetic materials that are nano in all dimensions; so called 0D materials or nanoparticles, have unique emergent properties even within the nanoscale regime. Magnetic nanoparticles below a material dependent threshold size become magnetically randomized by ambient thermal energy leading to a material that mixes different magnetic orderings in an exciting way. The magnetization of these materials has high saturation field propagation like a ferromagnetic material, but will align quickly to any applied external field like a paramagnetic material creating "superparamagnetism" Since the discovery of superparamagnetism, scientists have sought to explain its relevant properties and create ways of harnessing it to the benefit of new and interesting devices and applications. Particularly valuable in nanoscale magnetic materials is the generation of nanoscale multiferroics wherein the ferroic ordering of magnetization is controlled through its coupling with another ferroic ordering, thus making a multi-ferroic. These are of particular import due to the potential for low energy manipulation of magnetic moments at the nanoscale with device implications for computer memory, sensors, and microscopic antenna systems.

The work presented here focuses on superparamagnetic nanoparticle systems. Herein, the process by which nanoparticles are generated is investigated showing methods of improving the synthesis of nanoparticles as well as the generation of novel nanoparticles. Further, the means of characterizing these complicated nanoparticle systems are presented both in measurements of nanoparticle properties as well as specifically the magnetic properties of the superparmagnetic systems through multiple different magnetic material systems. The overarching theme of the work presented herein is to improve our understanding but also our control of the relevant energies of magnetic nanoparticles. The work seeks to show that the messy systems inherent to the art of chemistry can be harnessed in the pursuit of necessarily precise magnetic properties required for a working device. These systems show that we can precisely control the creation of these systems and thus show the possibility of applying these systems to computer memory, magnetic sensors, precise drug delivery, or many other applications that require very precise control of distributions of energy.

Chapter one is an expansion on methods for the fabrication of nanoparticle based multiferroic systems. A method for developing chemically bonded partial monolayers of nanocrystals on surfaces in air free conditions is presented. The method is shown to be able to preserve the magnetic properties of oxygen sensitive nanocrystals while still creating covalent bonds between the nanocrystal surface and the substrate. The adhered nanoparticles are shown and the magnetic properties are shown before and after adhesion. It is shown that while the method does alter the magnetic properties of the crystals it is done in a way that preserves the general magnetic behavior and can be used as the basis for creating interesting magnetic structures of interacting magnetic grains of nanocrystals.

Chapters two and three are concerned at the chemical synthetic level of nanoparticles. Chapter two shows a novel lower temperature method for generating a well-known nanoparticle material, cobalt ferrite. The particles are synthesized through first generating an oxo-metallic cluster

of cobalt and iron decorated with ligands. The ligands are then reacted through a simple esterification process. The method is shown to produce a higher quality of nanocrystal at smaller sizes than other methods while giving easy access to a large range of sizes as well as stoichiometries of the material. The mechanism of formation for the nanoparticles is probed to show that it differs fundamentally from the classical LaMer type mechanism by which most nanoparticle synthesis is understood. Further, the new mechanism is used to explain why the nanoparticle size dispersions are improved and explains the result of multiple different temperature syntheses. Growth and nucleation processes in the synthesis are probed and presented. The magnetic properties of the particles are also probed to show the variable qualities accessible through this synthesis as well as the general higher quality of the nanoparticles produced through this method as opposed to earlier systems.

Chapter three reports the first chemical synthesis of an iron gallium, or "galfenol" material in nanoparticle form that is processable in solution for multiferroics. The nanoparticle is made through the rapid reduction of iron and gallium precursors made possible through the removal and exclusion of oxygen source ligands. The nanoparticles produced are superparamagnetic at room temperature and extremely susceptible to oxygen. Due to the ease of the material to oxidize, it was necessary to work entirely within an oxygen and water free glove box and utilize dry and degassed solvents. Finally using the methods described abstractly in Chapter one, the potential to adhere the nanoparticles to substrates for their use in multiferroic devices was shown. The magnetic properties of the adhered nanoparticles are presented to show the change in the magnetism inherent to the adhesion process for the iron gallium nanoparticles.

Chapter four shows an interesting manner of investigation on the structure of an iron platinum nanoparticle. It is presented with an alteration of the synthetic method driven by this investigation that leads to an improvement in the desired aspects of that particle Iron platinum is a

well-studied material in nanoparticles due to its absurdly high magnetocrystaline anisotropy as well as its uniaxial easy axis magnetization. These properties make it a highly desirable computer memory material; however, these properties only exist in a specific intermetallic phase, $L1_o$ FePt. Generation of this phase is done through a high temperature annealing of the nanoparticles, which is generally done at too high a temperature to use the particles in computer memory applications. This chapter shows that by through a specific investigation of a nanoparticle's stoichiometric distribution, one of the root causes of this high annealing temperature requirement can be discovered. An unintended partial core-shell structure likely common in iron platinum nanoparticles turns to be the likely cause of the high annealing temperature. Further, this can be improved by ensuring simultaneous reaction of iron and platinum precursors.

Chapter five is concerned with a novel mathematical expression for the fitting of nanoparticle magnetic anisotropy distribution curves. The distribution of anisotropies for a set of nanoparticles is generated by finding the derivative of the difference in zero field cooled and field cooled curves for the nanoparticles. The $-d(\text{FC-ZFC})/dT$ curves are calculated for high magnetocrystaline anisotropy (MCA) cobalt ferrite nanoparticles and low MCA nickel nanoparticles. It is shown that the anisotropy distribution for the cobalt ferrite is primarily driven by volumetric crystalline anisotropy whereas the nickel nanoparticles require an understanding of surface and shape anisotropy as well to fully understand the distribution shape. Valuable magnetic data can be gathered through the fitting of the curves, from which we are able to gather important chemical information about the nanoparticles that otherwise would be easy to overlook. This analysis is shown to be valuable in determining problems within nanoparticle synthetic methodology that prevents the use of the particles in multiferroic devices.

CHAPTER 1: AIR-FREE ADHESION OF OXYGEN SENSITIVE NANOPARTICLES FOR INCOROPRATION INTO MULTIFERROIC STRUCTURES

1.1 INTRODUCTION

Nanoparticle research is a vast field that expands yearly. A wide range of 0 dimensional materials have found specialized utilization in many fields.[1,2] Nanoparticles have exciting developments in drug delivery systems as well as magnetic sensors and magnetic memory.[3–7] The key to the sudden generation of novel devices via nanoparticles is accessing the novel physics emergent from quantum confinement effects in nanoscale materials.[8,9] These effects are particularly exploitable in magnetic materials where nano size leads to the creation of the phenomenon of superparamagnetism (SPM).[8] A superparamagnetic material is a material that is so small the ferromagnetic moment is no longer stable to thermal fluctuation, and thus, despite having an aligned magnetic domain, the magnetization averages to zero over any relevant time measurement. These physics give access to the exciting devices mentioned above. As such, magnetic nanoparticles have already seen utilization in many systems. However, efforts to create viable devices from solutions of nanoparticles have been stymied by the lack of processing methods for interfacing nanoparticles with other relevant materials.[10,11]

The problem of integrating nanocrystals into devices is made even more acute by the general sensitivity of nanocrystals to ambient contamination, which can ruin the magnetic properties of the particles. [12–14] Interfacing thin film growth systems typically struggle with nanoparticle methods due to high energy or highly reactive precursors which may oxidize nanocrystals or fail to penetrate surface capping ligands. [15–17] Furthermore, direct physical methods of attaching nanocrystals to preformed substrates through high temperature annealing tends to sinter nanocrystals into larger structures unless the surfaces are coated through additional reactive steps. [18–20] As such, the exclusion

of oxygen from nanocrystal adhesion methods is an important development toward possible multiferroic devices.[10]

In this work, we show a facile method to the generation of controlled partial monolayers of metallic nickel nanocrystals using only the reactive surface of the nanocrystal to drive the reaction in air-free conditions. Rather than being driven by ambient bonding oxygen to create chemical bonds between the crystals and the substrate the naturally high reactivity of the crystal surface is exploited to make covalent bonds to oxygen rich substrates capable of supporting multiple oxidation states. The adhesion is made possible through the synthesis of a bare nickel surface nanocrystal via an altered synthetic method presented here. The magnetic properties of the crystals are measured through SQUID magnetometry to show the effectiveness of the method in retaining nanocrystal properties. Finally, the retention of a clean magnetic surface is also shown through the magnetic properties of the crystals when coated with various materials. Further this shows the utility of the method in creating potential magnetic devices via capping layers.

1.2 EXPERIMENTAL

1.2.1 Synthesis of nickel nanocrystals: Nickel nanocrystals were synthesized using a modified procedure from Carenco, S. et al.[21] A 50 mL Schlenk flask was charged with 2 mmol nickel acetylacetonate as well as 9.5 mmol oleylamine (3.0 mL, Sigma 70%), 1 mmol oleic acid (0.315 mL, Sigma 90%), and 7.3 mL n-octyl ether (24.3 mmol, Aldrich, 99%). The total solution was dried at 100° C and purged with argon three times. 0.45 mmol trioctylphosphosphine (0.2 mL) was injected into the solution via air free injection. The solution was then refluxed under an inert atmosphere at 220 °C for 45 minutes (ramp rate 3 °C/min) and then rapidly cooled to room temperature. 200 proof ethanol was added to the flask. The nanocrystals were precipitated from solution by use of a neodymium magnet. The nanopowder was resuspended in 4 ml of hexanes. The nanoparticles were washed again with addition of 50 mL of 200 proof ethanol and precipitation via a neodymium

magnet. The resultant nanopowder was then resuspended in hexanes.

1.2.2 Synthesis of bare surface nickel nanocrystals: For bare surface nickel nanocrystals, a similar process as described above in section 2.3 was used with the following modifications. The same precursors and solvents were injected into solution and dried at 100° C. After injection only 0.18 mmol trioctylphosphosphine (0.08 mL, Aldrich 95%) was injected into the solution via air free injection. The solution was then ramped to 190° C at a rate of 1.5 C/min. The reaction temperature was held for 120 minutes and then cooled to RT. Purification of the nanopowder was done as described above. The flask was transferred to an air free glove box. 50 mL of 1:9 dry isopropynol:dry methanol (Fisher, 99.7%:Fisher, 99.8%) solution was added to the flask and particles were precipitated with a neodymium magnet. The solution was decanted and 4 mL dry hexanes were added to solution. The nanoparticles were washed again with addition of 50 mL of 1:9 dry isopropynol:dry methanol and precipitation via a neodymium magnet. The nanopowder was then resuspended in dry hexanes.

1.2.3 Preparation of magnetometry samples: Magnetometry samples of nanocrystals were prepared through the suspension of nanocrystals into paraffin wax (Fisher). The wax was melted and a solution of nanocrystals in hexanes were added to the melted wax. The hexanes were driven off at elevated temperature for 10 minutes. The wax was then allowed to cool freezing the dispersed nanoparticles far apart. A fraction of the total wax was injected into a pill capsule, where it solidified. The pill capsules were then fitted in straws for measurement in the SQUID magnetometer. For air sensitive nickel nanoparticles, the same process was followed except inside an oxygen excluding glovebox with an argon atmosphere. To ensure a complete lack of oxidation of the nanocrystals, SQUID magnetometer samples were also prepared in an argon atmosphere box. The pill capsules set in straws were fit into centrifuge tubes within the box, and brought to the SQUID magnetometer

under argon atmosphere. The wax was briefly exposed to oxygen only during transfer from the centrifuge tube to the SQUID magnetometer. The magnetometer was then purged for analysis removing all oxygen.

1.2.4 Substrate preparation: Substrates of titanium dioxide active surface were produced through electron beam evaporator deposition of titanium (25 nm) on as-purchased silicon wafers. The surfaces were then allowed to ambiently oxidize over a 6-month period. After this period the titanium surface was assumed to be completely oxidized.

1.2.5 Preparation of adhered nanocrystal samples: Freshly purified solutions of fully suspended nanocrystals were used exclusively in order to ensure reactive surface. For air free adhesion, A silicon wafer with a titania surface layer was brought into the inert atmosphere box and introduced into the purified nanocrystal solution in hexanes. The sample was left to soak for one to three days. A slight change in color of the substrate surface was noted due to the presence of nanocrystals physiosorbed onto the substrate. SEM imaging was used to confirm the existence of a sub monolayer of nanocrystals. There was no clear difference between this range of soak times. After the monolayers were developed, the substrate was removed from the solution of nanocrystals and then repeatedly rinsed. This washing was performed multiple times with fresh hexanes until clean.

1.2.6 Preparation of surface capped samples: Samples were placed in a small dram vial cap and coated in dry hexanes within an air-free glove box. The dram vial cap and sample were then placed inside the lid of a scintillation vial. The vial was sealed and closed before removing from air-free conditions. The samples were then quickly moved from the scintillation vials into a sputterer without removing the dry hexane blanketing layer. The atmosphere of the sputterer was reduced to vacuum levels evaporating the hexane without exposing the nanoparticles to ambient conditions. A capping layer of gold was then sputtered onto the nanoparticles. For wax coated samples melted wax

was poured around the adhered nanoparticle sample and allowed to solidify around the sample at ambient conditions.

1.2.7 Instrumentation: Magnetic measurements were conducted using a superconducting quantum interference device (SQUID) magnetometer (Quantum Design, MPMS XL-5). Electron Dispersion Spectroscopy (EDS) data was taken via JEOL JSM-6700F FE-SEM. Transmission Electron Microscopy (TEM) images were collected using an FEI Tecnai T12 quick room temperature microscope. X-ray diffraction (XRD) made use of a Panalytical X'Pert Pro X-ray Powder Diffractometer operating with a Cu source.

1.3. Results and Discussion: Prior to development of an oxygen free adhesion method, it was necessary to ensure the nickel nanocrystals had a completely bare and highly reactive surface. Thus, it was necessary to ensure the crystals have no capping phosphorus layer—commonly seen via EDS on nanocrystals synthesized at high temperature with surface capping trioctylphosphine ligands.[12,14,22] In earlier methods, nanocrystals synthesized at 220° C with high levels of trioctylphosphide showed limited reactivity in air free conditions with titania substrates. Rather, to form covalentaly bound crystals in reasonably dense monolayers, exposure to ambient oxygen over long periods was required.[10]

As such, the method developed by Carenco et al. used prior was modified primarily by dropping the reaction temperature to 190° C and reducing the amount of trioctylphosphine. It was found to be impossible to completely remove trioctylphosphine as the nanoparticles would undergo uncontrollable growth leading to large size dispersions without the surface capping ligand. EDS measurements confirm a far lower amount of phosphorous in the subsequent nanoparticle samples below the detection limit. The method produced a large number of Ni nanocrystals and at a larger size for the given conditions as would be expected by the lower number amount of capping ligand.

A TEM image of the produced nanoparticles appears as figure 1.1 along with an XRD of the crystals. All nanocrystals are superparamagnetic as evidenced by a

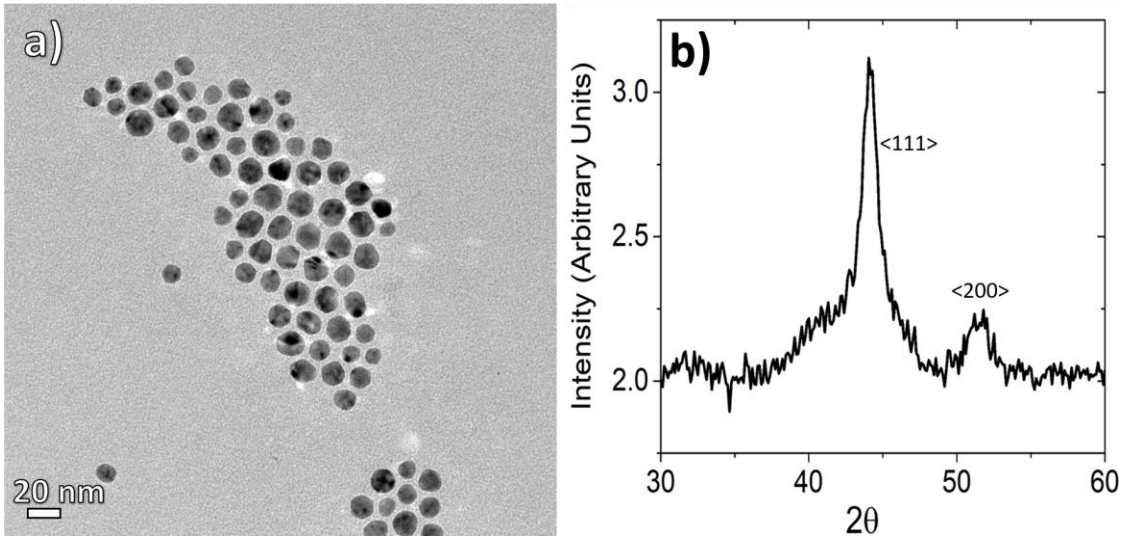

Figure 1.1 a) TEM images of Ni nanocrystals produced at 190° C with low trioctylphosphine. Crystals are 15 nm in average diameter. b) XRD pattern for nanocrystals after air exposure. 111 and 200 peaks can clearly be seen.

lack of coercivity when measuring magnetization at varying fields.

With sufficiently bare surface nanocrystals it became possible to generate monolayers of adhered crystals in air free conditions on reactive titania surfaces. The adhesion process is described above in section 1.2.5. Images of the partial monolayer formed during the adhesion process appear in figure 1.2. The nanocrystals are chemically attached to the substrate and impossible to remove via washing even when submerged in solvent with sonication. Furthermore, there is a clear magnetic difference between the nanoparticles before and after adhesion.

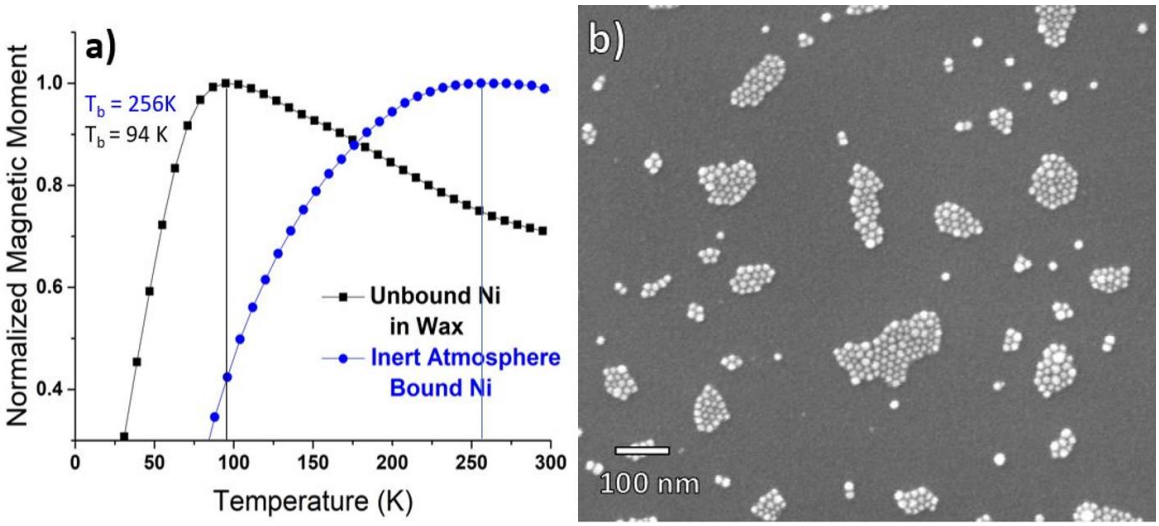

Figure 1.2 a) ZFC measurements of air excluded nanocrystals prior to adhesion and adhered nanocrystals measured in-plane. Blocking temperature increases from 94K to 256K due to increased sources of anisotropy. b) SEM images of nanocrystals after adhesion process. Nanocrystal size is not substantially altered. Monolayer coverage can be increased with longer soak times.

Because all nanoparticles are ubiquitously superparamagnetic, the blocking temperature of the nanocrystals was measured using zero field cooled measurements. An ensemble of nanocrystals is cooled to cryo temperatures in the absence of a magnetic field freezing the superparamagnetic moments into ferromagnetic directions. A small magnetic field is applied and the temperature is raised. As nanoparticles transition back to superparamagnetic, they align with the applied field increasing measured magnetization. The peak of the curve is the blocking temperature for the sample and is indicative of the anisotropic energy of the nanocrystals. The nanocrystals show a very large increase in blocking temperatures a result from adhesion, larger than has been observed in the case of oxygen rich adhesion processes.[10] The large increase of blocking temperature in the sample is indicative of a large increase in the anisotropy energy of the crystals. In the case of adhesion, this is likely due to strain applied to the nanocrystals by the adhesion process. The otherwise spherical crystals likely deform to create a larger interaction surface with the oxygen rich titania surface creating an oblong gumdrop shape.

The utility of the air-free method is obvious when exploring the potential to cap the nanocrystals to avoid oxidation of the nanocrystals. Figure 1.3 shows the results of the adhered nanocrystals with different capping layers as well as compared to a control of air exposed

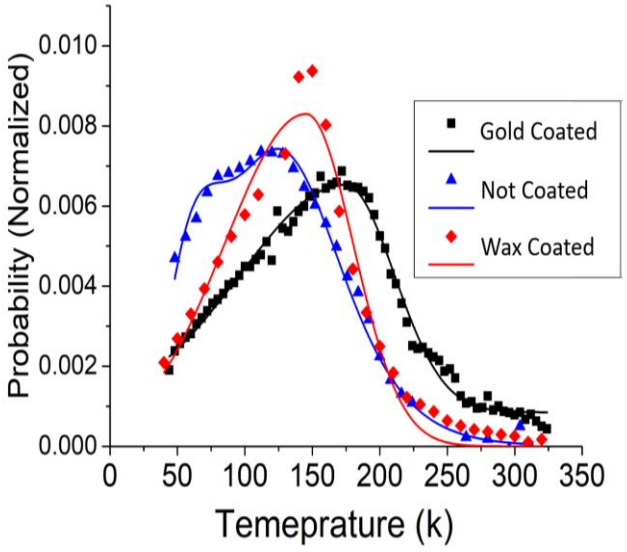

Figure 1.3 a) ZFC measurements of air excluded nanocrystals adhered nanocrystals measured in-plane. Nanocrystals were coated in sputtered gold (black), as well as in wax (red). Measurement was also done on adhered nanoparticles after exposure to air (blue). The blocking temperature of the crystals is lowered by air exposure due to conversion of metallic nickel to nickel oxide. Gold coated nanocrystals are highest due to exchange coupling.

nanocrystals. Exposure to oxygen generates a native oxide layer on the nanocrystals turning a portion of the crystals to NiO thus lowering the total volume of nickel for the crystals. The loss of nickel volume for the nanocrystals results in a greatly reduced blocking temperature of the crystals due to a lowering of the magnetocrystaline anisotropy from a smaller volume of nickel. Compared to the air-free wax coated nanocrystals, the oxygen exposed nanocrystals have a lower average blocking temperature due to the oxidation of the nanoparticles. However, the gold coated nanocrystals have an increased blocking temperature as compared to even the air free wax coated nanocrystals. The increased blocking temperature is due to a larger amount of exchange coupling anisotropy between

the nanocrystals as a result of the gold interstitial filling. Gold, as a highly conductive medium, allows for a high degree of electron hopping between the nanocrystals meaning an increased degree of exchange coupling and therefore higher blocking temperature. [23,24] From this figure it is shown that different distributions of anisotropies can be generated simply through control of the environment made possible by air free adhesion of nanocrystals.

1.4 CONCLUSIONS

Thus, we have demonstrated an improved self-assembly method to adhere magnetic nanoparticles to substrates in an air-free process that is able to retain high quality of nanocrystal despite oxygen sensitivity of the crystal. The adhesion process takes advantage of the reactive nanoparticle surface of bare nickel nanoparticles. Adhered nanoparticles show increased blocking temperature due to strain applied to the crystal from the adhesion process. Further it can be shown that the air-free quality of the crystals can be retained through processing and can even be exploited by choice of capping medium. This shows a great deal of potential in creating multiferroic structures.

CHAPTER 2: LOW POLYDISPERCITY, SCALABLE SYNTHESIS OF VARIED STOICHIOMETRY COBALT FERRITE NANOPARTICLES VIA CONTINUOUS SOLVOTHERMAL GROWTH

2.1. INTRODUCTION: Magnetic nanoparticles are a widely researched development. Medicinally, they have been used for direct drug delivery devices[25–29] as well as hyperthermia treatment by generating heat through AC magnetic fields applied to high coercivity materials.[25,26,30–32] Beyond biology, nanoparticles offer an efficient path to constructing high bit density computer memory with extremely low write energies.[33–35] Magnetostriction, the change in a particles shape via applied magnetic field, offers even more possibilities for applications.[36–38] These particles are capable of minute energy harvesting and translation of electromagnetic waves through the coupling of magnetics and physical structure. [36–38]

Many of these new applications stem from the emergent behavior of nanoscale magnets of superparamagnetism. In a sufficiently small magnetic crystal, high energy domain walls are excluded leaving the material with only one magnetic domain.[25] Because the alignment energy of a ferromagnet is proportional to the volume of the material, at even smaller sizes, the energy barrier between the alignment directions of this domain becomes smaller than thermal energy. Thus, the magnetization direction fluctuates at random creating a superparmagnetic (SPM) material. [25] The result is a ferromagnetic material with a time averaged net magnetization of zero. Additionally, because the magnetization is net zero, the magnetic attractive forces between the particles dissipate. Therefore, the particles are able to remain suspended in solution. The fluctuating ferromagnetic moment will still align with any applied field like a paramagnetic material but with high saturation characteristic of ferromagnets. [25] This generates rapid heating under small AC fields in hyperthermia[32,39,40], negligible write energy for non-volatile computer memory,[31] and low field size changes in magnetostrictives. [36–38] However, superparamagnetism only exists at negligible anisotropy

energy. The anisotropy energy barrier between alignment directions is the sum of many energies, including shape, surface, and particle-particle interaction. A small increase in nanocrystal average volume or agglomeration of nanocrystals can induce an increased anisotropy energy transitioning the superparamagnetism back to ferromagnetism at ambient temperature removing the utility of the material. Therefore, precise control of the shape and size distribution of generated nanoparticles is absolutely necessary.

Magnetic nanoparticles are made myriad ways. Synthetic approaches can be classified as top down, where the desired materials compositions are achieved and then reduced to nanoscale sizes,[41–43] and bottom up where elemental precursors are coprecipitated into nanomaterials.[25,44–47] While top down approaches such as ball milling excel at maintaining stoichiometric control for specific phases, they tend towards poor size and shape dispersion and long synthesis times.[42,48–50] Bottom up approaches generally rely on creating unstable precursors and causing sudden precipitation of these precursors into particles.[47,51–53] This can take the form of rapid reduction of metals to form zero-valent metal nanoparticles or rapid decomposition to form an oxide. All methods employ various extra efforts to try to maintain low size dispersion of particles. Typically, this means use of surface capping ligands or micelle isolated growth. However, low size dispersion remains a constant goal.[53–55]

Cobalt ferrite (CFO) offers specific promise as a nanoscale magnetic material. As with any oxidized ferrite, CFO even remains remarkably air and water stable in the nanoscale. The stability allows for compatibility with capping layers such as silica leading to a reliably biocompatible magnetic nanoparticle.[28,33] Additionally, CFO tends to good ionic ordering where cobalt occupies the 2+ charge state of the spinel structure of the ferrite with very little cation mixing due to cobalt's instability as a 3+ cation.[33,56] Finally, the structure has a high inherent crystalline anisotropy, up to an order of magnitude higher than ferrite, and substantial magnetostrictive behavior creating opportunities for multiferroic coupling.[36–38] The high anisotropy can be further enhanced by altering

the stoichiometric ratios of iron to cobalt.[55,56] A peak in anisotropy occurs around $Co_{0.6}Fe_{2.4}O_4$ for a material which has a crystal anisotropy rivaling rare earth magnets.[56]

Due to this value as a research material, many bottom-up methods have been used to synthesize nanoscale cobalt ferrite nanoscale cobalt ferrite (CFO),[54,57–63] Surfactant based synthetic methods have been developed using a constant concentration of micelle forming surfactants to limit growth of particles and produce nanoparticles of sizes 2-15 nm. The particle size is limited by growth occurring only within the confines of the micelles.[54,55] Other methods have used high temperature decomposition of organic metal complexes through calcination or combustion to achieve average sizes from 12 nm to as large as 90 nm with high saturation magnetizations and coercivities.[55,58,59] Wet chemical methods using hydrothermal autoclaves have shown morphological control at size ranges of average 16 nm to up to 200 nm.[60,61] Finally, a large number of methods have used straightforward "heating up" processes where organic metal precursors are reacted in a high boiling point solvent and precipitated particles are capped with surface ligands to hinder growth.[57,62,63]

Generally, the specific chemical process to form nanoparticles is described as being a LaMer mechanism of burst nucleation and growth.[64,65] Decomposition of precursor creates a dissolved "monomer" base unit of a nanoparticle. Concentration of monomer increases during heating until it reaches supersaturation. At that point, nucleation becomes energetically favorable, and small clusters called nuclei form rapidly dropping monomer concentration. Because concentration returns to below the supersaturation point, nucleation is again energetically unfavorable and ceases. All remaining monomer can only react through growth of the already existing particles. The sudden onset and quick end of the nucleation conditions is what creates a finite size distribution of particles. Because no new particles form, the earlier ones grow at similar rates resulting in a clustering of final sizes rather than a continuous size distribution from zero. This mechanism was originally proposed

as a justification for the formation of monodisperse sulfur hydrosols and not as a generalized nanostructure formation mechanism.[65,66]

For the past 50 years, LaMer-based mechanisms have typically been used as the foundation to explain nanocrystals synthetic procedures.[44,56,67–72] Generally the mechanism is only stated with minute details as a means of justification for an observed finite size distribution.[44,73] The mechanism has been theoretically defined and proven effective in Monte Carlo simulations and defined with numeric expressions in certain systems.[74,75] Expansion of the fundamental concept of the mechanism has led to some creative forms of size control as well.[69–71] Average nanoparticle size was increased in metal oxides nanoparticles through controlled addition of precursor only during the growth stage of the mechanism.[69,70,76] Additionally, the mechanism has been used as the basis for nanoparticle mechanisms leading to shape control. Surface capping ligands can modulate the rate of growth at different crystal facets leading to controlled shapes. [71,72]

However, while the original LaMer mechanism is extremely specific, most wet chemical nanoparticle syntheses are profoundly messy and likely occur through a number of simultaneous pathways.[65,66] Where LaMer presents mathematical justification for the separation of nucleation and growth, in most syntheses the processes are far from mutually exclusive. [76–80] For example, LaMer *et al.* clearly identify sulfur monomers in the formation of colloidal sulfur, the exact identity of a LaMer mechanism monomer is often glazed over in nanoparticle synthesis; this is especially true when creating an oxidized nanocrystals where the source of oxygen is neglected.[39-41] Often, substantial modifications to the mechanism are required to bridge the gap from understanding of decomposition to a full kinetic picture. [62,65,66,56,69 76–80] As such, more recent studies have started to evaluate the assumptions behind the LaMer mechanism and further have proposed using more designed mechanistic nanoparticle synthetic regimes to ensure low size dispersion, and higher quality crystals.[65,66,70]

To circumvent the problems of LaMer assumptions, recent work by Chang *et al.* has used a designed non-LaMer chemical mechanism to create a continuous growth process can be used to form ferrite nanoparticles. [65,66,81,82] This process removes a discrete nucleation event by growing crystals from a tri-metal-oxo carboxylate cluster. Metal precursors are condensed into three metal atomic clusters. The clusters are decorated with terminal long chain carboxylic acid ligands. A primary ethanol is added, which reacts with the carboxylic acid ligands via an esterification reaction. After the reaction, the ligand is removed, and the cluster is left with a reactive radical end leading to continuous growth of the clusters into nanoparticles.[81] The formation of the initial cluster is energetically favorable due to the strong binding energy of the carboxylic ligands but slows as precursor cluster population drops compared to nanoparticle population, creating good size control.[81] Esterification has also been shown to produce manganese oxide nanoparticles of varying phase depending on varying amount of alcohol.[82]

In this work, we utilize the continuous growth method developed by Chang et al., to show the broad scope of this mechanism by synthesis of a well-studied material, cobalt ferrite (CFO) from a heteroatomic metal-oxo cluster previously synthesized.[81,83] We utilized the clusters to synthesize cobalt ferrite nanoparticles at varied stoichiometries using this novel methodology. It is shown that stoichiometrically precise CFO can also be synthesized via the same method. The synthetic method uses low cost acetylacetonate precursors and oleic acid ligands. It is straightforward in performance, scalable in synthetic size, and capable of precise size control. It is shown that the new method is superior in shape control and size dispersion than previous methods. We investigate some of the growth and nucleation mechanisms that simultaneously exists in this method. Finally, we show that the anisotropy constant of the as synthesized particles is higher than particles synthesized in a more conventional burst methodology. The anisotropy of the cobalt deficient nanoparticles is remarkably

high. Ultimately this all leads to a distribution with more uniform magnetic characteristics improving utility for magnetic applications.

2.2 EXPERIMENTAL:

2.2.1 Preparation of esterification active precursor: Esterification active precursor was formed through the reaction of metal acetylacetonate salts with oleic acid under vacuum. In a 50 mL standard Schlenk flask, 0.194 mmol cobalt (II) acetylacetonate (Aldrich, 97%) and 0.399 mmol Iron (III) acetylacetonate (Aldrich, 99.9%) were mixed with a stir bar in a solution containing 5 mL oleic acid (15.75 mmol, Panreac, purified by distillation) and 6 mL n-octyl ether (19.95 mmol, Aldrich, 99%). The solution was degassed at room temperature (RT) for ten minutes. Following a 15-minute ramp up from RT, the solution was further dried under vacuum at 100 ºC for 30 minutes.

2.2.2 Esterification Based Synthesis of CFO nanocrystals: Under argon, 4 mL 1-decanol (20.95 mmol, 'Baker', 99%) was added to a solution of esterification active precursor synthesis described above. The mixture was heated to reaction temperature (180 ºC or 200 ºC) with a 15-minute ramp period and held for a reaction time (30 - 600 minutes). The resulting nanoparticles were cooled to RT. To the solution, ethanol was added and the particles were centrifuged and the solution was decanted. The product was then re-dispersed in hexanes and washed with ethanol twice before being dispersed in hexanes.

2.2.3 Literature Conventional Synthesis of CFO nanocrystals: All nanoparticles prepared by the classical solvothermal method were synthesized following an oxygen-free procedure adapted from Lu et al.[38] In a 50 mL standard Schlenk flask, 63.0 mg cobalt (II) acetylacetonate (0.245 mmol, Aldrich, 97%), 125 mg Iron (III) acetylacetonate (0.354 mmol, Aldrich, 99.9%), and 155 mg 1,2-hexadecandiol (0.600 mmol, Aldrich, 90%) were dissolved with a magnetic stir bar in a mixture of 6 mL oleylamine (18.24 mmol, Panreac, purified by distillation), 2 mL oleic acid (6.3 mmol, Panreac, purified by distillation), and 4 mL n-octyl ether (13.30 mmol, Aldrich, 99%). The solution was degassed at room

temperature (RT) for ten minutes. Following a 15-minute ramp up from RT, the solution was further dried under vacuum at 100º C for 30 minutes. Under argon, the mixture was heated to 250 ºC with a 15-minute ramp period and held for 30 minutes. The resulting nanoparticles were cooled to RT, centrifuged, decanted, and dispersed in hexanes. The product was then washed with ethanol twice before being re-dispersed in hexanes.

2.2.4 Preparation of Magnetometry samples: Magnetometry samples were prepared through the suspension of nanocrystals into paraffin wax to reduce interaction between the crystals. Paraffin wax was melted in a scintillation vial. A concentrated solution of washed nanoparticles suspended in hexanes was then injected into the paraffin wax. the hexanes were evaporated from the mixture by sustained heat over ten minutes. A fraction of the total wax was injected into a pill capsule, which was then fitted for measurement in the SQUID magnetometer. The wax was resolidified at ambient temperature before use.

2.2.6 Instrumentation: Magnetic measurements were conducted using a superconducting quantum interference device (SQUID) magnetometer (Quantum Design, MPMS XL-5). Oxidation potential of surfaces and samples carried out using X-ray Photoelectron Spectroscopy (XPS) from a Kratos Axis Ultra DLD spectrometer with a monochromatic Al (Kα) radiation source. Scanning electron microscope (SEM) images taken via JEOL JSM-6700F FE-SEM. TEM (cnsi tencai T12)

2.3 RESULTS AND DISCUSSION: The crux of esterification nanoparticle synthesis is the esterification of a carboxylate-ligand heteroatomic tri-metal-oxo precursor.[81–83] To create an esterification active precursor, acetylacetonate-ligand metal precursors were mixed with oleic acid under vacuum at high temperatures. The acidic proton of the oleic acid protonates acetylacetonate ligands, removing them, and generating an oleate ligand for the metal. Protonation and replacement

of acetylacetonate ligands then, is driven by evaporation of acetylacetone from the system via vacuum.

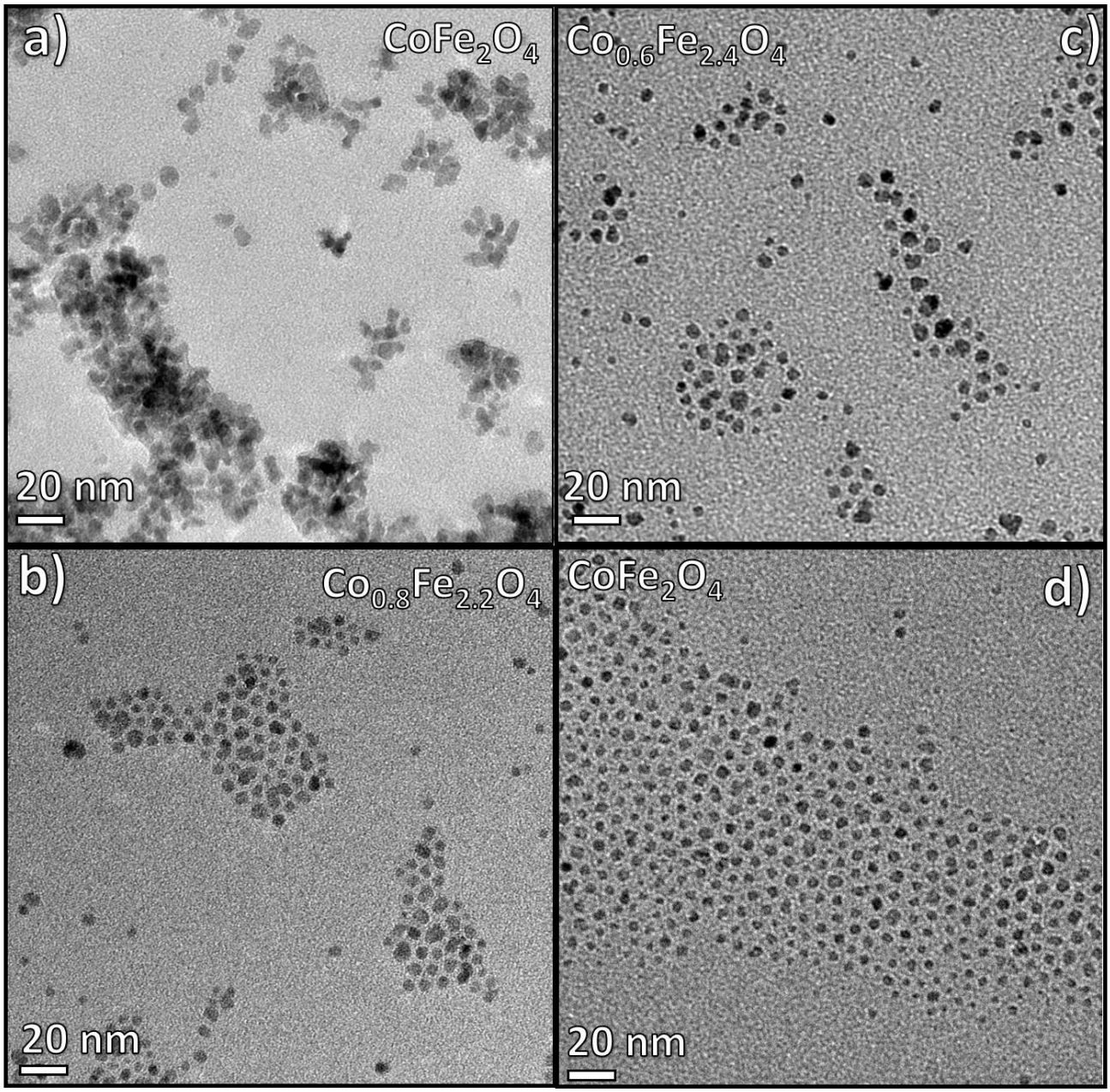

Figure 2.1. a) TEM of CFO nanoparticles produced through conventional nucleation and growth method showing high agglomeration and high variation in size and shape. b) TEM of CFO nanoparticles produced through esterification at 200° C synthesis showing low agglomeration and size dispersion c) TEM of CFO nanoparticles produced through esterification at 180° C synthesis showing low agglomeration and small dispersion. d) esterification synthesis method nanoparticles with excess cobalt leading to stoichiometrically precise $CoFe_2O_4$ Cobalt Ferrite.

The esterification of carboxylate acid ligands on the metal-oxo cluster leads to growth of the precursor clusters into nanoparticles as described by Chang et al.[81] TEM images of particles

synthesized via an esterification process appear in Figure 2.1. These particles were compared to particles synthesized from a conventional method from Lu et al. using reducing agents at high temperatures representative of heat-up methods in literature.[63] The specific synthetic method for the conventional nanoparticles is listed in Section 2.2.3. Figure 2.1 features TEM images of these differently sourced nanoparticle samples. Visual inspection thereof shows stark contrast between the esterification nanoparticles and those of the conventional method. Regardless of stoichiometry, esterification nanoparticles are uniform and well dispersed. Likely, the relatively slow growth kinetics of esterification leads to a more facet averaged particle with a more spherical shape. However, for conventional synthesis, growth occurs rapidly leading to in a larger kinetic distribution of shape. Thus, synthesis results in more oblong and lumpy particles. Further, there is an apparent increase in agglomeration of the nanoparticles from the conventional synthesis. Particles in figure 2.1b are synthesized at 200° via esterification whereas those in figure 2.1c are at 180° to show that low temperatures successfully create visually indistinguishable particles. Particles of CFO precise stoichiometry via esterification appear in figure 2.1d showing the method is viable to multiple stoichiometries. The specific stoichiometries of the particles is controllable through a combination of synthesis temperature, and precursor ratio.

The nanoparticle sizes are quantified in figure 2.2, wherein histograms of the size distribution of the nanoparticles are presented. The conventional method produces a much broader distribution of sizes than any of the variations on esterification method. Conventionally derived nanoparticles have an average diameter of 7.6 nm with a standard deviation of 3.0 nm whereas as an example, the 180 °C 3-hour esterification particles averaged 6.7 nm in diameter with a standard deviation of only 1.3 nm. The esterification method shows small size distribution at several size regimes through variation of reaction time and temperature.

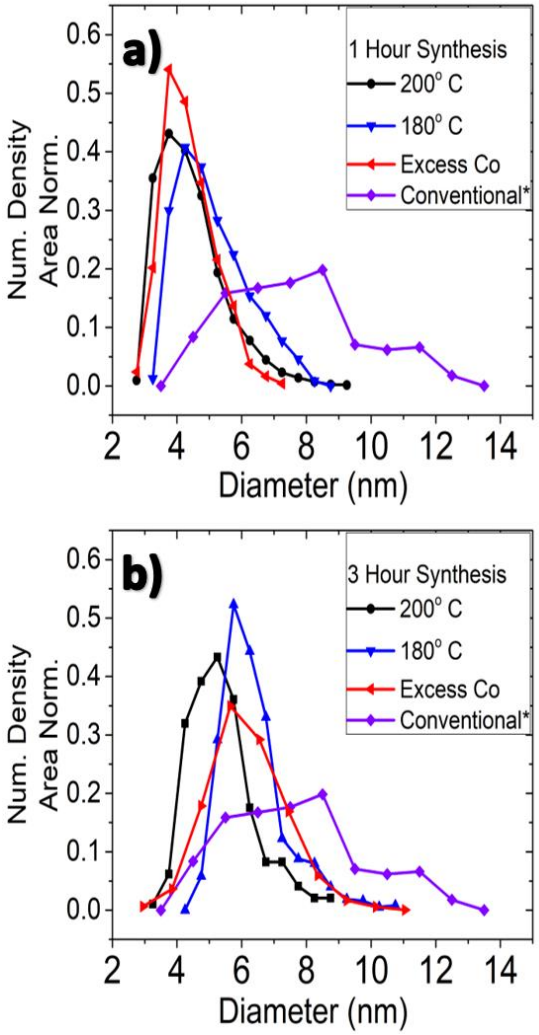

Figure 2.2 Size distributions for nanoparticles of varying design from esterification synthesis compared to conventional particle synthesis. Histograms for 200° C and 180° C synthesis are presented in black and blue respectively as well as stoichiometrically precise CFO in red. Histograms in a) represent an hour of synthesis whereas b) shows three hours of synthesis. Conventional particles presented are the same in each graph.

To demonstrate continuous growth as a means of generating precise size control, a set of syntheses were run with nanoparticles aliquots taken at various time points. Nanoparticles from each aliquot were isolated and size was measured via TEM. For esterification at 180° C or 200° C the average size of the particles shows continuous size growth over a long period of time, which contrasts with conventional methods. Generally, heat up synthesis is understood to follow a burst nucleation event, which quickly reaches a final size dictated by the interplay of surface ligands and exhaustion of precursor. Figure 2.3 shows the result of time point studies. The average size of crystals at the sampled time is reported in figure 2.3. For crystals grown at either 180 °C or 200

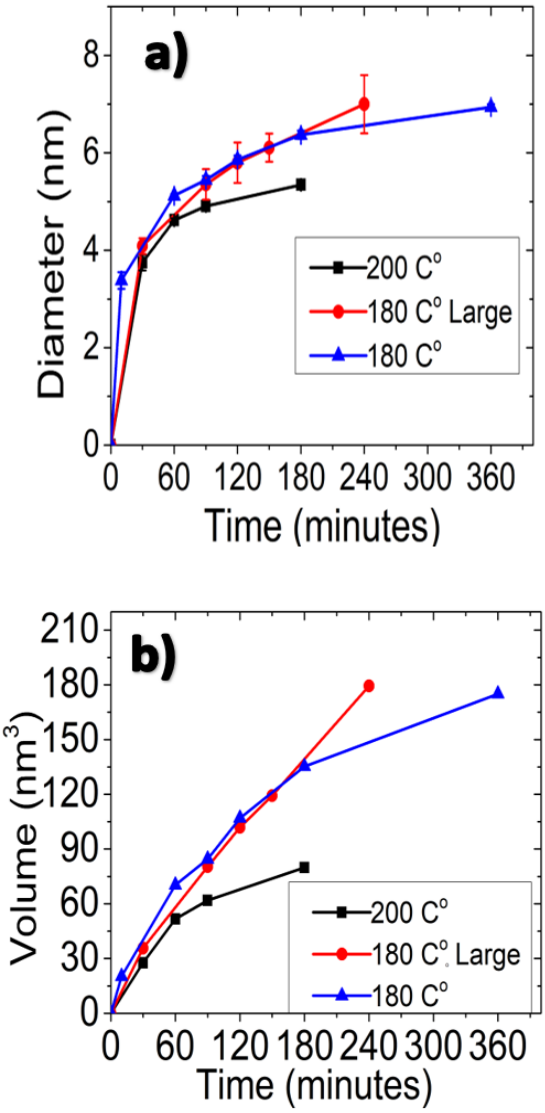

Figure 2.3. a) Average nanoparticle size as a function of time as determined by aliquot removal from an ongoing synthesis. All esterification based synthetic methods show continuous growth of nanoparticles over a long period. Growth is not affected by scale up of method. b) Time dependent volume growth of nanocrystals over time in both 180°C and 200 °C synthetic methods. At 180 °C growth follows a continuous kinetic-limited process within the studied region. For 200°C nanocrystal growth is linear but slows

°C reaction temperature, nanocrystal diameter increases continuously over a long region. Figure 2.3b shows that volumetrically the 180 °C synthesized particles grow linear over the studied period expected of continuous growth. Linear growth is reproduced in a scaled-up synthesis as well (red) with double the volume of that shown in the blue curves. The linear growth implies stable growth kinetics leading to easy size control in both small and large batches important for industrial applications. In addition, figure 2.3 shows that particles grown at 200 °C are noticeably smaller throughout the observed time period. The different growth pathways imply that temperature asymmetrically affects nucleation and growth mechanisms of the particles. At 200° C the precursor is disproportionately susceptible to new nucleation of particles such that more nuclei are formed. With more nucleation the same degree of growth systematically leads to smaller particles during the same time period.

It was suspected that at 200 °C the enhanced nucleation was due to metal-oxo cluster precursor to spontaneously decomposing without primary alcohol esterification leading to a

supersaturated solution of metal atoms, and thus LaMer type synthesis on top of the esterification. If so, the amount of precursor consumed by nucleation would increase, reducing the amount of material available for growth, thereby, decreasing the final size of the nanoparticles as was seen. To investigate the possibility of direct thermal decomposition at 200° C, synthesis was carried out without any alcohol, precluding esterification. The method described in section 2.2 was followed but without decanol addition for a three-hour soak, However, at either 180 °C or 200 °C no particles could be created from this altered method. Therefore, the metal-oxo cluster precursor must be stable at 200° C and does not decompose thermally into nanoparticles without the presence of an alcohol.

Additional nucleation mechanisms were investigated to justify the differences in 180° C and 200° C synthesis. In many nanoparticle systems there is the possibility that previously formed crystals can catalyze decomposition of the precursor, thereby leading either to growth of the crystal or even generation of new nuclei called seed-mediated nucleation.[25,44–46] To investigate the possibility of seed-mediated nucleation of nanocrystals, previously synthesized nanoparticles formed through esterification synthesis were added to a flask of metal precursors. Again, alcohol was excluded from the reaction to prevent esterification from occurring. The solution was heated to 180° C or 200 °C. In either case the exact same distribution of seeds was used. After thirty minutes of soak at high temperature, the nanoparticles were extracted and imaged. A comparison between the yielded new nanoparticle distributions appears in figure 2.4.

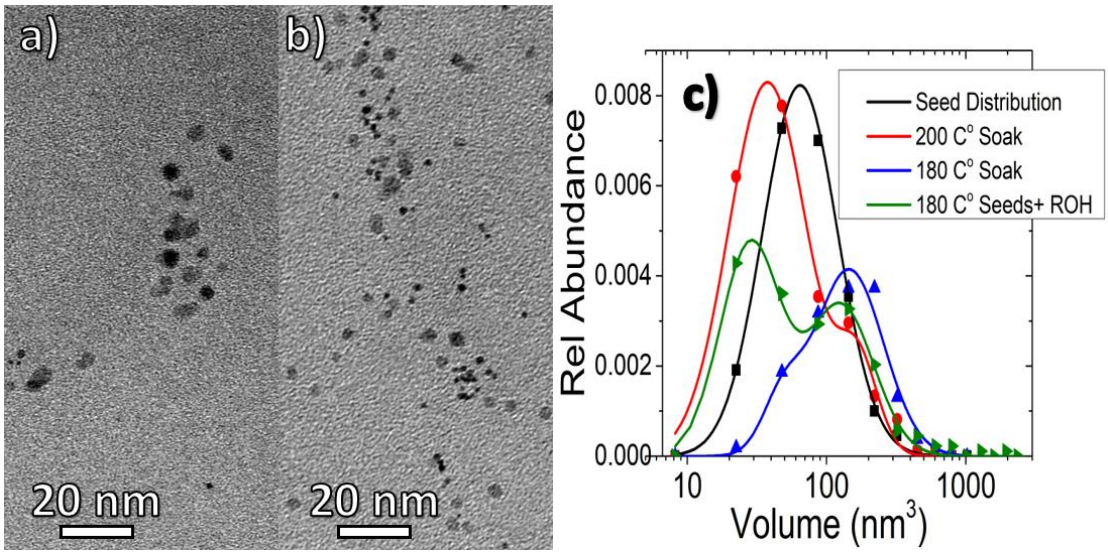

Figure 2.4. a) TEM of CFO nanoparticles after heating seed CFO nanoparticles at 180° C for 30 minutes in a precursor solution with no decanol present. Most visible particles are large with some very small new particles being visible. b) TEM of CFO nanoparticles after heating seed CFO nanoparticles at 200° C for 30 minutes in a precursor solution with no decanol present. Some visible particles are large but the majority are very small new particles. c) Size histograms on a logarithmic scale through imageJ analysis of TEM images of nanoparticles generated through heating of seeds at 180° C or 200° C in oxo-metallic precursor solution as well as size histogram of the initial seed distribution. Distribution shows 200°C heating preference for nucleation and 180° C preference for growth.

From the TEM images new small particles appear after a thirty-minute soak at either 200° C or 180° C; thus, it is apparent that seed-mediated decomposition of metal-oxo precursor occurs in both 200 °C and 180 °C synthesis. At 200 °C, seed-mediated decomposition of precursor generates a large number of new nanocrystals. As can be seen in the TEM images in figure 2.4b, the original nanocrystal seeds appear but there is a large number of new smaller average size nanocrystals. However, for the 180 °C soak synthesis, the majority of observable crystals are simply larger seeds while very few small particles appear.

This dichotomy is better represented by the histogram distributions of the measured particles as seen in figure 2.4c. While the distribution of seeds fits well to one log-normal curve of average diameter of 6.7 nm, the distribution the distributions after a second soak require two log normal curves

to fit, one for new nuclei and one for the slightly larger original seeds. For 200° C synthesis, the average sizes via these two distributions are 5.1 nm and 7.2 nm diameters respectively. For 180 °C growth soak with seeds, the mean sizes are 4.8 nm and 7.7 nm. More importantly than the modest differences in average diameter are the relative sizes of these peaks within the distribution. As a normalized curve, the size of the curves corresponds to the population of particles within that curve. For the 200 °C soak, the smaller distribution has twice the population of the large diameter distribution. However, for 180° C soak the smaller diameter particles only account for roughly a twentieth of the total population. Thus, the additional seed mediated decomposition pathways at 180 °C favor growth whereas at 200° C nucleation is favored leading to smaller final size in 200° C than 180° C.

Finally, to show that esterification is the primary process by which nanoparticle nucleation occurs in 180° C synthesis the seed mediated reaction was run with reintroduction of decanol. The resulting nanoparticle population can be seen in green in figure 2.4c. The distribution closely resembles that of the 200 °C seed-based synthesis. The distribution again requires two lognormal curves to fit due to seeds and new nuclei, with average sizes of 4.3 nm and 7.2 nm diameter. Thus, the decanol is necessary not just for the initiation of the reaction but also helps to lower the energy barrier towards growth of nanocrystals from precursors allowing nucleation to occur at 180 °C.

In addition to evaluating the size distribution of the nanoparticles, testing was done to evaluate the magnetic quality of the esterification generated nanoparticles. A series of magnetic tests was performed using a SQUID magnetometer. Measurement of magnetization with applied field was performed to show the particles were indeed SPM. The magnetization under applied field of the particles passes through the origin as is expected for SPM nanoparticles. All distributions of nanoparticles in this work are superparamagnetic.

Because the randomization of magnetization direction is a thermal effect, there is a transition temperature referred to as the blocking temperature. Below that temperature, the particles return to a normal ferromagnetic state. Blocking temperature of the superparmagnetic particles was probed through zero field-cooled and field-cooled tests. Generally, to acquire a zero-field cooled curve, particles are cooled with randomized magnetization direction and heated with a small applied field. Magnetization increases as the particles near their SPM transition temperature and can align with the applied field. The maximum observed magnetization is listed as the ensemble blocking temperature. An example of this curve appears in figure 2.5a for a representative sample showing a blocking temperature of around 175 K.

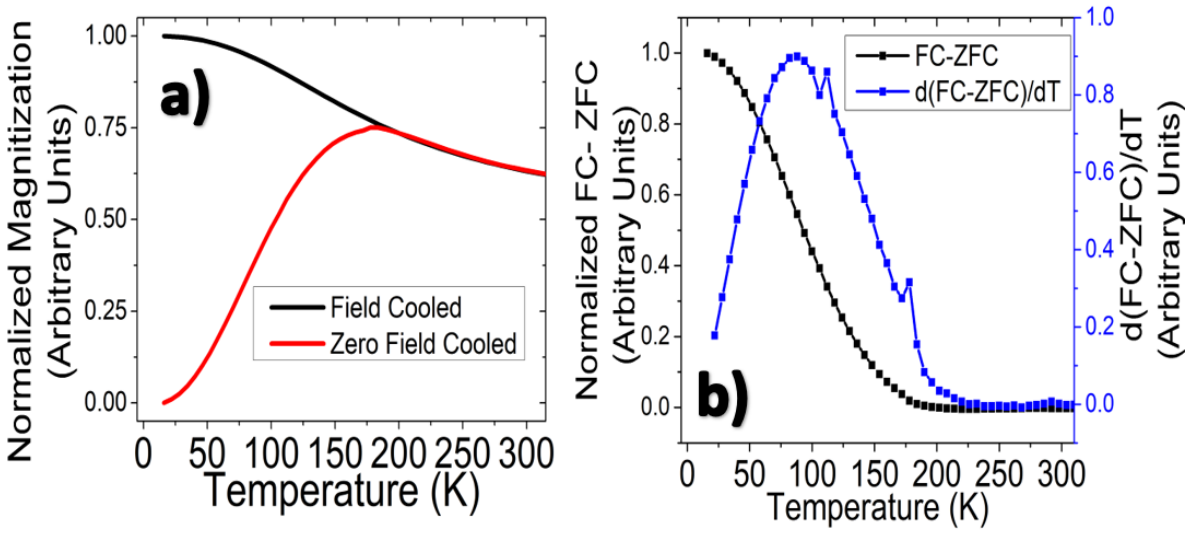

Figure 2.5. a) Example FC and ZFC curves of nanoparticles synthesized through esterification at 180°C b) FC-ZFC curve (black) showing cumulative population distribution of un-blocked nanoparticles. Derivative curve (blue) showing population of blocking temperatures in an example sample.

To visualize the average individual blocking temperatures of the particles, $-d(\text{FC-ZFC})/dT$ curves have been calculated for the different syntheses. As implied by the name, these curves are generated by taking the derivative of the difference between a field cooled (FC) measurement and a zero-field cooled (ZFC) measurement. This derivative corresponds to the population of nanoparticles

that is switching from a blocked ferromagnetic state to a SPM state at the measured temperature differential. The height of the curve generated shows the relative population of nanoparticles with that blocking temperature and as a whole the graph represents a population distribution of number density of particles with the given temperature as a blocking temperature.[22,84,85] An example of these curves is

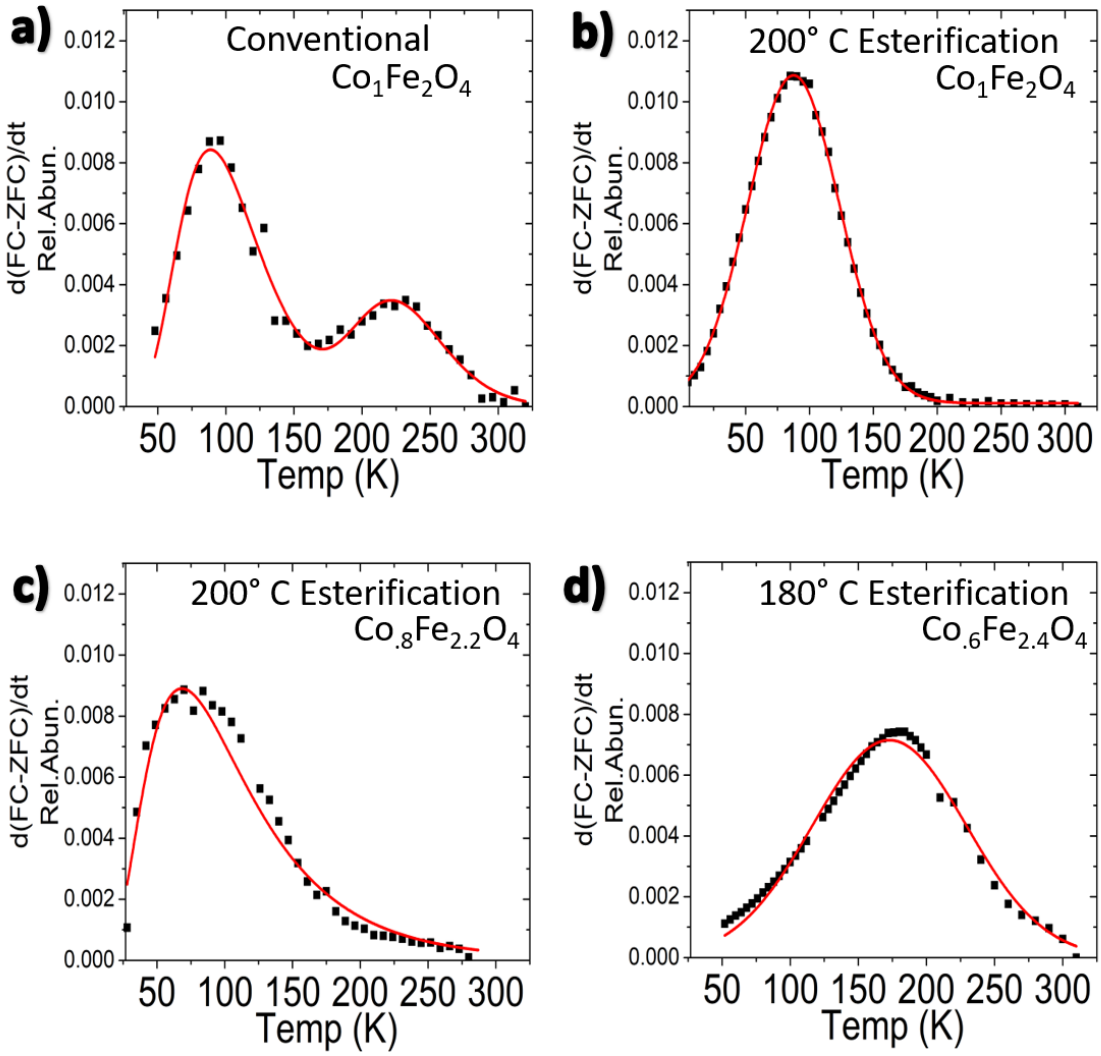

Figure 2.6. *d*(ZFC-FC)/*dT* graphs are shown from SQUID magnetometry of three representative samples of conventional(a) esterification of CFO stoichiometry at 200° C (b) 180°C off stoic esterification (c) and 200°C stoichiometric CFO esterification synthesis(d). Fitting functions have been applied to each of the curves in order to glean the average blocking temperature of the sample. The two peaks in conventional correspond to two peaks in the volumetric distribution and therefore have two average blocking temperatures and two anisotropy constants.

shown in figure 2.5b. The FC and ZFC curves used to generate the figure are the same as appear in figure 2.5a.

The average blocking temperature allows for a calculation of the anisotropy constant for the nanoparticle distributions. The effective anisotropy constant of the crystals serves as a good volume normalized metric by which the quality of the nanoparticles can be compared. An average effective anisotropy constant can be calculated from the average blocking temperature with the average volume as determined by TEM distributions as described in eq 1.[22,86–88]

$$(1)\ \boldsymbol{T_b = \frac{K_{eff}\langle V\rangle}{25k_b}}$$

As such representative d(FC-ZFC)/dT curves with distribution fittings are shown in figure 2.6 for Cobalt Ferrite nanoparticles synthesized via conventional, 180°C esterification, 200°C esterification methods, and stoichiometric CFO via esterification. The average blocking temperature of each is found from fitted curves. For 180° C and 200° C esterification these average blocking temperatures are 188 K and 182 K respectively. The average volume of the particles is found by taking the TEM image derived volumetric histogram for a given synthesis and fitting a lognormal distribution to it.[62] The esterification derived stoichiometric cobalt ferrite samples had an average volume of 105 nm^3 and blocking temperature of 87.6K, thus a K_{eff} of 287. kJ/m.[3] For the 180°C and 200°C esterification from figure 2.6 the average sizes are 137 nm^3 and 118 nm^3. Thus, the effective anisotropy constants are 422 kJ/m^3 and 321 kJ/m^3 respectively. These values are much larger than stoichiometric bulk values of ~225 kJ/m^3. [62,86]

For the conventionally synthesized nanoparticles two peaks appear in the d(FC-ZFC)/dT curve complicating the same calculation. These two peaks are mirrored in the volumetric distribution and so the average blocking temperature can be matched for each peak to the two separate lognormal distribution peaks to calculate two effective anisotropy constants, which then can be population averaged. The first average blocking temperatures from the two fitted peaks are 105K and 231K

corresponding to size peaks of volumes 301 nm^3 and 537 nm^3. Using again eq 1 for these individual peaks the effective anisotropy constants are 120 kJ/m^3 and 148 kJ/m^3 and when normalized for population density of the two peaks that the average k_{eff} for conventional particles is 121 kJ/m^3.

There are many possible reasons nanoparticle anisotropy constants deviate from that of the bulk measurements. Generally, throughout literature, it is common for CFO nanoparticles to have anisotropy constants lower than the bulk due to varied crystalline defects at the surface of the particles dominating the anisotropy. The anisotropy constant for the esterification particles is ubiquitously higher than the conventionally grown particles.[56–63] it is possible that the slower growth of the esterification particles leads to a more thermodynamic product with a more uniform surface of lower defects. Regardless of the reason the esterification process offers a method to generate a higher quality magnetic material than is seen in conventional methods.

4. CONCLUSION: We have shown a facile method for low temperature size-controlled synthesis of cobalt ferrite nanoparticles as a natural expansion on the work of Chang et al. The mechanism of formation is shown to be primarily through esterification of precursors, particularly at low temperature, and no auto decomposition of the precursor occurs. A varied range of nanoparticle sizes and with low size dispersion can be made with this method and batch scalability is shown. Multiple stoichiometries are accessible for further tuning of nanoparticle properties. Furthermore, we have shown that magnetic nanoparticles generated through these means also have improved magnetic properties. This has been shown through a $d(\mathrm{ZFC\text{-}FC})/dT$ curve analysis on magnetic nanoparticle data. Through this analysis we show that the particles herein created have a higher inherent crystalline anisotropy than those made from literature heat up methods.

We anticipate both that this method for producing CFO nanoparticles will be an improvement from earlier methods in both quality and ability to produce large quantities of particles. It expands the growing field of continuous growth methodologies, which utilize chemical properties for greater

control of nanoparticle properties. We expect this method to be widely applicable to form a wide variety of cobalt ferrite nanoparticles for a wide range of applications.

CHAPTER 3: CHEMICAL SYNTHESIS AND ADHESION OF MAGNETOSTRICTIVE IRON GALLIUM NANOPARTICLES

3.1 INTRODUCTION: Nanoscale magnetostrictive materials have many exciting potential applications, particularly when formed into composite multiferroic systems.[8,9,89] Magnetostrictive materials have been proposed to power the internet of things by functioning as minute energy harvesters.[37,90–92] These materials also have been shown to be a logical choice for a new generation of minute field sensors, particularly, for materials that show a high strain response to small applied fields.[93–95] Nanoscale magnetostrictives have even found their way into biomedical applications where strain from an alternating magnetic field applied to magnetostrictive have been used to induce bone growth.[96,97] As the application space continues to expand, the demand for new and better nanoscale magnetostrictive materials continually expands.

Broader nanoscale adaptation of magnetostrictive materials has been slowed by magnetostrictives tendency to have high magnetic crystalline anisotropy, and a tendency to utilize rare-earth elements.[8] Most commonly, high magnetostriction derives from strong spin orbit coupling in a strong magnetic crystalline anisotropy (MCA) energy. A minor distortion of the lattice in a high MCA material result in a large magnetic energetic change, and thus, high magnetostriction.[8,9] However, a high MCA intrinsically means that a large field is required to saturate the magnetization of the material and thus reach maximum lattice distortion from the magnetostriction. Such, high MCA precludes many multiferroic applications.[9,92,93] Additionally, the strong spin orbit coupling needed for many magnetostrictives tends to be a product of the incorporation of rare-earth elements.[98–103] This is true of the particularly prevalent magnetostrictive, Terfenol-D, which takes advantage of a partially frustrated intermetallic of terbium dysprosium and iron to create a low coercivity high magnetostrictive material. However, the difficulty of synthesis combined with the price of rare earths creates a large incentive toward alternative magnetostrictive of more common

elements in less specific lattice structures.[104–106]

Iron gallium alloys are an attractive alternative to rare earth magnetostrictives due to impressive magnetostrictive coefficients at low saturation fields and using earth abundant elements; although the origin of this magnetostriction is not entirely understood.[107–116] Magnetostriction constants for iron gallium alloys can reach as large as 400 ppm with saturation magnetic fields in the range of 100-200 Oe with strong tensile strength, making it an ideal system for many multiferroic applications.[112,113] Initial measurements of high magnetostriction in single crystal systems showed magnetostriction increased monotonically with gallium content up until around 17% gallium.[106,108] In single crystals, the magnetostriction was thought to increase with gallium effects on the band structure of the material until high gallium content induced the create of negative magnetostrictive Fe_3Ga DO_3 crystal grains.[106,108,109,114] *Ab Initio* modeling of α-Fe alloy FeGa have reproduced high magnetostriction, implying the effects of gallium on the iron electronic band structure is alone sufficient to generate high magnetostriction.[112,113] More recent experiments have shown that artificially stabilizing the structure against DO_3 formation at high gallium content, via doping of copper or epitaxial pinning of structure, show an even larger enhancement of magnetostriction.[113,115] However, investigations into polycrystalline samples have implied that a great deal of the magnetostriction could stem from DO_3 nanocluster grains undergoing a tetragonal shift to DO_{22} within a largely A2 cubic matrix.[116–120] The puzzle is further complicated where papers have shown doping effects to increase FeGa magnetostriction possibly due to enhancement of crystal defects or further alterations to single crystal band structure.[121,122]

The implications of the debate extend to the design of nanoscale systems wherein creation of single crystal materials encounters new challenges. Sputtered polycrystalline thin films were made showing magnetostriction values lower than bulk single crystal materials but high enough for multiferroic applications.[123–125] Electrodeposition methods were shown to be able to generate both

thin film and nanowire architectures.[123,126–128] Thin film deposition methods were improved with introduction of epitaxy through underlayers or sputtered beam epitaxy to make single crystal forms improving the magnetostriction.[123,129–131] Even more recently the electrodeposited thin film iron gallium layers have been incorporated into multi-layer stacks to keep high magnetostriction while lowering the formation of eddy currents under applied voltages in multiferroic devices.[132,133] The vast majority of nano-structuring in iron gallium systems has focused on 2D and 1D architectures with little work in 0D nanostructures such as nanoparticles.

Nanoparticle architecture is an obvious next step in new nano structuring of iron gallium. Aside from the possible applications from nanoparticle architecture magnetostrictive, an accurate measurement of magnetostriction in intrinsically single crystal nanoparticles could offer a valuable data point in the debate over the origin of magnetostriction in iron gallium. To make a magnetostrictive multiferroic based synthesized nanoparticles need to be proper iron gallium composition and solution processable onto a strainable surface. So far, intermetallic Fe_3Ga particles have been chemically grown in carbon nano tube substrate.[11] A stoichiometric metal nitrate precursors were soaked into carbon nanotubes and then annealed at 500° C in a 50:50 argon H_2 mixture.[11] The nanoparticles generated in this method were monodisperse in size but adhered irreversibly inside the carbon nanotube matrix preventing use for generating a multiferroic device. To the best of our knowledge this is the only chemical or mechanical method reported for FeGa nanoparticles.

In this work, we show a wet chemical method for the synthesis of iron gallium nanoparticles. The method relies on the rapid reduction of stable iron and gallium precursors while excluding all potential sources for oxygen at the high reaction temperature. the particles described herein are mono disperse in size distribution, crystalline, and magnetically superparamagnetic. The nanoparticles are extremely susceptible to oxygen and it was necessary to conduct all work within an

argon atmosphere glove box. Finally, using the method developed by Sasaki et al. the particles were chemically adhered to a titania surface to show the potential for integration into multiferroic structures.[10] This has been shown to be a valuable first step to generating a multiferroic structure from nanoparticles.[24]

3.2 EXPERIMENTAL:

3.2.1 Preparation of oleate precursor: Metal acetylacetonate precursors were converted to oleate precursor through the reaction with benzoic acid under vacuum. In a 50 mL standard Schlenk flask, 0.35 mmol gallium (III) acetylacetonate (Aldrich, 99%) and 0.70 mmol Iron (III) acetylacetonate (Aldrich, 99.9%) were mixed with a stir bar in a solution containing 384 mg (3.15 mmol) benzoic acid (Aldrich, 99.5%) and 8 mL n-octyl ether (26.6 mmol, Aldrich, 99%). The solution was degassed at room temperature (RT) for ten minutes. The system was a 15-minute ramp up from RT, the solution was further dried under vacuum at 100 ºC for 30 minutes. Acetylacetonate was recollected in a dry ice cooled trap.

3.2.2 Synthesis of $Fe_{0.9}Ga_{0.1}$ nanocrystals: Air free transfer of 0.5 ml (1.12 mmol) of trioctylphosphine (Aldrich 97%) was injected into the solution to acts a surface caping ligand. Under argon, the 8 ml solution of oleate precursor was heated to 210° C. 4 ml of 1.0 M solution of lithium triethylborohydride in n-octyl ether solution was injected at temperature to the solution of oleate precursors. The reaction instantly turned black but was left at temperature for 30 to 120 minutes. The resulting nanoparticles were allowed to cool to ambient temperature. The solution was brought into an argon atmosphere glove box. A 1:9 dry isopropynol:dry methanol (Fisher, 99.7%:Fisher, 99.8%) solution was added to the flask. The nanocrystals were forced to crash out from solution by use of a neodymium magnet. The nanopowder was resuspended in 4 ml of dry hexanes. 1:9 dry isopropynol:dry methanol was added to the hexanes and the nanocrystals were again forced to crash out by a neodymium magnet. The resultant nanopowder was then resuspended in hexanes.

3.2.3 Preparation of adhered nanocrystals: For chemical adhesion of nanoparticles to a substrate, the ambient oxygen free method described by Sasaki et al. was used.[10] A silicon wafer with a ~100 nm titania surface layer was brought into an inert atmosphere box and submerged into a solution of nanocrystals suspended in hexanes. The sample was left to soak for 24 hours days. During this time, the substrate changes color and a partial monolayer of nanocrystals forms on the substrate in an inert atmosphere environment. A protective layer of gold was sputtered on top of this substrate to reduce oxygen contamination of the FeGa particles.

3.2.4 Preparation of air free XRD: A sample for XRD was prepared by drop-casting nanopowder from nanoparticles suspended in hexanes on a piece of aluminized mylar inside an oxygen free glove box. Another piece of aluminized mylar was used to cover the sample and the edges were sealed by heating the mylar to form an air tight seal. The XRD pattern was taken and background subtracted from an aluminized mylar standard.

3.2.5 Preparation of magnetometry samples: Magnetometry samples were prepared through the suspension of nanocrystals into paraffin wax (Fisher) to ensure an oxygen free environment. A concentrated solution of washed nanoparticles suspended in hexanes was then injected into melted paraffin wax. The wax was left at temperature as a liquid for ten minutes to evaporate excess hexanes. A fraction of the total wax was injected into a pill capsule, where it solidified and was then fitted for measurement in the SQUID magnetometer.

3.2.7 Instrumentation: Magnetic measurements were conducted using a superconducting quantum interference device (SQUID) magnetometer (Quantum Design, MPMS XL-5). Scanning electron microscope (SEM) images taken via JEOL JSM-6700F FE-SEM. Transmission Electron Microscopy (TEM) images were collected using an FEI Tecnai T12 quick room temperature microscope. X-ray diffraction (XRD) made use of a Panalytical X'Pert Pro X-ray Powder Diffractometer operating with a Cu source.

3.3 RESULTS AND DISCUSSION: The crux of FeGa nanoparticle synthesis is the importance of excluding oxygen in various forms from the system. To remove trace air and water from the reaction, the synthesis of nanoparticles was performed on an air free Schlenk line set up where all precursors were dried under vacuum at temperature. Furthermore, it has been proposed in the literature that acetylacetonate ligands generally are able to participate in reactions with reducing agents during high temperature nanoparticle synthesis.[12] As such, it was quickly discovered that any attempts at synthesis of FeGa particles using acetylacetonate precursors would yield oxidized nanoparticles regardless of the strength of reducing agent used. Therefore, the switch from a dicarbonyl metal ligand to a more stable carboxylate ligand was necessary to prevent oxygen scavenging during the reaction and formation of oxide nanoparticles.

TEM images of synthesized particles appear in figure 3.1. The particles show very low dispersion of size and shape and have an average diameter of 5.5 nm and a standard deviation of 1 nm. An XRD pattern is shown in figure 3.1d showing the characteristic peaks of a BCC alloy of iron gallium. The <110> peak being the most intense and also shifted to slightly lower 2θ due to the introduction of large gallium atoms into the lattice. Additionally, EDS measurements of the nanoparticles indicate that the particles are $Fe_{0.9}Ga_{0.1.}$ The final iron to gallium ratio is lower than the to the stoichiometric ratio of the precursors used for synthesis of 2:1 Fe:Ga. This is likely due to the relative difficulty of reducing gallium during the synthesis. It is possible to yield a set of stoichiometries by changing the precursor stoichiometries.

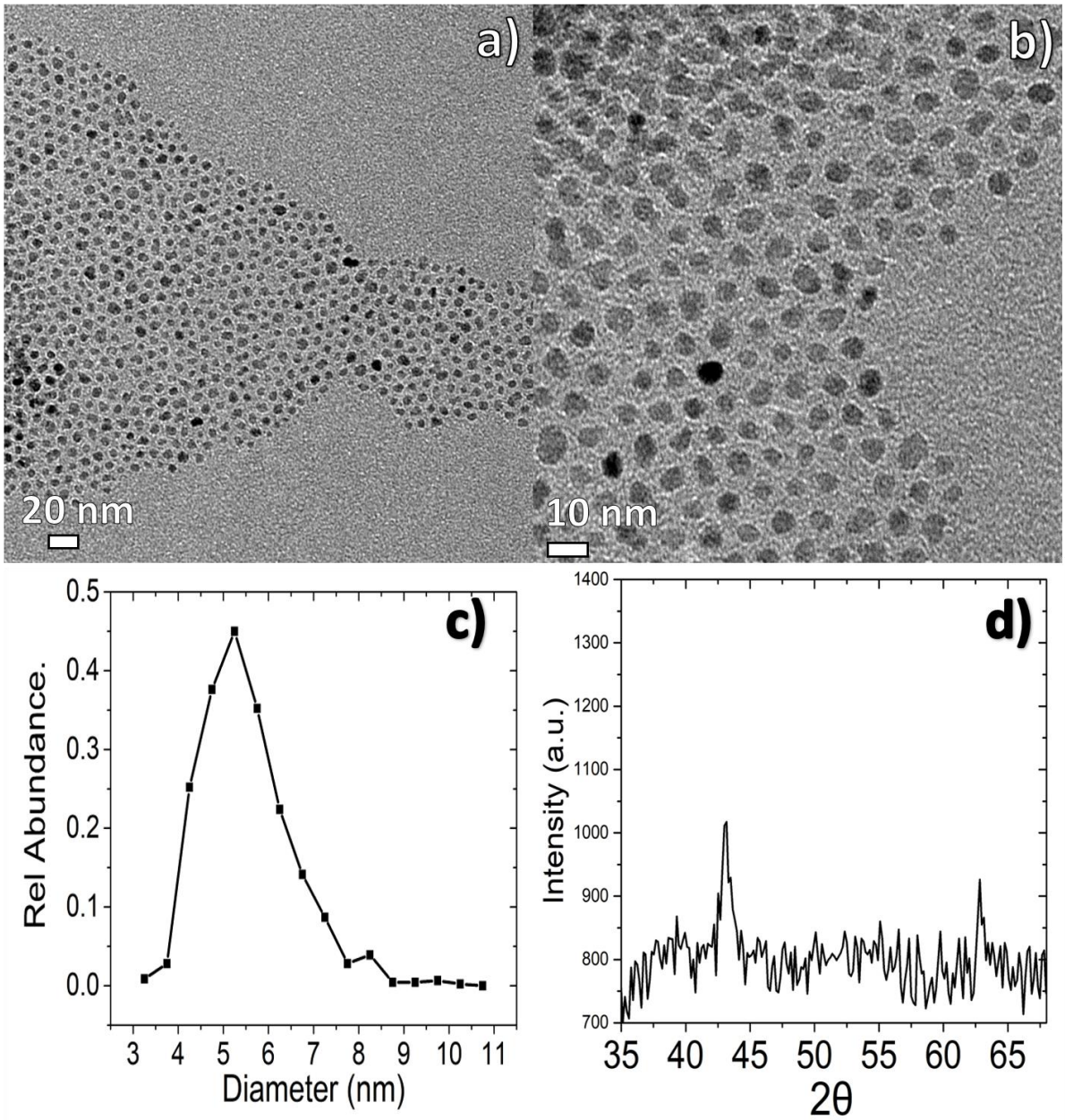

Figure 3.1 a),b) TEM of FeGa nanoparticles showing low dispersity of size. EDS confirms particles are $Fe_{0.9}Ga_{0.1}$ c) Histogram of nanoparticle diameters determined through imageJ d) XRD of synthesized particles

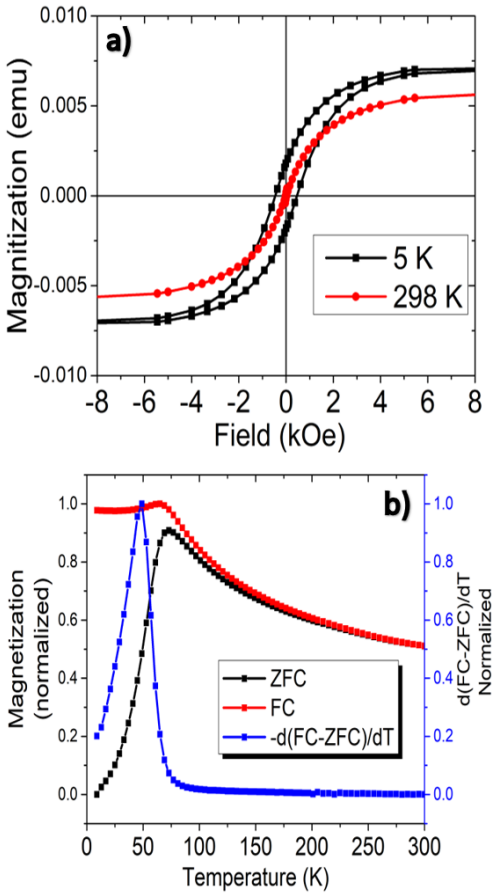

Figure 3.2 a) MH loops of as synthesized nanocrystals suspended n paraffin wax. At room temperature the particles are clearly superparamagnetic with no detectable coercivity. At 5K the ferromagnetic particles show a coercivity of around 500 oe. b) Zero field cooled (black) and field cooled (red) curves for $Fe_{0.9}Ga_{0.1}$ Particles. The ensemble blocking temperature from ZFC is 65K. blocking temperature distribution (-d[FC-ZFC]/dT) shows an average blocking temperature at 49K and a narrow distribution of blocking temperatures indicating good chemical uniformity of particles.

Magnetic analysis of the nanoparticles showed that the particles were superparamagnetic at room temperature and became ferromagnetic at extreme low temperature. Particles suspended in paraffin wax were measured using a SQUID magnetometer. MH loops for the as synthesized particles appear in figure 3.2a. The particles are clearly ferromagnetic at low temperature, 5K, with a coercivity of ~500 Oe. The coercivity disappears quickly with elevated temperature and the particles return to superparamagnetic with zero measurable coercivity. A room temperature MH loop appears as well to show the superparmagnetic nature of the particles.

The distribution blocking temperatures were probed through zero field cooled and field cooled measurements. Because the measurements were performed on particles spaced with paraffin wax, there should be no contributions to anisotropy from inter particle interaction. The ZFC curve shows an ensemble blocking temperature of 65K. Average blocking temperature can be more accurately judged via a calculated $d(\text{ZFC-FC})/dT$ curve wherein the derivative of the difference between the field cooled and zero field cooled measurements is calculated as described by Micha et al.[84] This curve, in blue in figure 3.2b, shows the population of nanoparticles

with the given blocking temperature and thus can be seen as a way of more precisely calculating a true average blocking temperature. The calculated average blocking here was 49K.

From the average blocking temperature and using the size distribution seen above an effective anisotropy constant for the particles can be calculated by use of equation 1.

(1) $T_b = \frac{K_{eff}V}{k_b \ln(\frac{t}{t_o})}$

Here the natural log of the sampling frequency can be estimated at 25 as is described in literature.[84,134] Calculating the effective anisotropy constant yields 194 kJ/m^3. While this is higher than the anisotropy associated with bulk iron, 48 kJ/m^3, it is far lower than measured anisotropy constants of iron nanoparticles. Nanoparticle effective anisotropy constants are generally much higher as they are enhanced by anisotropy contributions from surface and shape. As such a pure iron nanoparticle anisotropy has been measured closer to 550 kJ/m^3.[135] The nonmagnetic gallium while increasing the magnetostriction, should have this effect of lowering the effective anisotropy constant by both being non-magnetic and growing the lattice through the size of gallium. The calculated anisotropy constant from this work mirrors the relationship seen between iron and iron gallium in bulk systems where iron gallium magnetocrystaline anisotropy has been measured to be near 30 kJ/m^3.[136]

To show the applicability of the iron gallium nanoparticles to multiferroic structures the nanoparticles were chemically adhered to a substrate. Adhesion was done through a passive chemical reaction between the iron gallium nanoparticle surface and a surface of titania rich in oxygen as has been previously described.[10] The passive adhesion allows for the creation of a partial monolayer of nanocrystals on a substrate surface while maintaining the magnetic properties of the nanoparticles. After the adhesion reaction the nanoparticles were coated in a protective layer of gold sputtered onto the entire substrate. While the gold prevents visual inspection of the nanoparticles via SEM, the magnetic properties of the particles were probed through SQUID magnetometry the results of which appear in figure 3.3.

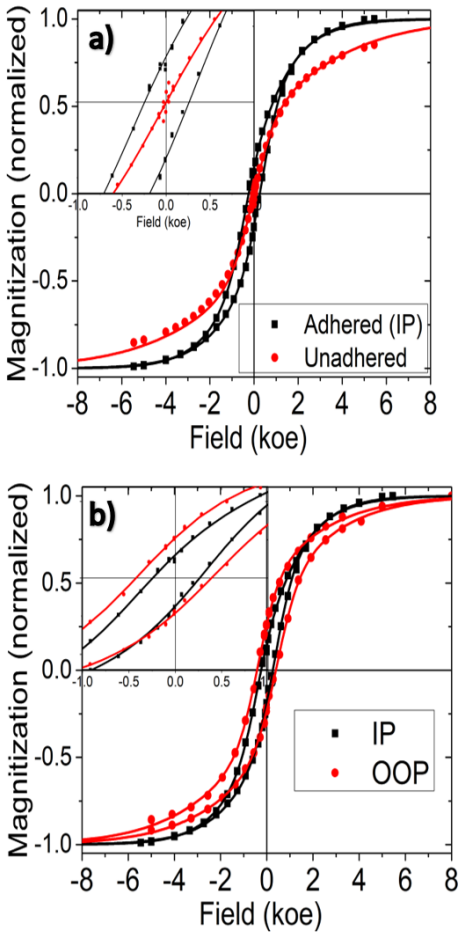

Figure 3.3 MH loops of nanoparticles after adhesion to a titania surface on a silicon substrate. a) a comparison of the as synthesized nanoparticles (red) and an in-plane measurement of the nanoparticles on a substrate. as synthesized nanoparticles are superparamagnetic, however, adhered particles have noticeable coercivity. b) comparison of magnetic properties in-plane and out-of-plane. The adhered particles show a preferential axis in plane.

The MH loop of adhered particles shows that post adhesion the particles are no longer superparamagnetic, but rather have a coercivity of around 300 oe. This is likely due to a number of new sources of anisotropy. Most simply, the adhered particles are much more densely packed and dispersed in a conductive medium, gold. The close proximity naturally increases any potential dipole coupling between the particles adhered to the plate. Further, it has been shown that a highly conductive medium between near nanoparticles can increase coercivity

by increasing the exchange coupling between the particles.[24] However, even more importantly than interparticle forces, adhesion of the particles to a surface involves a reaction between the surface of the particles and oxygen in the titania surface. This likely causes deformation of the nanoparticles as they elongate to interact with the titania surface to a larger degree, effectively wetting the surface. The additional strain applied to the particles thus can act as a new source of anisotropy. Additionally, this strain can cause the particles to be pinned by the substrate increasing the anisotropy due to the inability to change shape as the wax enmeshed particles can.

Further elucidation to the new anisotropy can be seen in figure 3.3b which features a comparison of an in-plane and an out-of-plane magnetization measurement. The adhered nanoparticle ensemble shows a preferential direction in-plane resulting in a squarer curve with lower coercivity in this geometry. In-plane preference further implies that newly applied strain is the culprit for the increased anisotropy of adhered nanoparticles as any applied strain should be positive in the in-plane direction. Because iron gallium is a positive magnetostrictive, strain of the nanoparticles in plane would contribute to the preferred axis in the plane of the adhesion. Finally, this is a promising result for later integration of the nanoparticles into functional multiferroic structures as adhesion to a strainable substrate is straight forward.

3.4 CONCLUSION: We have shown a facile method for the synthesis of an iron gallium, galfenol, nanoparticle with low size and shape dispersion and promising magnetic properties. The material was characterized through both crystal structure, stoichiometry, microscopy and through effective magnetocrystaline anisotropy constant. The work is a natural next step in the creation of galfenol nanostructures. Further, the nanoparticle was shown to be easily integrated into potential devices.

The work here should show the ease of generating iron gallium nano structures through wet chemical methods. it shows too that these materials can be utilized in the fabrication of the multiferroic systems. We anticipate that the nanoparticles will show excellent magnetostrictive

properties. Further it is likely the measurement of their magnetostriction could further help add to the ongoing investigation of the source of giant magnetostriction in galfenol alloys.

CHAPTER 4: INVESTIGATION OF NANOPARTICLE STRUCTURE TO LOWER PHASE CONVERSION ANNEALING TEMPERATURE

4.1 INTRODUCTION: The key to a large portion of computer memory devices remains magnetic moments. Magnetism offers high information density in a non-volatile format. Unfortunately, these systems require high energy for both the deposition methods used for their construction and also for their write functions.[137,138] Wet chemical synthesis of nanoparticles offers a low energy route towards high density bits which have potential to have low write energies.[137,138] Chemical synthesis too circumvents high energy deposition of elements.[139]

Specifically, in the last twenty years iron platinum nanoparticles have been heavily investigated as a potential high-density data storage material.[139] These particles are easily synthesized and also show extremely high out of plane coercivity. However, common in the literature is the need for extremely high annealing temperatures to achieve these coercivities.[140,141] The high uniaxial coercivity is a result of the high magnetocrystaline anisotropy of the L1o phase of FePt. The high annealing temperature required for this transformation in FePt nanoparticles has provided a road block for many years.

In bulk and even thin film samples of FePt, this required annealing temperature is vastly lower.[142] While nanoparticle literature tends to anneal at 700° C, temperatures as low as 230° C have been used effectively in specifically designed thin film structures.[142] However, phase transformation in most nanoparticle studies becomes pinned by regions of atomic composition imbalance.[143] These imbalances in structure require long distance atomic diffusion which creates the need for the high temperature annealing. [143] The source of these imbalances in synthetic method generally is not addressed and it is important to investigate possible sources for the high annealing temperature.

The high temperature annealing is likely a symptom of the general difficulty of synthesizing binary or higher nanoparticle systems.[144–149] Particularly for an alloy of highly differential metal

properties, the simultaneous reaction and mixing of a bulk stable alloy can be complicated by reaction kinetics. The problem is augmented by the difficulty in precise measurement of nano materials. As such, it is necessary to both precisely measure nanoparticles to get a full picture of the nanostructure and then to tailor synthesis to control kinetic difficulties arising from high energy synthesis.[144,149]

In this work, we report a method of investigating nanoparticle properties combined with other nanoparticle defining analysis which can provide vital information in improving the quality of the nanoparticles. The reduction in required annealing temperature for FePt $L1_o$ nanoparticles is used as an example system by which the value of this investigation is shown. It is clear from the analysis of the nanoparticles through combined EDS and XPS measurements it is possible to greatly improve the value of the nanoparticles. Annealing conditions are made less extreme by a change in the architecture of the nanoparticles via a reworking of the method.

4.2 EXPERIMENTAL

4.2.1 Synthesis of heat up FePt nanoparticles: Synthesis of heat up FePt nanoparticles was done through a modified method by Sun et al. a 50 ml Schlenk flask was charged with 1.0 mmol (0.250 grams, Aldrich 95%) hexadecanediol dissolved in 8 ml of dioctyl ether (TCI), 3 ml (11 mmol, Sigma 90%) of oleic acid and 5 ml (15 mmol, Sigma 70%) oleylamine. 0.6 mmol (0.235 g, Sigma 99%) of $Pt(acac)_2$ was dissolved into the solution. The solution was heated to 110° C and dried under vacuum for 30 minutes. In a separate container, 2ml (6 mmol, Sigma 70%) of dry oleylamine and 2 ml n-octyl ether was used to dissolve 0.6 mmol (0.08 ml Sigma 99%) of $Fe(CO)_5$ At the end of the drying process the 50 ml Schlenk flask was purged three times with argon. The $Fe(CO)_5$ solution is injected into the Schlenk flask and the flask was ramped to 300° C. The solution turns black before the end of the ramp. After a 45-minute soak at temperature the solution is cooled to room temperature. The

nanoparticles are then washed three times with ethanol and nanoparticles are collected through centrifuging. The product is then resuspended in hexanes.

4.2.2 Synthesis of hot injection FePt nanoparticles: Synthesis of hot injection FePt nanoparticles is done in an identical way except that the $Pt(acac)_2$ is not added to the 50ml Schlenk flask but rather to the injected solution. Further, the Schlenk flask solution is heated to 300° C prior to injection. Injection is done as rapidly as possible to attempt to ensure reaction occurs instantaneously. The solution turns black immediately after injection. The solution is left to soak for 45 minutes and then cooled to room temperature. The solution is washed three times with ethanol and nanoparticles are collected through centrifuging. The nanoparticles are resuspended in hexanes.

4.2.3 Creation of partial monolayer samples: Nanoparticles were deposited on silica plates by dipping silica in a dilute solution of nanoparticles in hexanes. The hexane was allowed to slowly evaporate depositing a sub monolayer of nanoparticles onto silica plates. The nanoparticles were then coated using a sputterer to apply 20 nm of gold to the surface of the plate over the nanoparticles.

4.2.4 Annealing Studies: Films were annealed in alumina tube, under flowing forming gas (5% H_2, 95% Ar). A magnetic field of ~3000G was applied via an electromagnet surrounding the alumina tube containing the sample. The samples were held in place with a holder so that a field was applied perpendicular to the sample.

4.2.5 Instrumentation: Magnetic measurements were conducted using a superconducting quantum interference device (SQUID) magnetometer (Quantum Design, MPMS XL-5). Oxidation potential of surfaces and samples carried out using X-ray Photoelectron Spectroscopy (XPS) from a Kratos Axis Ultra DLD spectrometer with a monochromatic Al (Kα) radiation source. Scanning electron microscope (SEM) images taken via JEOL JSM-6700F FE-SEM. Transmission Electron Microscopy (TEM) images were collected using an FEI Tecnai T12 quick room temperature microscope. X-ray

diffraction (XRD) made use of a Panalytical X'Pert Pro X-ray Powder Diffractometer operating with a Cu source.

4.3 RESULTS AND DISCUSSION: The general synthetic method for the wet chemical production of FePt uses a fast-heating ramp from low temperature on a precursor solution.[140,141] However, despite common literature consensus that iron carbonyls decompose rapidly at low temperatures, the ramping rate gives precursors a window wherein platinum can reduce before iron carbonyl decomposes. Precursor mixtures as described in section 4.2.1 when heated to 220° and soaked for 45 minutes yield entirely platinum nanoparticles.[95,150] The implication being that from 220° C until sufficiently high temperature platinum precursors are forming nanocrystal nuclei while iron precursors are inert.

The general wisdom surrounding the use of iron carbonyls in nanoparticle synthesis is that they are so reactive as to form iron nanoparticles at room temperature. Thus, the idea that the only decomposing precursor by 220° C remains platinum, flies in the face of this understanding of iron carbonyls. It has been theorized that the iron carbonyl readily complexes with free oleylamine during the initial mixing of precursors to form a far more stable transition metal complex.[150] While the iron oleylamine complex becomes less reactive it also becomes less volatile, necessary for nanoparticle synthesis at 300° C. Reactions carried out with iron carbonyl but without oleylamine at elevated temperatures have yielded wildly fluctuating iron atomic percent as iron carbonyl untreated with oleylamine escapes the reaction mixture due to evaporation.

Because of this early opportunity for platinum nucleation, nanoparticles formed through heat up methods described in 4.2.1 generate a core-shell like structure for the final particle. In this structure a majority platinum core forms as the synthesis mixture ramps to reaction temperature. these cores are then coated by iron at sufficiently high temperature leading to a nanoparticle with poor atomic mixing. the atomic nanostructure of the synthesized particles can be probed through the combined

use of both XPS and EDS compositional studies. Key to this technique are the subtle differences between the two compositional spectroscopies. EDS spectroscopy uses accelerated high voltage electrons to remove core electrons from atoms. The valence electrons of the species relax into the core emitting x-rays. Because the ejected electrons propagate further and the x-rays are not reabsorbed by the materials, this technique suffers from spot size growth. Thus, it senses the material through a large depth giving a full picture of the composition of the total particle. However, XPS spectroscopy uses energetically precise x-rays to excite core electrons. The instrument detects the energies of emitted electrons. Any electrons that are emitted from the interior of the material are reabsorbed by that material, meaning the only signal generated by the instrumentation is that of surface atomic sites.

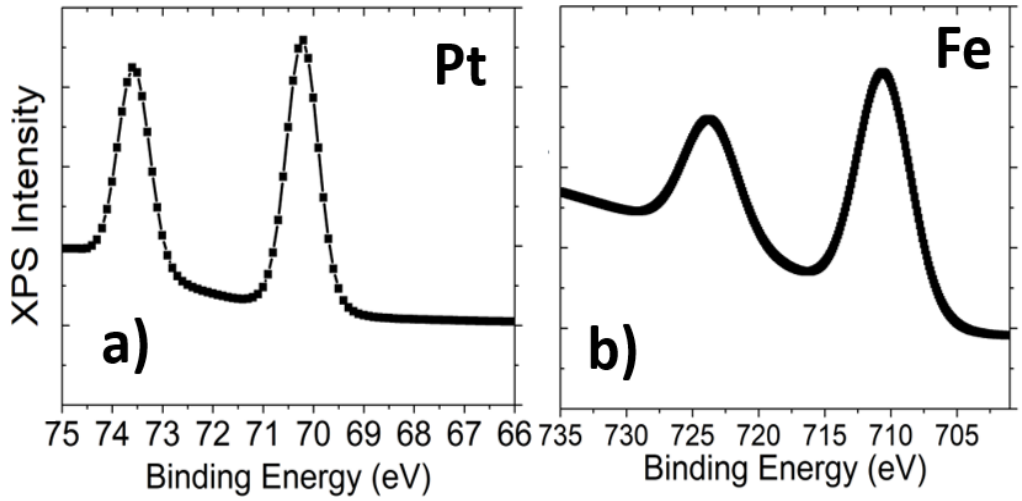

Figure 4.1 XPS results for heat up method synthesized FePt nanoparticles. Despite EDS measurements showing the nanoparticles are 1:1 Pt:Fe, the XPS results show only 9% Pt against 91% Fe implying a core shell structure.

Figure 4.1 shows XPS results for nanoparticles synthesized through a heat ramp rate. The XPS shows a ratio of 9% Pt compared to 91% Fe despite an EDS measurement showing 50:50 Pt:Fe. This is due to the high surface sensitivity of the XPS therefore implying a strong core shell local structure.

The platinum core formation can be eliminated by changing to a hot injection synthesis, as described above in section 4.2.2 The crux of the hot injection is that the reaction of the iron and the platinum is forced to occur simultaneously by only introducing both precursors when the reaction is at high enough temperature to cause the decomposition of both.

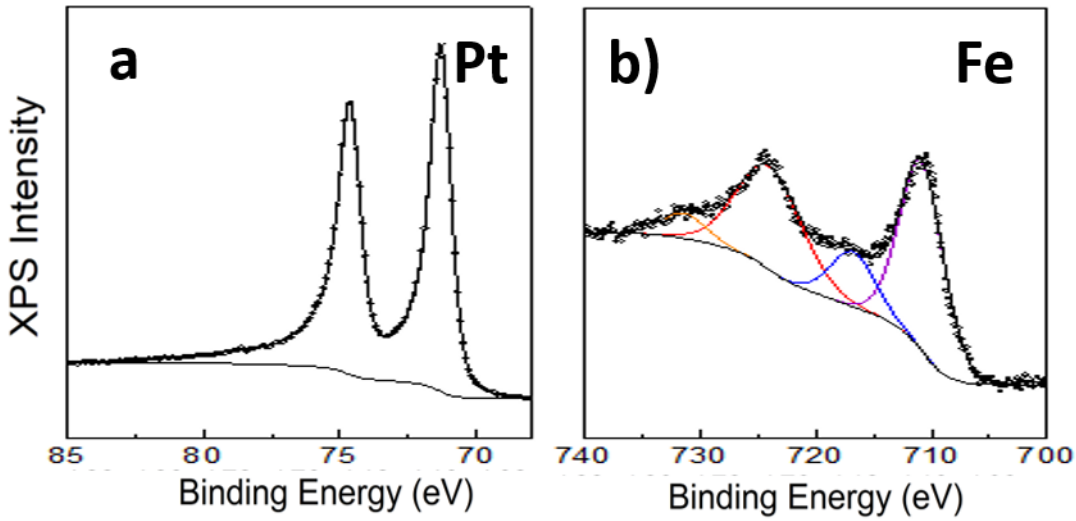

Figure 4.2 XPS results for hot injection method synthesized FePt nanoparticles. Despite EDS measurements showing the nanoparticles are 1:1 Pt:Fe, the XPS results show 38% Pt against 62% Fe much closer to a true randomized alloy.

Figure 4.2 shows the XPS results for hot injection nanoparticles. Again while the nanoparticles via EDS are 1:1 Fe:Pt, the XPS now shows 38:62 Pt:Fe. Clearly while, the method does not generate a perfectly stoichiometrically mixed nanoparticle, likely because the precursors do not react at the same rate, the particle is much closer to the desired randomized alloy necessary for annealing.

Furthermore, polydispersity and size are improved in the hot injection synthesis. As seen in figure 4.3, the as synthesized FePt nanoparticles are on average ~6 nm in diameter. All measured particles are within 5 to 7 nm in diameter implying a high degree of monodispersity. Figure 4.3 shows the physical properties of the nanocrystals through TEM imaging as well as XRD pattern of

the nanocrystals. Additionally, all particles were spherical, precluding the possibility of nanorods confounding the magnetic properties of the particles.

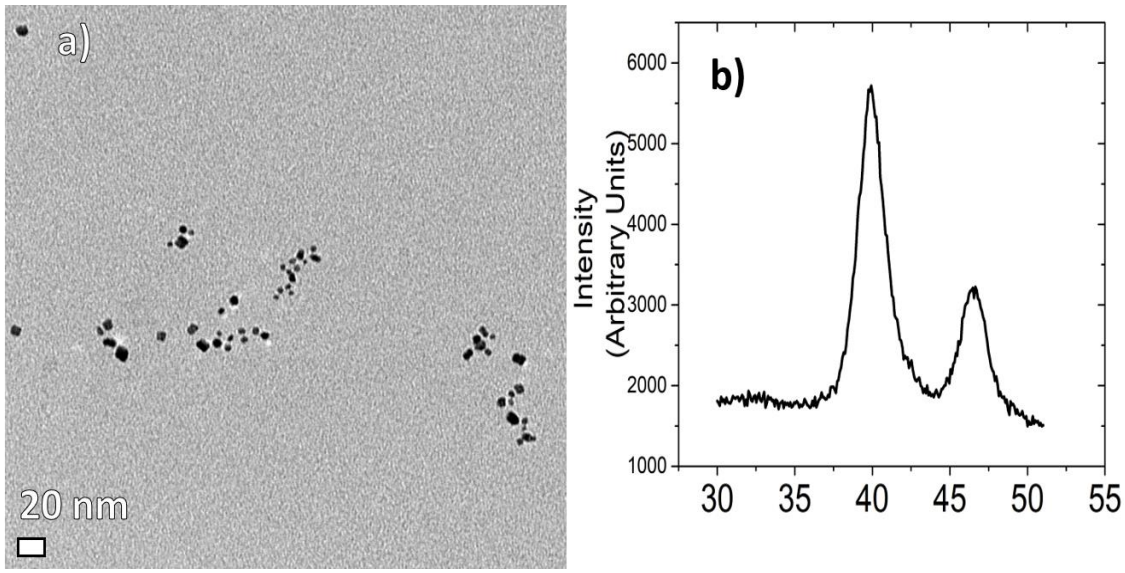

Figure 4.3 a) TEM images of FePt nanoparticles showing small size dispersity and size. b) XRD pattern for FePt nanoparticles showing <111> and <200> peak clearly.

Further investigation of the structure of the nanoparticles from the two methods was performed by comparison of the anisotropy distributions of the synthesized nanoparticles. This is done by generating a d(ZFC-FC)/dT graph as per Micha et al.[84] By taking the derivative of the difference in a field cooled and zero field cooled SQUID magnetization measurement, a graph of the distribution of nanoparticle blocking temperatures is generated. The blocking temperature can be assumed to be the product primarily magnetocrystaline anisotropy for the nanoparticles and generally shows a nearly log normal distribution due to the log normal distribution of nanoparticle sizes. The d(ZFC-FC)/dT graph appears in figure 4.4

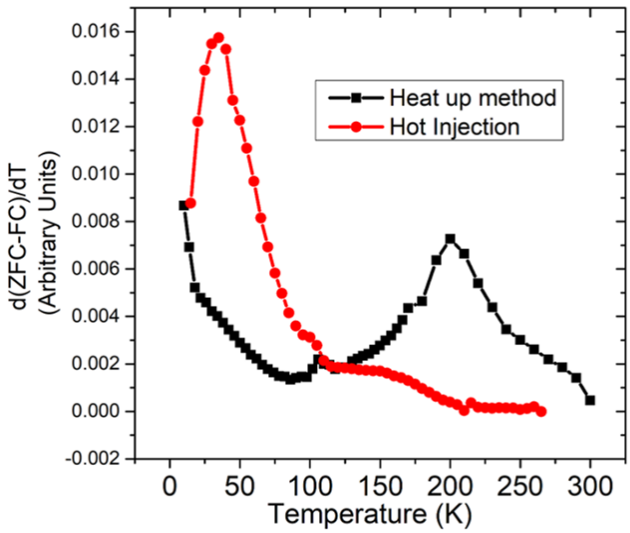

Figure 4.4 *d*(ZFC-FC)/*dT* graph for nanoparticles generated through a heat up method (black) vs a hot injection method (red). The hot injection method shows predominately one single peak of anisotropies implying one nanoparticle product, whereas the heat up method shows two clear peaks at extremely low temperature and another near 200K. This implies that in heat up methods multiple anisotropies exist due to the more complicated system of a core shell nanoparticle.

After magnetic annealing of the nanoparticles at a range of temperatures, magnetometry data indicates nearly complete conversion to the $L1_0$ FePt phase. M-H loops for a sample annealed at 550° C are shown in figure 4.5a. The remaining A1 phase material and the $L1_o$ material were fit separately to obtain the fit for the experimental data. The coercivity (H_c) for the sample via fitting was 10043. Oe, substantially more than has been seen at this temperature previous. The $L1_o$ phase from the fit has a H_c of 12695 Oe. From the difference in saturation magnetization of the fits for two phases we can determine the total percentage conversion of the sample. Because the $L1_o$ phase has a higher per atom magnetization, the saturation of the two phases must be weighted for this difference. After weighting, the it can be calculated that 85% of the sample is converted to the $L1_o$ phase.

The results of a series of annealing temperatures are shown in figure 4.5b. The hot injection method shows a clear lowering of the required annealing temperature. Clearly the change to hot

injection method has reduced the annealing temperature required to generate the $L1_o$ structure. Furthermore, use of combined EDS XPS shows high potential to reveal important structural information in bimetallic nanoparticles.

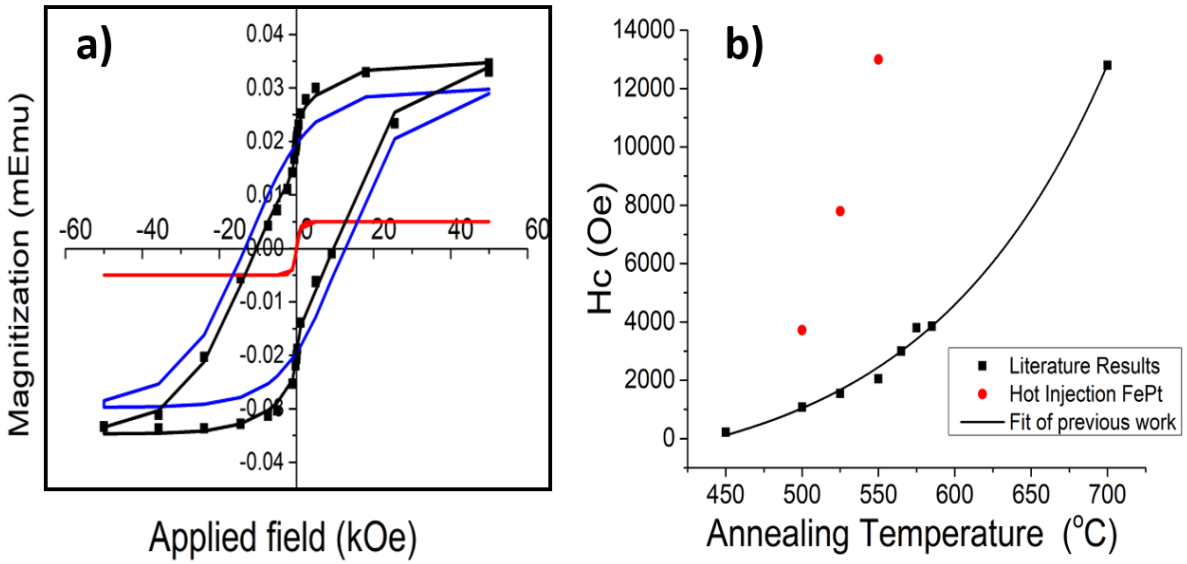

Figure 4.5 a) M-H loop out of plane of nanoparticle sample annealed at 550° C. Black curve is raw data showing 10kOe coercivity. Fitting of superparamagnetic unconverted signal (red) and ferromagnetic signal (blue) reveals true coercivity of ferromagnetic particles is ~13kOe and that conversion is 85%. b) results of annealing studies compared to literature values of nanoparticles synthesized via methods described by Sun et al. Hot injection nanoparticles show much lower required annealing temperatures.

4.4 CONCLUSION: We have demonstrated a form of nanoparticle analysis, which shows a great deal of utility toward revealing important nanoparticle attributes. This has been shown to be useful in the case of FePt nanoparticles, by revealing information about the nanoparticles that lead better potential for the particles to be used in devices. The presentation of this methodology should emphasize the potential of using this along with other methodologies such as anisotropy distribution curves to create a better quality of nanoparticle. The hope is to increase the utility of nanoparticles by showing better ways to analyze the product of nanoparticle synthesis.

CHAPTER 5: NOVEL MATHEMATICAL FITTING FUNCTION FOR TEMPERATURE DEPENDENT *d*(ZFC-FC)/d*T* NANOPARTICLE DISTRIBUTIONS

INTRODUCTION: Magnetic nanoparticles are essential to applications in many quickly growing fields. For many years drug delivery applications have utilized the unique properties of lipid or inorganic nanoparticles for exciting new cancer treatments.[30,40,151–154] Filtration and harvesting in aqueous systems has been accomplished with ease using clever design of nanoparticles.[155,156] Nanoparticles have potential as sensors of magnetic fields, due to inherent rapid saturation of a nanomagnet, and as a minute energy source for nanoscale devices via energetic harvesting.[157–159] Further, minute but stable magnetic bits made from nanoparticles can be used as a cost effective way to rapidly engineer computer memory devices.[35,137,159,160] Naturally, all of these application spaces are contingent on our ability to generate and accurately measure high quality synthesized nanoparticles.

Engineering a quality device from a given nanoparticle distribution is largely dependent on not just the average quality of the particles, but by the total range of the distribution. Whether made through top-down approaches such as ball milling or bottom-up approaches such as ligand mediated chemical growth, nanoparticle synthesis ubiquitously creates a dispersion of sizes and frequently a range of physical properties. The high energies required for synthesis of nanoparticles naturally leads to a variety of formation mechanisms and thus intrinsic variety of produced particles. [161] Research continues on any improvements toward narrowing nanoparticle size and thus, trait dispersions as in chapter 2.[162–166] Emphasis on uniformity of properties is especially true in nanomagnetic applications, where simple polycrystallinity can preclude certain materials from systems.[167–171] As such, the measurement of averaged or summed properties of nanoparticle distributions does not always suffice to describe a system, but rather, it is necessary to describe the entire distribution of particles and the many different physical properties within distributions.

A prime example of a physical property in magnetic nanoparticles wherein the ensemble and individual nanoparticle effects diverge importantly is in superparamagnetic attributes. Superparamagnetism is a magnetic behavior observed in nanoscale systems where the magnetic anisotropic energy of a ferromagnet is negligible compared to thermal energy.[8,172] Thus, the magnetization direction of the nano domain fluctuates at random just from thermal energetic randomization. The main result of the thermal switching is a superparamagnetic material has a time averaged net magnetization of zero. Thus, the magnetic attractive forces dissipate between particles and they are dispersible in a solution. Further, without any anisotropy the material will magnetically align with any applied magnetic field like a paramagnet, but with a high saturation magnetization like a ferromagnet.[8,172] Because the main contribution to magnetic anisotropy is the crystalline anisotropy, generally the superparamagnetism only exists in nanosystems where total anisotropy of the system is only sufficiently low. As such, the phenomenon is greatly size dependent, meaning that size dispersion within of nanoparticles can lead to a dispersion of superparamagnetic and ferromagnetic behaviors within the same synthesis.[8,172]

However, size dispersion is not the only complicating variable on nanoparticle anisotropy as many different anisotropy energies exist in magnetic nanostructures.[8,173] Aside from magnetocrystaline anisotropy (MCA), nanoparticles shape and surface can be a source of magnetic anisotropy. Magnetization direction is most energetically favorable along the longest axis of a structure creating shape effects, while surface defects can create a different anisotropy energetic landscape than seen in the bulk crystal.[8,173] Both of these effects are particularly pronounced in the nanoscale due to the relatively high ratio of surface area to volume.[39,172–175] Additionally nanocrystals are particularly susceptible to magnetic interaction between other local grains creating exchange and dipole anisotropy.[8,23,173,176–179] As such clusters of nanocrystals can have distinctly different magnetic behaviors from these interaction anisotropies.[179–181] Finally, magnetostriction can add an additional

form of anisotropy, but this is rare since this anisotropy is dependent on application of strain on nanocrystals.[10]

Characterization of the total anisotropy of a distribution of nanoparticles can be done through analysis of a zero-field cooled (ZFC) and field cooled (FC) magnetometry measurement. The temperature at which a nanoparticle transitions between a ferromagnetic and superparamagnetic state is called the blocking temperature (T_b). It can be determined from zero-field cooled experiments by freezing a nanoparticle ensemble under zero applied field, applying a small field, and then increasing the temperature of the sample and measuring the increasing magnetization of a sample aligning with the field as the nanoparticles of the sample transition to superparamagnetic.[85] Figure 5.1a shows a ZFC curve in black. The blocking temperature for the polysized ensemble is determined by the highest magnetization measured.

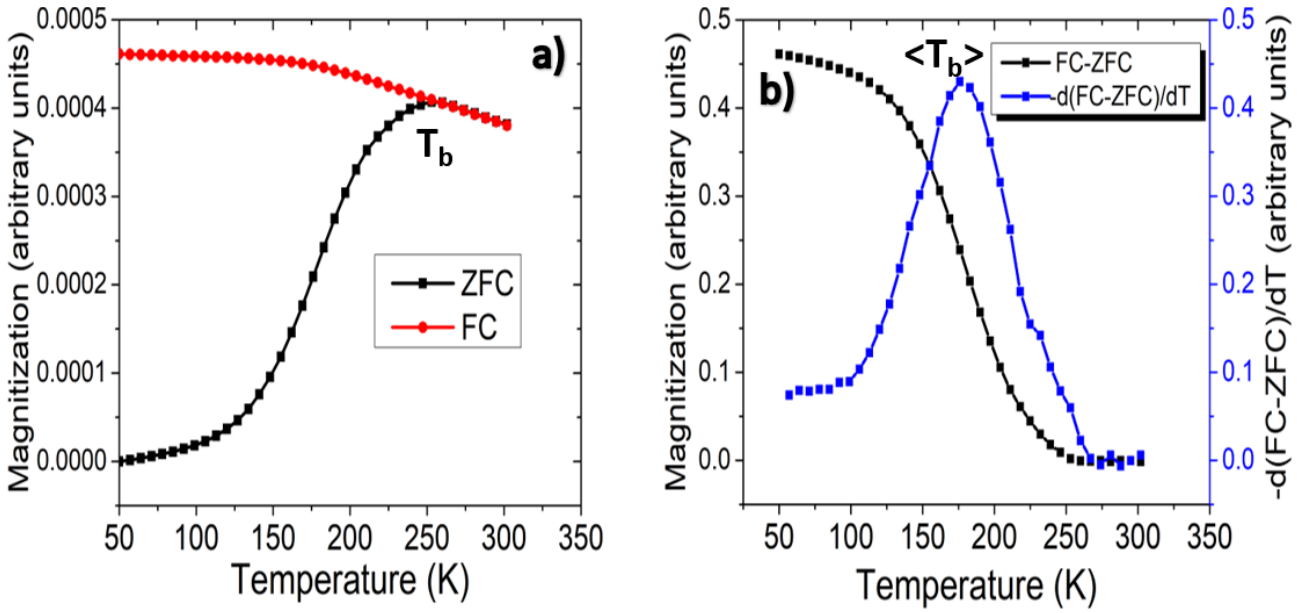

Figure 5.1 a) Example zero-field cooled (ZFC) (black) and field cooled (FC) (red). Blocking temperature for a polysized sample is at the peak of the ZFC curve. b) Difference between FC and ZFC curve shown in a). Derivative curve of the difference curve is shown in blue. Average blocking temperature of the nanoparticles in the ensemble is the peak in this curve. Determination of blocking temperature through this method results in a much lower calculated blocking temperature than in the curve from a.

After this point the magnetizations of the nanoparticles are further randomized by temperature and total signal drops. Because the sample of nanoparticles has particles of many different sizes, many different total anisotropies and thus blocking temperatures are expected. The smallest nanoparticles of the sample transition back to random magnetization before the ZFC curve reaches a peak, thus leading to difficulty measuring blocking temperature just through ZFC. The return to random magnetization can be measured using a Field cooled (FC) sample, which is the same experiment except performed on an ensemble that is fully aligned prior to measurement. By taking the difference between these two measurements, figure 5.1b, a measurement of only nanoparticles aligning to the field can be made. The derivative of the difference as is seen in blue in figure 5.1b, thus is a representation of the blocking temperatures of the sample by showing the temperatures at which the signal is changing the fastest.[85,182] Generally this blocking temperature is considered a better representation of the real distribution blocking temperatures of the individual particles.[85]

The shape of the derivative curve should be determined by the distribution of total anisotropy for each individual nanoparticle.[85,182] If it is assumed that the largest contribution to the anisotropy should be magnetocrystaline anisotropy then the curve should follow the shape of the size distribution of the nanoparticles, which is generally a log-normal distribution.[182–185] Thus, fitting the derivative cure to a log-normal function generally works, particularly in systems where the blocking temperature is at a low enough temperature that the entire derivative curve cannot be measured. [22,85,182,186,187] However, frequently a lognormal curve fails to fully characterize the shape of the blocking temperature distribution curve, as is the case of the curve presented from experimental data in figure 5.1b. [22,188,189] So while these curves can retain the general asymmetric peak shape from MCA and a lognormal volume distribution, for systems with additional anisotropies the curve will deviate from a log normal shape.[22,188,189] The various sources of anisotropies also add difficulty to calculation of single anisotropy constant for a nanoparticle material. Generally, calculation of an

"effective" anisotropy constant has been done as a means of avoiding this complication but the values for these constants can vary wildly between papers and synthetic methods.[22,39,187,189–191]

Attempts to reconcile the many interacting physics in blocking temperature distributions of nanoparticles have become more common as a precise calculation of average anisotropy constant can give vital information about a synthetic method for nanoparticles.[22,186,188,192] An understanding of the entire distribution of anisotropies in an ensemble of particles is even more elucidating. Recently, Batley et al. used fitting of anisotropy constants across a number of nanoparticle distributions partially to understand the fine structure of nickel nanoparticles with a nickel phosphide coating.[22] Work has also used anisotropy constants to describe observed changes in lattice or stoichiometry in difficult to characterize systems.[193,194] Precisely calculated anisotropy constants can also be used to display differences in synthetic mechanism of particles as in chapter 2. However, difficulties remain. One main issue is the method for measuring blocking temperature, FC-ZFC curves, is a temperature-based measurement while magnetic anisotropy is a known to be temperature dependent.[195] Calculating a temperature dependent anisotropy constant for nanoparticles has been shown to be useful in justifying the effective anisotropy constants calculated for nanoparticles. [22,196–198] However, most work has stopped short of combining temperature dependence of anisotropy with a rigorous way of calculating multiple forms of anisotropy in nanoparticle full distributions.

In this paper, we mathematically fit experimental $-d(\text{FC-ZFC})/dT$ curves of multiple nanoparticle distributions including two different materials as well as many variations on those main materials. The mathematical fitting is done with a novel formulation of a $-d(\text{FC-ZFC})/dT$ curve fitting function, which is able to calculate the relevant anisotropies for an entire distribution of nanoparticles and create a fuller energetic picture of the nanoparticles. The main two test systems are high intrinsic MCA material, cobalt ferrite, as well as a low MCA material of metallic nickel nanoparticles. To determine the fitting function of the derivative curves from MCA, the

nanoparticle distributions are carefully characterized for size through TEM. Further, it is shown that for low MCA materials such as nickel, both shape and surface anisotropies must be added to the fitting function in order properly characterize the a -d(FC-ZFC)/dT curves. The shape distributions are also found via the analysis of TEM images. In addition, intrinsic anisotropy constants are justified using EDS data. With all this information we explicitly model the temperature dependent anisotropy for the nanoparticle distribution. From these it is shown that many chemically valuable conclusions can be drawn using this fitting system.

5.2 EXPERIMENTAL:

5.2.1 Low temperature synthesis of cobalt ferrite nanocrystals: Low temperature synthesis was carried out as described in chapter 2. In a 50 mL standard Schlenk flask, 0.194 mmol cobalt (II) acetylacetonate (Aldrich, 97%) and 0.399 mmol iron (III) acetylacetonate (Aldrich, 99.9%) were dissolved in a mixture of 5 mL oleic acid (15.75 mmol, Panreac, purified by distillation) and 6 mL n-octyl ether (19.95 mmol, Aldrich, 99%). The solution was degassed at room temperature (RT) for ten minutes. The temperature was increased to 100° C over 15 minutes and dried under vacuum for an additional 30 minutes. Under argon, 4 mL 1-decanol (20.95 mmol, 'Baker', 99%) was added. The mixture was heated to 200 ºC with a 15-minute ramp period and held for 180 minutes. The resulting nanoparticles were cooled to RT. 50 mL ethanol was added to the reaction mixture and the mixture was centrifuged at 4000 RPM to induce precipitation of the nanocrystals. The solution was decanted from the particles. The product was then re-dispersed in hexanes and washed with ethanol twice before being dispersed in hexanes.

5.2.2 High temperature synthesis of cobalt ferrite nanocrystals: High temperature synthesis of CFO nanocrystals was performed following an oxygen-free procedure adapted from Lu et al.[199] 63.0 mg cobalt (II) acetylacetonate (0.245 mmol, Aldrich, 97%), 125 mg Iron (III) acetylacetonate (0.354 mmol, Aldrich, 99.9%), and 155 mg 1,2-hexadecandiol (0.600 mmol, Aldrich, 90%) were dispensed

to a 50 ml Schlenk flask. A mixture of 6 mL oleylamine (18.24 mmol, Panreac, purified by distillation), 2 mL oleic acid (6.3 mmol, Panreac, purified by distillation), and 4 mL n-octyl ether (13.30 mmol, Aldrich, 99%) was added to dissolve the metal precursors, The solution was heated and then dried under vacuum at 100º C for 30 minutes. The flask was purged with argon three times. Under argon, the mixture was heated to 250 ºC with a 15-minute ramp period and held for 30 minutes. The reaction was cooled to RT. 50 mL Ethanol was added and the solution was centrifuged at 4000 RPM to precipitate particles. The solution was decanted, and dispersed in hexanes. The product was then washed with ethanol twice before being re-dispersed in hexanes.

5.2.3 High temperature synthesis of nickel nanocrystals: Nickel nanocrystals were synthesized using a modified procedure from Carenco, S. et al.[14,21] A 50 mL Schlenk flask was charged with 2 mmol nickel acetylacetonate as well as 9.5 mmol oleylamine (3.0 mL), 1 mmol oleic acid (0.315 mL), and 7.3 mL n-octyl ether (24.3 mmol, Aldrich, 99%). The total solution was dried at 100º C and purged with argon three times. 0.45 mmol trioctylphosphosphine (0.2 mL) was injected into the solution via air free injection. The solution was then refluxed under an inert atmosphere at 220 ˚C for 45 minutes (ramp rate 3 ˚C/min) and then rapidly cooled to room temperature. The flask was closed to atmosphere and transferred to an air free atmosphere glovebox. A 1:9 dry isopropynol:dry methanol (Fisher, 99.7%:Fisher, 99.8%) solution was added to the flask. The nanocrystals were precipitated from solution by use of a neodymium magnet. The nanopowder was resuspended in 4 ml of dry hexanes. The nanoparticles were washed again with addition of 50 mL of 1:9 dry isopropynol:dry methanol and precipitation via a neodymium magnet. The resultant nanopowder was then resuspended in hexanes.

5.2.4 Low temperature synthesis of nickel nanocrystals: For bare surface nickel nanocrystals, a similar process as described above in section 2.3 was used with the following modifications. The same precursors and solvents were injected into solution and dried at 100º C. After injection only

0.18 mmol trioctylphosphosphine (0.08 mL) was injected into the solution via air free injection. The solution was then ramped to 190° C at a rate of 1.5 C/min. The reaction temperature was held for 120 minutes and then cooled to RT. Purification of the nanopowder was done as described above In section 5.2.4.

5.2.5 Preparation of magnetometry samples: Magnetometry samples of oxide nanocrystal were prepared through the suspension of nanocrystals into paraffin wax (Fisher). The wax was melted and a solution of nanocrystals in hexanes were added to the melted wax. The hexanes were driven off at elevated temperature for 10 minutes. The wax was then allowed to cool freezing the dispersed nanoparticles far apart. A fraction of the total wax was injected into a pill capsule, where it solidified. The pill capsules were then fitted in straws for measurement in the SQUID magnetometer. For air sensitive nickel nanoparticles, the same process was followed except inside an oxygen excluding glovebox with an argon atmosphere. To ensure a complete lack of oxidation of the nanocrystals, SQUID magnetometer samples were also prepared in an argon atmosphere box. The pill capsules set in straws were fit into centrifuge tubes within the box, and brought to the SQUID magnetometer under argon atmosphere. The wax was briefly exposed to oxygen only during transfer from the centrifuge tube to the SQUID magnetometer. The magnetometer was then purged for analysis removing all oxygen.

5.2.6 Instrumentation: Magnetic measurements were conducted using a superconducting quantum interference device (SQUID) magnetometer (Quantum Design, MPMS XL-5). Electron Dispersion Spectroscopy (EDS) data was taken via JEOL JSM-6700F FE-SEM. Transmission Electron Microscopy (TEM) images were collected using an FEI Tecnai T12 quick room temperature microscope. X-ray diffraction (XRD) made use of a Panalytical X'Pert Pro X-ray Powder Diffractometer operating with a Cu source.

5.3 RESULTS AND DISCUSSION: Several distributions of nanoparticles were generated and

characterized to investigate different sources of anisotropy represented in $d(FC-ZFC)/dT$ curves and

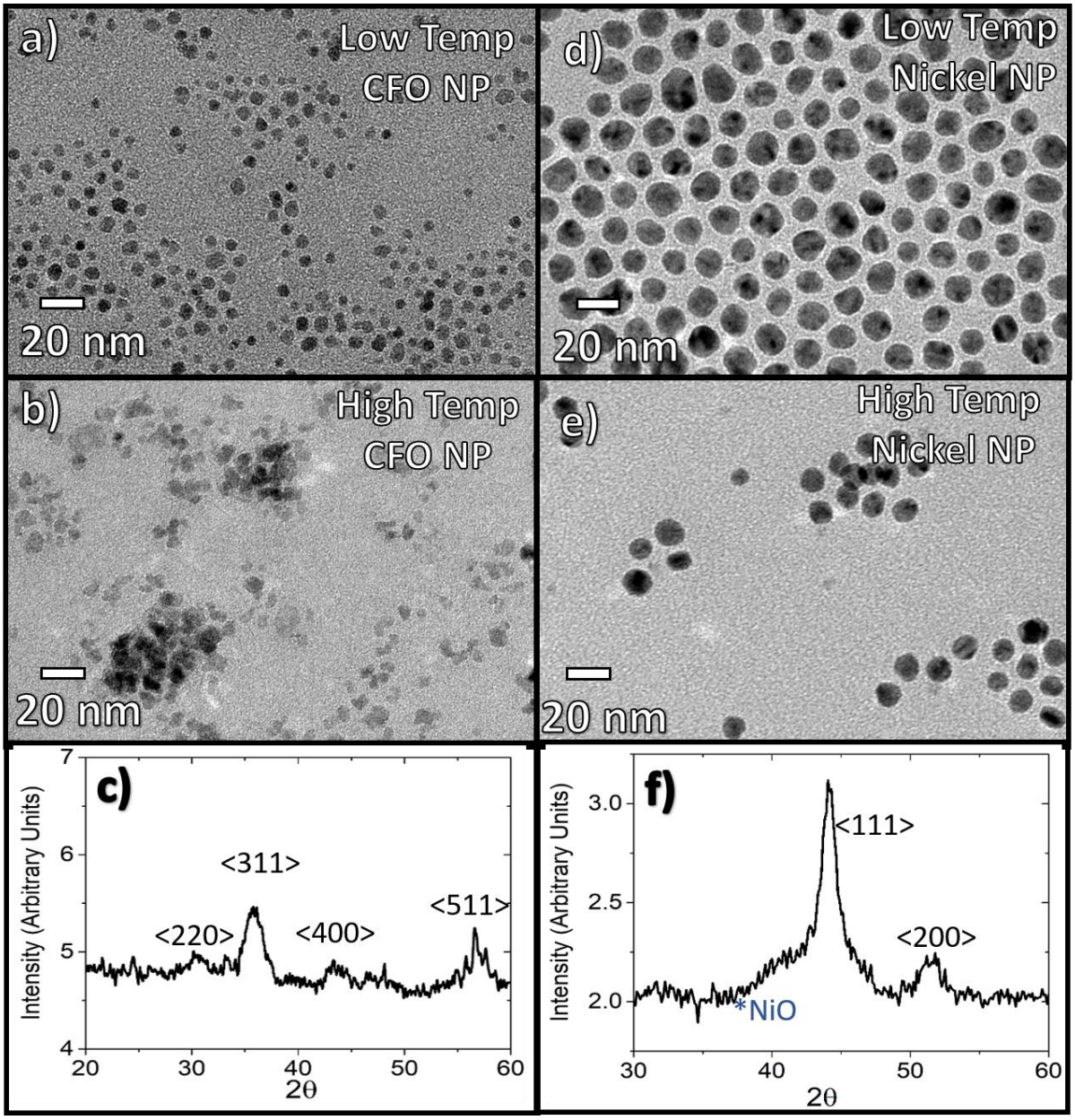

Figure 5.2. a) example TEM image of low temperature cobalt ferrite nanocrystals with low size dispersion and small size. b) high example TEM image of high temperature cobalt ferrite nanocrystals. Crystals remain small while having higher dispersity. C) XRD representative of those for CFO nanoparticle synthesis. d) TEM image of low temperature nickel nanocrystals after exposure to air. E TEM image of high temperature nickel nanocrystals after exposure to

understand what chemical properties can be derived from in depth fitting of the curves. The main

characterizations of the nanoparticle distributions appear in figure 5.2. TEM images were used along with imageJ software to generate nanoparticle size data sets for each distribution. Electron Dispersive Spectroscopy and X-ray diffraction were used to investigate potential structural differences between the nanoparticles.

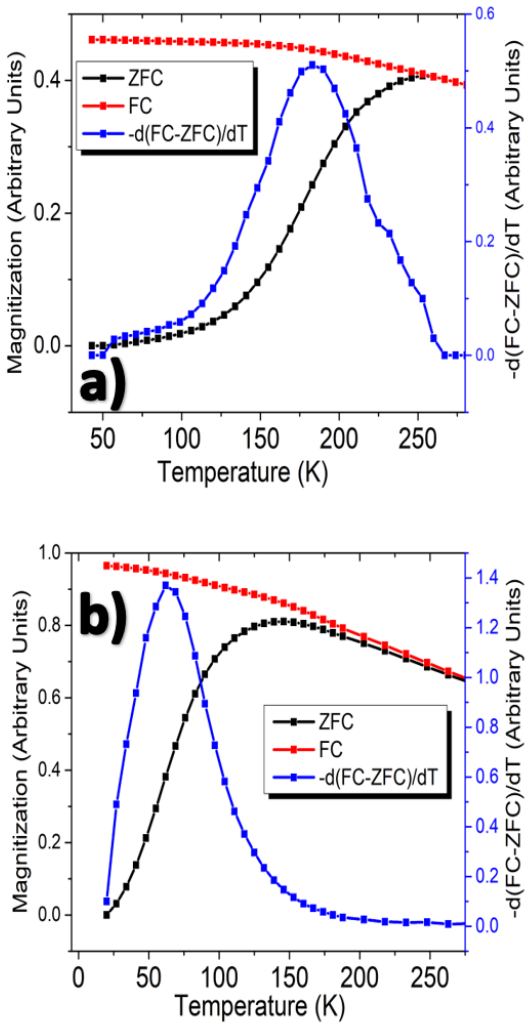

Figure 5.3. a) ZFC(black) FC(red) and -d(FC-ZFC)/d*T* (blue) curve for low temperature CFO nanocrystal distribution. Despite the small size of the crystals the curve is broad and at a high average blocking temperature of 183K. The curve is noticeably not lognormal in shape. b) ZFC(black) FC(red) and -d(FC-ZFC)/d*T* (blue) curve for low temperature Ni nanocrystal distribution. The large nanocrystals have lower anisotropy and so

Each described nanoparticle distribution was measured via SQUID magnetometry to generate zero field cooled and field cooled curves from which -*d*(FC-ZFC)/*dt* curves can be extracted. The curves are full of qualitative information about the differences in nanoparticle distributions. Example curves from low temperature CFO and low temperature nickel can be seen in figure 5.3 as a means of better explaining the curves.

The -*d*(FC-ZFC)/*dT* curve has been described as being analogous with the volumetric distribution in literature. Generally, the average volume of the distribution can be related to the measured blocking temperature using equation 1.

(1) $\boldsymbol{T_b = \frac{K_o V}{25 k_b}}$

The equation works on the assumption that the blocking temperature is a representation of the anisotropy energy of the nanoparticles and that the anisotropy energy is only generated through the

volume of the crystals and the magnetocrystaline anisotropy (MCA) of the material.[22,183,200] With this assumption a number of different qualitative insights can be gathered via -*d*(FC-ZFC)/*dT* curves when comparing extremely different nanoparticle distributions.

Using the CFO and nickel distributions as an example in from figure 5.3, the largest difference in the two distributions in figure 5.3 are that the CFO nanoparticle distribution has a much higher average blocking temperature of 183K vs the Ni nanocrystals which have an average blocking temperature of 62K. High blocking temperature is largely due to the high intrinsic magnetocrystaline anisotropy of CFO.[62,200,201] So, while the nickel nanoparticles are nearly an order of magnitude larger in volume than the CFO, the blocking temperature of the CFO far exceeds that of the nickel nanocrystals. Further the discrepancy in anisotropy constant is largely responsible for the difference in width between the nickel and CFO. While the standard deviation in nanoparticle diameter for nickel is 1.6nm against 1.3nm for CFO, the CFO anisotropy distribution is still much wider. Even slight changes in the nanoparticle size are responsible for largely different blocking temperatures. Finally, it is important to note that the CFO distribution does not have a lognormal shape in the blocking temperature curve as would be expected of the curve being simply representative of size distribution. This is commonly seen in -*d*(FC-ZFC)/d*T* curves at elevated temperatures.[22,202–204] However, for subtly different nanoparticle distributions, a more quantitative understanding of the curves is required.

Quantitatively fitting the curves to find a total anisotropy constant for the nanoparticle set should be possible by applying equation 1 to the known volumetric distribution of nanoparticles. The majority of synthetic nanoparticle methods produce lognormal size distribtuions.[183] Thus, for a given distribution it is trivial to generate a large data set of sizes and fit to a lognormal function and this is frequently done. However, fitting a single anisotropy constant to the entire distribution fails to recover the shape of the -*d*(Fc-ZFC)/*dT* curves, which tend to not be log normal. The failure of this

method to properly fit equations is illustrated in figure 5.4a. A $-d(\mathrm{FC-ZFC})/dT$ curve has been fit using a lognormal function generated from TEM images and equation 1. The data was fit using Origin graphing software. For the blue curve the average anisotropy constant calculated from average volume and average blocking temperature was used to fit the entire curve and for the red curve the anisotropy constant was allowed to optimize the fitting of the curve. In either case, the experimental anisotropy distribution is much narrower than any of the fitting functions, which do not decay before room temperature. The implication of this is that some of the nanoparticles in the distribution should be non- superparamagnetic at room temperature, which is untrue for these distributions.

One trouble that complicates the application of eq 1 to find an anisotropy constant is that the experiment sweeps through a temperature range to find a series of energies, but volumetric magneto crystalline anisotropy constant decays substantially as a function of temperature. As such the attempts to measure the anisotropy across the entire distribution must be adjusted by the

changing. Anisotropy constant decay can be calculated by its relationship to the saturation magnetization (M_s), which is also temperature dependent. Magnetization decay is described by Bloch's law, which appears as eq 2.

$$(2)\quad \frac{M_{s_1}}{M_{s_o}} = (1 - \frac{T_1}{T_o})^p$$

For bulk systems p is 1.5 however due to quantization of magnons within a nano material the decay is often accelerated to up to p of 2 for nanoparticles.[198,205–207] In this work, the decay of magnetization saturation has been fit independently for each of the samples. Values consistently remain between 1.5 and 2 for p as is expected.

The altered Bloch's law for calculating a temperature dependent anisotropy constant appears in eq 3.[198]

$$3)\quad \frac{K_t}{K_o} = ((1 - \frac{T_1}{T_o})^p)^n$$

The value of n in equation 3 is determined by the symmetry of the system in question. As the thermal energy applied to the system increases, the magnetization increases in probability of hopping from an initial magnetic easy axis to an adjacent easy axis. Thus, the constant decays faster in systems with lowest angle between adjacent easy axes. Thus, for a highly symmetric bulk cubic crystal, n is10. However, because the aspect ratio of the nanoparticles

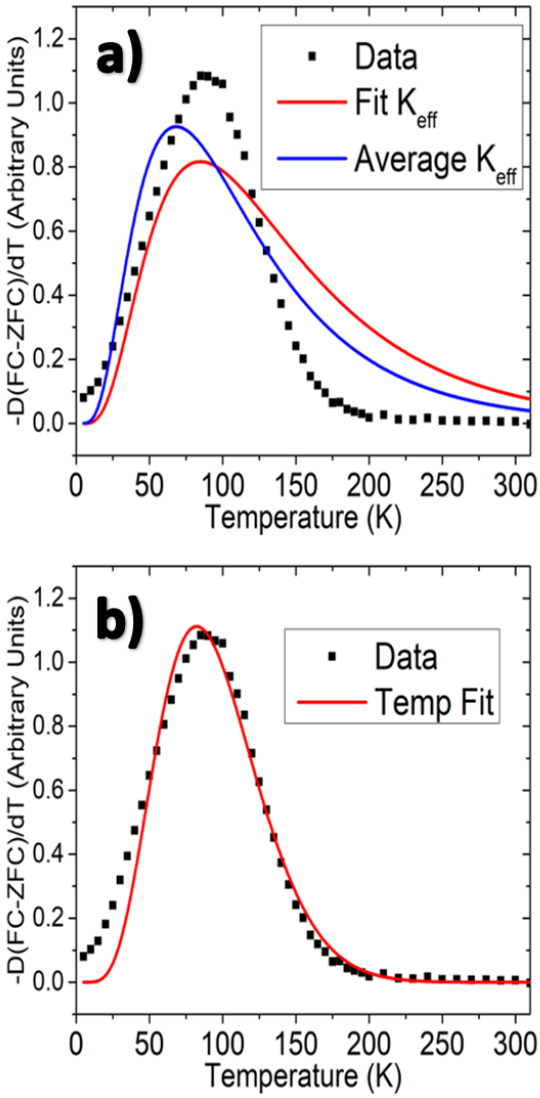

Figure 5.4. a) Fitting -d(FC-ZFC)/*dT* curve data by use of a log normal function where volume is calculated using equation 1. Blue curve uses the calculated average anisotropy constant of the distribution whereas the red curve the anisotropy constant is allowed to change to best fit the data. b) successful fitting of the same data set by use of a combined equation.

tends to be high, the decay of the crystalline anisotropy constant is suppressed and the particles act as though uniaxial in crystalline anisotropy. Therefore, n of three is typically seen for nanoparticles. As such, equation 1 can be rewritten to reflect this shifting anisotropy constant as the temperature relationship to volume as is seen in equation 4.

4) $$V = \frac{T * 25k_b}{K_o((1-\frac{T}{T_o})^p)^n}$$

This is a more accurate calculation of nanoparticle volume from temperature and can be used with the volumetric distribution to fit the *d*(FC-ZFC)/*dT* curve much more accurately.

However, in addition to using an accurate anisotropy constant, the *d*(FC-ZFC)/*dT* is not weighted in the same way as a typical volumetric distribution of nanoparticles would be. Nanoparticle size distributions are a number count lognormal distribution of volumes, but -*d*(FC-ZFC)/*dT* curves are measurements of magnetization of a sample. Thus, the measured signal is weighted by volume of the nanoparticles rather than by the number of nanoparticles switching. Any equation used to fit these curves then must also be weighted with a volume term added to the volumetric lognormal to accurately represent this source of the signal. Additionally, the magnetization of the particles is weighted by the temperature related decay of magnetization as described by equation 2. The full fitting equation then can be seen in equation 5 with the temperature dependent anisotropy constant as well as magnetization signal weighting where all appearances of *V* are substituted with equation 4.

5) $$-d(FC-ZFC)/dT = \left[yo + \frac{A1}{\sqrt{2\pi}\, w*V} e^{\frac{-\left[ln(\frac{V}{Xc})\right]^2}{2w^2}}\right] \times V \times (1-\frac{T}{T_o})^p$$

With the proper corrections applied to the d(FC-ZFC)/dT curves for volume and the two types of decay, these curves can be used to calculate a temperature independent anisotropy constant

and simultaneously analytically fit a volumetric distribution of nanoparticles from a SQUID magnetometry sample. The fits of the magnetometry *d*(FC-ZFC)/*dT* curves appear in figure 5.4b. Qualitatively it is clear that the fitting function is able to encapsulate the shape of the *d*(FC-ZFC)/*dT* curves accurately. More quantitatively, The r^2 for the red and blue curves in figure 5.4a are 0.72 and 0.85 respectively, whereas the temperature dependent fitting has an r^2 of .97. furthermore, the accurate shape fitting allows for a more expected anisotropy constant. Bulk CFO has a magnetocrystaline anisotropy constant ranging between 180 to 300 kJ/m^3, but for nanoparticles the anisotropy constant should be greater due to shape and surface contributions. [87,196,208,209] For the fittings in figure 5.4a the anisotropy constants yielded are 213 kJ/m^3 and 182 kJ/m^3, lower than would be expected for anisotropy constant, whereas the fitting in figure 5.4b is 358 kJ/m^3 which is elevated and therefore more in line with what would be expected for a nanoparticle distribution. [192,196]

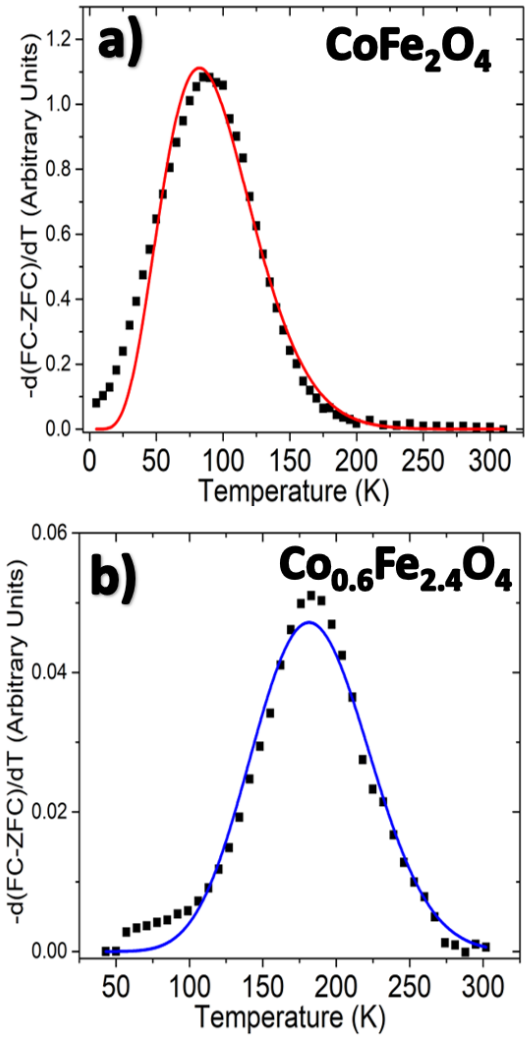

Figure 5.5. a) Fitting -d(FC-ZFC)/*dT* curve of stoichiometrically precise CFO from low temperature synthesis by use of a temperature dependent fitting function. b) Fitting -d(FC-ZFC)/*dT* curve of low cobalt CFO from low temperature synthesis by use of a temperature dependent fitting function.

The high accuracy calculation of anisotropy constant also allows for investigation into material properties, which may otherwise be difficult to prove. The effect of stoichiometry of cobalt ferrite on anisotropy constant in nanoparticles has recently been shown to be large with a local maximum of magnetocrystaline anisotropy at a

stoichiometry of $Co_{.6}Fe_{2.4}O_4$[193] Direct comparisons of blocking temperature can be confounded from volumetric differences when changing synthetic parameters, and further measurements of anisotropy constant are dependent on temperature, meaning higher blocking temperature anisotropy constants are depressed compared to the true figure. Two samples of different stoichiometry cobalt ferrites synthesized in the low temperature synthesis described above in section 2.1 are shown in figure 5.5. A simple calculation of the average anisotropy constant using equation 1 for these two distributions would show the K_{eff} for the blue curve of low cobalt CFO to be 149 kJ/m^3 whereas the stoichiometric CFO as before would have an k_{eff} of 213 kJ/m^3. TEM images of the particles are available in the SI. These calculations are in opposition of what is reported in literature where the MCA of the low cobalt nanoparticles should vastly exceed that of the stoichiometric CFO. However, by fitting the data with the -*d*(FC-ZFC)/*dT* fitting function, the anisotropy constants yielded are 358 kJ/m^3 and 619 kJ/m^3 for the red and blue curves respectively. These anisotropy constants are in much better agreement with literature and it is clear that without accounting for the temperature dependence of the measurement, the wrong values are obtained.

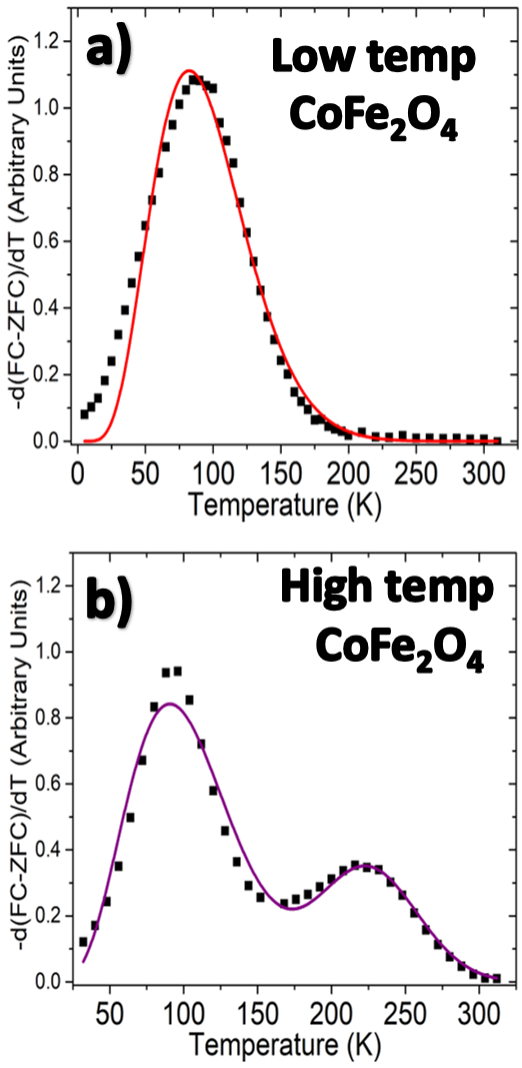

Figure 5.6. a) Fitting -*d*(FC-ZFC)/*dT* curve of stoichiometrically precise CFO from low temperature synthesis by use of a temperature dependent fitting function. b) Fitting -*d*(FC-ZFC)/*dT* curve of stoichiometrically precise CFO from low temperature synthesis by use of a temperature dependent fitting function.

Fitting the full -*d*(FC-ZFC)/*dT* curve becomes even more valuable when approaching an even more complicated system. Higher temperature nanoparticle synthesis can often generate multiple products as a result of the fast reaction speeds and high free energy. Figure 5.6 shows a comparison between two distributions of CFO where one is made at a high temperature and the low temperature CFO that has been shown in figures 5.4 and 5.5. While the volumetric distribution for the high temperature CFO fits best to wo different lognormal distributions, the -*d*(FC-ZFC)/*dT* curve cannot be fit with one anisotropy constant. However, by allowing the distribution to consist of two different temperature dependent expressions two anisotropy constants can be extracted from the magnetization data, 304 kJ/m^3 for the low temperature peak and 756 kJ/m^3 for the higher temperature peak. With such a large discrepancy between the anisotropy constants required to properly describe the data the obvious implication is that multiple species of nanocrystal are being produced in this high temperature synthesis. So, while EDS data shows a stoichiometrically pure mixture within the error of the measurement, the magnetization data presented here betrays the broad variety of nanoparticles that actually exist in the distribution. Thus, temperature dependent fitting of *d*(FC-ZFC)/*dT* curves can generate information about a distribution that is otherwise difficult to detect.

Fitting of CFO is specifically easy due to the high intrinsic magnetocrystaline anisotropy of the material. However, in systems where multiple anisotropies exist at comparable energies, fitting using just the temperature dependent anisotropy constant no longer becomes possible. As an example of this difficulty a distribution of low temperature nickel nanocrystals was synthesized. The volumetric distribution for these nanocrystals was defined as with the CFO nanocrystals and TEM images of these crystals are available in the SI. The results of fitting the *d*(FC-ZFC)/*dT* curve with a temperature dependent anisotropy constant can be seen in in figure 5.7. In the case of nickel, the fitted distribution, in red, is far more narrow than experimental *d*(FC-ZFC)/*dT* curve due to a

number of anisotropies which add artificial broadness to the actual distribution of blocking temperatures. As such it is necessary to incorporate these anisotropies to properly fit the shape of the nickel *d*(FC-ZFC)/*dT* curve. The surface anisotropy is known to be a relevant anisotropy in nanocrystals and is often cited as the reason K_{eff} in nanocrystals vastly exceeds the MCA constant in bulk. [87,198,200,208–210] Including a surface anisotropy term in the fitting distribution requires that the term be calculated through the volumetric distribution. Typically, the surface anisotropy of a system is expected to relate to the total anisotropy following equation six.

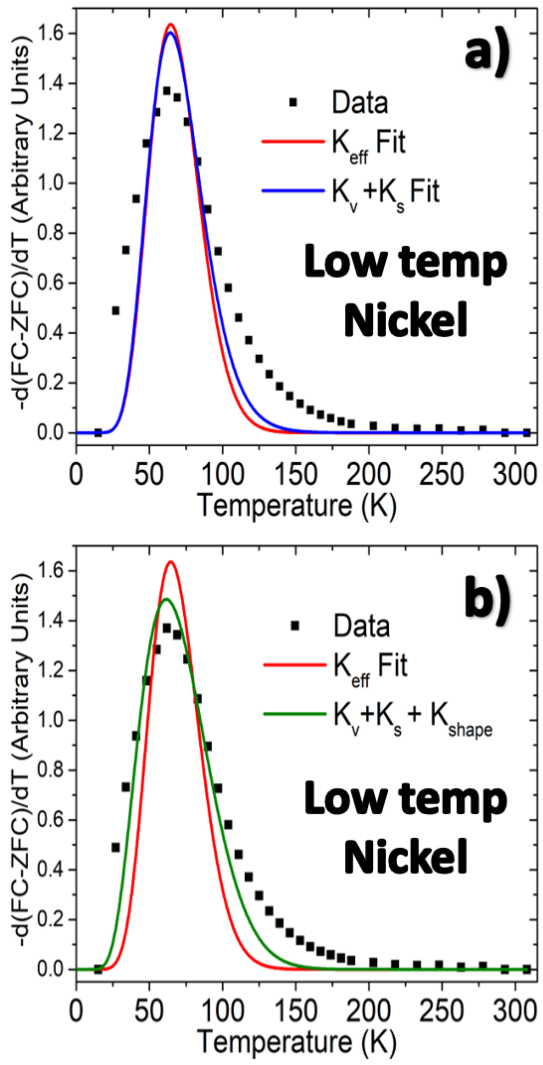

Figure 5.7. a) Fitting -*d*(FC-ZFC)/*dT* curve of nickel nanoparticles from low temperature synthesis by use of a temperature dependent fitting function. (blue) and the same function but with a shape anisotropy term added. b) Fitting -*d*(FC-ZFC)/*dT* curve of the same nickel np data, but with a function including both surface and shape anisotropy with temperature dependent MCA. The fit is greatly improved in the green curve.

6) $$K_{eff} = K_V + \frac{6\,K_S}{d}$$

The relationship clearly stems from the relationship between the volume and the surface ratio of nanoparticles and therefore favors surface anisotropy at smaller total volumes. The equation can be incorporated into the fitting function by expanding the anisotropy term in the volume calculation of equation 4 as is seen in equation 7 which is then plugged into equation 5 as

7) $$V = \frac{T * 25k_b}{K_o((1-\frac{T}{T_o})^p)^n + \frac{6\,K_S}{d}}$$

before.[211] The diameter then at a given temperature can be estimated from an estimate

for volume from equation 5. The additional anisotropy term which does not decay at the same rate as the MCA anisotropy results in the broadening of the blocking temperature distribution.[211] The results of this addition can be seen in the blue curve of figure 5.7a. Clear from this figure is that the shape alone as an addition to the curve is insufficient to justify the distribution of blocking temperatures.

Therefore, shape anisotropy, must be added to the fitting function to better encapsulate the shape of the d(FC-ZFC)$/dT$ curve. Shape anisotropy is particularly relevant in nanoscale regime and has been used as well to justify high K_{eff} seen in nanoparticles and other nanostructures.[22,212,213] To approximate shape anisotropy for the nanoparticles, the aspect ratio of the particles was gathered from the same TEM image data sets analyzed via imageJ. The demagnetizing factor of a given shape can be calculated using equation 8 where m is the aspect ratio of the particle as defined by the largest diameter of the particle divided by the smallest.[214]

8) $$L_x = \frac{4\pi}{m^2-1}\left(\frac{m}{2(m^2-1)^{1/2}}\ln\left(\frac{m+(m^2-1)^{1/2}}{m-(m^2-1)^{1/2}}\right)-1\right)$$

From the demagnetizing factor the shape anisotropy can be calculated via the application of equation 9) which is related to the square of the saturation magnetization and therefore decays at elevated temperature as with Bloch's law.

9) $$K_{shape} = -\frac{(3L_x-4\pi)}{2}m_x^2$$

Thus, the entire equation is identical to equation 5 but in the place of volume fits the entire function as written in equation 10

10) $$V = \frac{T_b * 25k_b}{Ks+K_o((1-\frac{T}{T_o})^p)^n+(\frac{(3L_x-4\pi)}{2}*(MS(1-\frac{T}{T_o})^p)^2)}$$

In order to encapsulate the varying aspect ratio distribution of the nanoparticles the data set was divided into four quartile sets. Thus, four average aspect ratios for the different parts can be separately fit and a composite curve can be linearly combined to fit the total data. To show that all

four quartiles of aspect ratio have the same size distribution, separate histograms were checked for each fitted data set. These histograms appear in figure 5.8

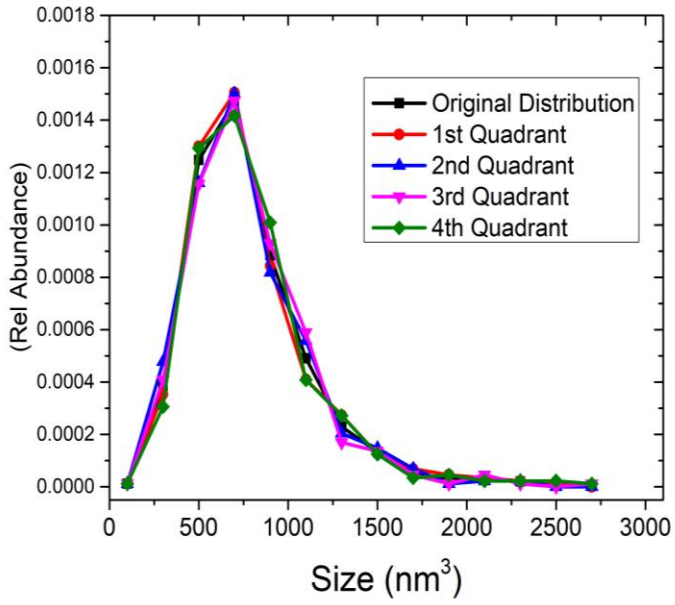

Figure 5.8 Size histogram for Low Temperature Nickel Nanocrystals showing the total distribution of sizes as well as the distribution of sizes for the data set split into four quadrants defined by aspect ratio. 1st quadrant being the 25% lowest aspect ratio particles of the original distribution etc to the highest 25% aspect ratio in quadrant 4. All size distributions appear nearly identical meaning the same volumetric fitting function can be applied ubiquitously

The combined equation is used to fit the function in figure 5.7b in green showing a much-improved agreement with the shape of the d(FC-ZFC)/dT curve. The remainder of the broadness of distribution of blocking temperatures is likely due to interparticle interactions, both dipole and exchange coupling, which also have the effect of elevating and broadening blocking temperature distribution.[215] cite the GMF Furthermore, the added anisotropies fit with physically meaningful numbers. For the red curve the fitted anisotropy constant is 51.8 kJ/m^3, which is much higher than the bulk figure of 23.6 kJ/m^3 whereas for the green curve the volumetric anisotropy contribution is only 22.5 kJ/m^3 with an additional surface anisotropy of 6.1x10^{-7} J/m^2 in near agreement with the literature value of 2.5x10^{-7} J/m^2.[216,217]

To show the utility of the method, another nanoparticle synthetic trial was prepared. For nickel nanocrystals prepared as described in sections 2.3 and 2.4 there is some debate about the prevalence of a nickel phosphide shell surrounding the nanoparticles.[10,21,22] Therefore, to elucidate this possibility nickel nanoparticles were synthesized at high temperature where phosphorous remnant can be confirmed via EDS post washing and then again at a lower temperature where EDS does not detect the presence of phosphorous. The *d*(FC-ZFC)/*dT* curves for both nanoparticle distributions appear in figure 5.9. As mentioned before, the end result of fitting function in figure 5.9a generates a volumetric anisotropy constant of 22.5 kJ/m^3 with a surface constant of 6.1x10^{-7} J/m^2 both in good agreement with literature values for these constants. However, the calculated anisotropy constants for volume and shape for the high temperature nickel are 17.5 kJ/m^3 and 2.0x10^{-10} J/m^2. Indicating that both magnetic anisotropy terms are depressed across the entire dispersion of nickel nanocrystals. This further adds to the conclusion that the phosphorous detected via EDS is not simply remaining attached ligand, but rather attributable to a nickel phosphide outer shell that increases the volume of

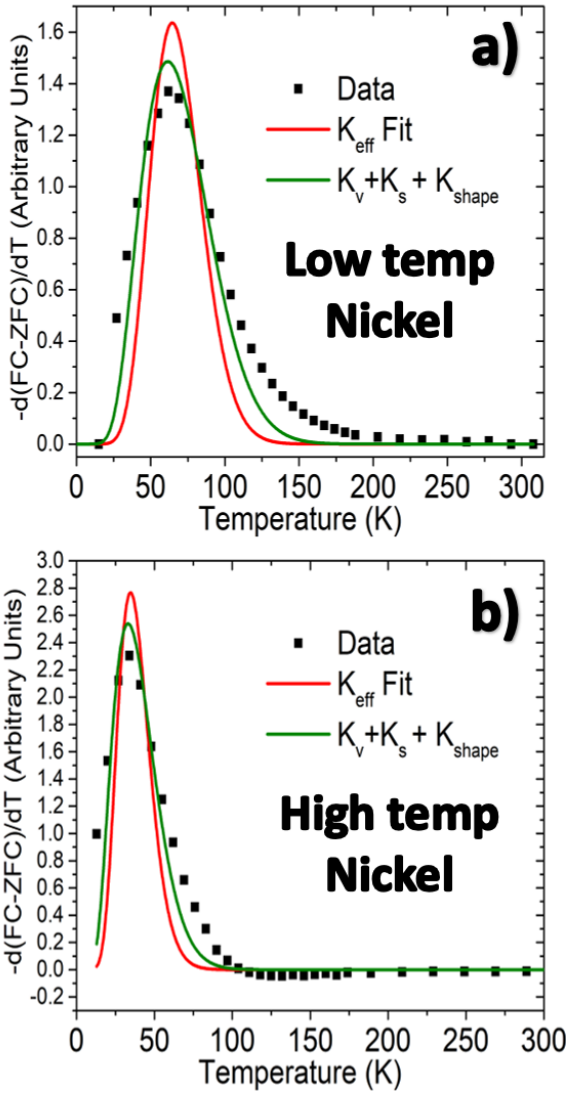

Figure 5.9. a) Fitting -d(FC-ZFC)/*dT* curve of nickel nanoparticles from low temperature synthesis as in figure 5.7b with both temperature dependent and shape/surface additions. b) Fitting -d(FC-ZFC)/*dT* curve of high temperature nickel synthesis, with the same functional forms as

each nanocrystal while acting as a magnetically dead layer that does not contribute to the anisotropy energy. The ability to differentiate between these two possibilities just through fitting of *d*(FC-ZFC)/*dT* curves shows the potency of this fitting methodology.

CONCLUSION: Here a new fitting function for *d*(FC-ZFC)/*dT* curves was proposed unifying the volumetric lognormal distributions of nanoparticles with the blocking temperature distributions. The new method utilized a temperature depended anisotropy constant as well as particle volumetric weighting. It was shown that this method could more successfully generate physically reasonable anisotropy constants for various cobalt ferrite nanoparticle distributions from *d*(FC-ZFC)/*dT* magnetization data sets. Furthermore, it was shown that this functional form could be expanded upon with physically relevant terms to further increase the accuracy of fitting for nanoparticle distributions with smaller inherent magneto crystalline anisotropy. This function was shown to accurately fit *d*(FC-ZFC)/*dT* curves for nickel nanocrystals and was shown to be able to further elucidate the subtlety different chemical structures of nickel nanoparticles synthesized in slightly different syntheses.

The fitting functional form is expected to help explain the large disagreement of anisotropy constants that are listed for nanoparticle distributions. Further it should help generate more physically meaningful anisotropy constants without the need of quoting varied forms of anisotropy for justification. Furthermore, the method is effective in defining the chemical composition of nanoparticles. It is useful in explaining possible reasons for overly broad nanoparticle blocking temperature distributions, which can prevent the application of nanoparticles into useful devices. We expect this functional form to be useful for a wide variety of magnetic nanoparticles both oxides and metallic and to help expand the utility of the *d*(FC-ZFC)/*dT* curves for nanoparticles as a whole.

BIBLIOGRAPHY:

(1) Hou, Y.; Kondoh, H.; Ohta, T. Size-Controlled Synthesis and Magnetic Studies of Monodisperse FePd Nanoparticles. *Journal of Nanoscience and Nanotechnology* **2009**, *9* (1), 202–208. https://doi.org/10.1166/JNN.2009.J056.

(2) Park, J.; Lee, E.; Hwang, N.-M.; Kang, M.; Kim, S. C.; Hwang, Y.; Park, J.-G.; Noh, H.-J.; Kim, J.-Y.; Park, J.-H.; Hyeon, T.; Park,] J; Lee, E.; Kim, S. C.; Hyeon, T.; Hwang, N.-M.; Kang, M.; Hwang, Y.; Park, J.-G.; Noh, H.-J.; Kim, J.-Y.; Park, J.-H. One-Nanometer-Scale Size-Controlled Synthesis of Monodisperse Magnetic Iron Oxide Nanoparticles. *Angewandte Chemie International Edition* **2005**, *44* (19), 2872–2877. https://doi.org/10.1002/ANIE.200461665.

(3) Friedrich, R. M.; Zabel, S.; Galka, A.; Lukat, N.; Wagner, J. M.; Kirchhof, C.; Quandt, E.; McCord, J.; Selhuber-Unkel, C.; Siniatchkin, M.; Faupel, F. Magnetic Particle Mapping Using Magnetoelectric Sensors as an Imaging Modality. *Scientific Reports 2019 9:1* **2019**, *9* (1), 1–11. https://doi.org/10.1038/s41598-018-38451-0.

(4) Gonçalves, R.; Larrea, A.; Sebastian, M. S.; Sebastian, V.; Martins, P.; Lanceros-Mendez, S. Synthesis and Size Dependent Magnetostrictive Response of Ferrite Nanoparticles and Their Application in Magnetoelectric Polymer-Based Multiferroic Sensors. *Journal of Materials Chemistry C* **2016**, *4* (45), 10701–10706. https://doi.org/10.1039/C6TC04188D.

(5) Couvreur, P. Nanoparticles in Drug Delivery: Past, Present and Future. *Advanced Drug Delivery Reviews* **2013**, *65* (1), 21–23. https://doi.org/10.1016/J.ADDR.2012.04.010.

(6) Hristoforou, E.; Ktena, A. Magnetostriction and Magnetostrictive Materials for Sensing Applications. *Journal of Magnetism and Magnetic Materials* **2007**, *316* (2 SPEC. ISS.), 372–378. https://doi.org/10.1016/J.JMMM.2007.03.025.

(7) Revia, R. A.; Zhang, M. Magnetite Nanoparticles for Cancer Diagnosis, Treatment, and Treatment Monitoring: Recent Advances. *Mater. Today* **2016**, *19* (3), 157–168. https://doi.org/10.1016/j.mattod.2015.08.022.

(8) Spaldin, N. A. *Magnetic Materials*; Cambridge University Press: Cambridge, 2010. https://doi.org/10.1017/CBO9780511781599.

(9) Spaldin, N. A.; Ramesh, R. Advances in Magnetoelectric Multiferroics. https://doi.org/10.1038/s41563-018-0275-2.

(10) Sasaki, S.; Kurish, J.; Robbennolt, S.; Yan, Y.; Garcia, E.; Tolbert, S. H. Covalent Bonding-Based Adhesion Method for Rigidly Coupling Metal Nanocrystals to Metal and Metal Oxide Surfaces. *ACS Applied Nano Materials* **2021**, *4* (4), 3426–3433. https://doi.org/10.1021/ACSANM.0C03246/SUPPL_FILE/AN0C03246_SI_001.PDF.

(11) Ghunaim, R.; Eckert, V.; Scholz, M.; Gellesch, M.; Wurmehl, S.; Damm, C.; Büchner, B.; Mertig, M.; Hampel, S. Carbon Nanotube-Assisted Synthesis of Ferromagnetic Heusler Nanoparticles of Fe 3 Ga (Nano-Galfenol). *Journal of Materials Chemistry C* **2018**, *6* (5), 1255–1263. https://doi.org/10.1039/C7TC04618A.

(12) Mourdikoudis, S.; Liz-Marzán, L. M. Oleylamine in Nanoparticle Synthesis. *Chemistry of Materials* **2013**, *25* (9), 1465–1476. https://doi.org/10.1021/CM4000476.

(13) Boles, M. A.; Ling, D.; Hyeon, T.; Talapin, D. v. The Surface Science of Nanocrystals. *Nature Materials 2016 15:2* **2016**, *15* (2), 141–153. https://doi.org/10.1038/nmat4526.

(14) Carenco, S.; Labouille, S.; Bouchonnet, S.; Boissière, C.; le Goff, X. F.; Sanchez, C.; Mézailles, N. Revisiting the Molecular Roots of a Ubiquitously Successful Synthesis: Nickel(0) Nanoparticles by Reduction of [Ni(Acetylacetonate)2]. *Chemistry – A European Journal* **2012**, *18* (44), 14165–14173. https://doi.org/10.1002/CHEM.201201071.

(15) Rosen, E. L.; Buonsanti, R.; Llordes, A.; Sawvel, A. M.; Milliron, D. J.; Helms, B. A. Exceptionally Mild Reactive Stripping of Native Ligands from Nanocrystal Surfaces by Using Meerwein's Salt. *Angewandte Chemie - International Edition* **2012**, *51* (3), 684–689. https://doi.org/10.1002/ANIE.201105996.

(16) Bhar, M.; Rudra, S.; Mukherjee, P. What Role Can Surface Capping Ligand Play to Control Dopant Emission in Semiconductor Nanoparticles? *Journal of Physical Chemistry C* **2020**, *124* (12), 6588–6597. https://doi.org/10.1021/ACS.JPCC.9B11074/SUPPL_FILE/JP9B11074_SI_001.PDF.

(17) Electric-Field Control of Magnetism via Strain Transfer across Ferromagnetic/Ferroelectric Interfaces. **2015**. https://doi.org/10.1088/0953-8984/27/50/504001.

(18) Volkman, S. K.; Yin, S.; Bakhishev, T.; Puntambekar, K.; Subramanian, V.; Toney, M. F. Mechanistic Studies on Sintering of Silver Nanoparticles. *Chem. Mater* **2011**, *23*, 4634–4640. https://doi.org/10.1021/cm202561u.

(19) Nadeem, K.; Ullah, A.; Mushtaq, M.; Kamran, M.; Hussain, S. S.; Mumtaz, M. Effect of Air Annealing on Structural and Magnetic Properties of Ni/NiO Nanoparticles. *Journal of Magnetism and Magnetic Materials* **2016**, *417*, 6–10. https://doi.org/10.1016/J.JMMM.2016.05.064.

(20) Kim, J.; Rong, C.; Ping Liu, J.; Sun, S. Dispersible Ferromagnetic FePt Nanoparticles. *Advanced Materials* **2009**, *21* (8), 906–909. https://doi.org/10.1002/ADMA.200801620.

(21) Carenco, S.; edric Boissi ere, C.; Nicole, L.; ement Sanchez, C.; le Floch, P.; ezailles, N. M. Controlled Design of Size-Tunable Monodisperse Nickel Nanoparticles. *Chem. Mater* **2010**, *22*, 1340–1349. https://doi.org/10.1021/cm902007g.

(22) Batley, J. T.; Nguyen, M.; Kamboj, I.; Korostynski, C.; Aydil, E. S.; Leighton, C. Quantitative Understanding of Superparamagnetic Blocking in Thoroughly Characterized Ni Nanoparticle Assemblies. *Cite This: Chem. Mater* **2020**, *32*, 6506. https://doi.org/10.1021/acs.chemmater.0c01758.

(23) Udalov, O.; Chtchelkatchev, N.; Belobordov, I.; Chtchelkatchev, N. M.; Beloborodov, I. S. Electric Field Control of Magnetic Properties and Magneto-Transport in Composite Multiferroics. *Journal of Physics: Condensed Matter J. Phys.: Condens. Matter* **2015**, *27*, 10. https://doi.org/10.1088/0953-8984/27/18/186001.

(24) Sasaki, S.; Udalov, O.; Kurish, J.; Ishii, M.; Beloborodov, I.; Tolbert, S. Tuning Exchange Coupling in a New Family of Nanocrystal-Based Granular Multiferroics Using an Applied Electric Field (Approved). *ACS Applied Materials & Interfaces* **2022**.

(25) Kudr, J.; Haddad, Y.; Richtera, L.; Heger, Z.; Cernak, M.; Adam, V.; Zitka, O. Magnetic Nanoparticles: From Design and Synthesis to Real World Applications. *Nanomaterials* **2017**, *7* (9). https://doi.org/10.3390/NANO7090243.

(26) Yew, Y. P.; Shameli, K.; Miyake, M.; Ahmad Khairudin, N. B. B.; Mohamad, S. E. B.; Naiki, T.; Lee, K. X. Green Biosynthesis of Superparamagnetic Magnetite Fe3O4 Nanoparticles and Biomedical Applications in Targeted Anticancer Drug Delivery System: A Review. *Arabian Journal of Chemistry* **2020**, *13* (1), 2287–2308. https://doi.org/10.1016/J.ARABJC.2018.04.013.

(27) Lodeiro, C.; Roig, A.; Saccardo, P.; Bronstein, L. M.; Price, P. M.; Mahmoud, W. E.; Al-Ghamdi, A. A. Magnetic Drug Delivery: Where the Field Is Going. *Frontiers in Chemistry | www.frontiersin.org* **2018**, *6*, 619. https://doi.org/10.3389/fchem.2018.00619.

(28) Reddy, L. H.; Arias, J. L.; Nicolas, J.; Couvreur, P. Magnetic Nanoparticles: Design and Characterization, Toxicity and Biocompatibility, Pharmaceutical and Biomedical Applications. *Chem. Rev.* **2012**, *112* (11), 5818–5878. https://doi.org/10.1021/cr300068p.

(29) Harada, M.; Kuwa, M.; Sato, R.; Teranishi, T.; Takahashi, M.; Maenosono, S. Cation Distribution in Monodispersed MFe 2 O 4 (M = Mn, Fe, Co, Ni, and Zn) Nanoparticles Investigated by X-Ray Absorption Fine Structure Spectroscopy: Implications for Magnetic Data Storage, Catalysts, Sensors, and Ferrofluids. *Cite This: ACS Appl. Nano Mater* **2020**, *2020*, 8389–8402. https://doi.org/10.1021/acsanm.0c01810.

(30) Carlos Camacho-Fernández, J.; Karendash González-Quijano, G.; Séverac, C.; -, al; Tu, S.-J.; Wu, S.-Y.; Wang, F.-S.; Kashanian, F.; Habibi-Rezaei, M.; Moosavi-Movahedi, A. A.; Wu, K.; Su, D.; Liu, J.; Saha, R.; Wang, J.-P. Magnetic Nanoparticles in Nanomedicine: A Review of Recent Advances. *Nanotechnology* **2019**, *30* (50), 502003. https://doi.org/10.1088/1361-6528/AB4241.

(31) Kim, S.; Kim, N.; Seo, J.; Park, J. E.; Song, E. H.; Choi, S. Y.; Kim, J. E.; Cha, S.; Park, H. H.; Nam, J. M. Nanoparticle-Based Computing Architecture for Nanoparticle Neural Networks. *Science Advances* **2020**, *6* (35). https://doi.org/10.1126/SCIADV.ABB3348.

(32) Hedayatnasab, Z.; Abnisa, F.; Daud, W. M. A. W. Review on Magnetic Nanoparticles for Magnetic Nanofluid Hyperthermia Application. *Materials & Design* **2017**, *123*, 174–196. https://doi.org/10.1016/J.MATDES.2017.03.036.

(33) Wu, L.; Mendoza-Garcia, A.; Li, Q.; Sun, S. Organic Phase Syntheses of Magnetic Nanoparticles and Their Applications. *Chemical Reviews* **2016**, *116* (18), 10473–10512. https://doi.org/10.1021/ACS.CHEMREV.5B00687.

(34) Kim, S.; Kim, N.; Seo, J.; Park, J. E.; Song, E. H.; Choi, S. Y.; Kim, J. E.; Cha, S.; Park, H. H.; Nam, J. M. Nanoparticle-Based Computing Architecture for Nanoparticle Neural Networks. *Science Advances* **2020**, *6* (35). https://doi.org/10.1126/SCIADV.ABB3348/SUPPL_FILE/ABB3348_SM.PDF.

(35) Al-Bustami, H.; Koplovitz, G.; Primc, D.; Yochelis, S.; Capua, E.; Porath, D.; Naaman, R.; Paltiel, Y.; Al-Bustami, H.; Koplovitz, G.; Yochelis, S.; Paltiel, Y.; Primc, D.; Capua, E.; Naaman, R.; Porath, D. Single Nanoparticle Magnetic Spin Memristor. *Small* **2018**, *14* (30), 1801249. https://doi.org/10.1002/SMLL.201801249.

(36) Noh, B. il; Yang, S. C. Ferromagnetic, Ferroelectric, and Magnetoelectric Properties in Individual Nanotube-Based Magnetoelectric Films of CoFe2O4/BaTiO3 Using Electrically Resistive Core-Shell Magnetostrictive Nanoparticles. *Journal of Alloys and Compounds* **2022**, *891*, 161861. https://doi.org/10.1016/J.JALLCOM.2021.161861.

(37) Narita, F.; Fox, M. A Review on Piezoelectric, Magnetostrictive, and Magnetoelectric Materials and Device Technologies for Energy Harvesting Applications. **2017**. https://doi.org/10.1002/adem.201700743.

(38) Mushtaq, F.; Chen, X.; Torlakcik, H.; Steuer, C.; Hoop, M.; Siringil, E. C.; Marti, X.; Limburg, G.; Stipp, P.; Nelson, B. J.; Pané, S. Magnetoelectrically Driven Catalytic Degradation of Organics. *Advanced Materials* **2019**, *31* (28). https://doi.org/10.1002/ADMA.201901378.

(39) Mamiya, H.; Fukumoto, H.; Cuya Huaman, J. L.; Suzuki, K.; Miyamura, H.; Balachandran, J. Estimation of Magnetic Anisotropy of Individual Magnetite Nanoparticles for Magnetic Hyperthermia. *ACS Nano* **2020**, *14* (7), 8421–8432. https://doi.org/10.1021/ACSNANO.0C02521/SUPPL_FILE/NN0C02521_SI_001.PDF.

(40) Mahmoudi, K.; Bouras, A.; Bozec, D.; Ivkov, R.; Hadjipanayis, C. Magnetic Hyperthermia Therapy for the Treatment of Glioblastoma: A Review of the Therapy's History, Efficacy and Application in Humans. *https://doi.org/10.1080/02656736.2018.1430867* **2018**, *34* (8), 1316–1328. https://doi.org/10.1080/02656736.2018.1430867.

(41) Chakka, V. M.; Altuncevahir, B.; Jin, Z. Q. Magnetic Nanoparticles Produced by Surfactant-Assisted Ball Milling. *J. Appl. Phys* **2006**, *99*, 8–912. https://doi.org/10.1063/1.2170593.

(42) Kurichenko, V. L.; Karpenkov, Y.; Gabay, A. M.; Akdogan, N. G.; Marinescu, M.; Liu, J. F.; Hadjipanayis, G. C. Rare Earth-Cobalt Hard Magnetic Nanoparticles and Nanoflakes by High-Energy Milling. *J. Phys.: Condens. Matter* **2010**, *22*, 6. https://doi.org/10.1088/0953-8984/22/16/164213.

(43) de Carvalho, J. F.; de Medeiros, S. N.; Morales, M. A.; Dantas, A. L.; Carriço, A. S. Synthesis of Magnetite Nanoparticles by High Energy Ball Milling. *Applied Surface Science* **2013**, *275*, 84–87. https://doi.org/10.1016/J.APSUSC.2013.01.118.

(44) Lu, A.-H.; Salabas, E. L.; Schüth, F. Magnetic Nanoparticles Magnetic Nanoparticles: Synthesis, Protection, Functionalization, and Application. *Angew. Chem. Int. Ed* **2007**, *46*, 1222–1244. https://doi.org/10.1002/anie.200602866.

(45) Lin, X. M.; Samia, A. C. S. Synthesis, Assembly and Physical Properties of Magnetic Nanoparticles. *Journal of Magnetism and Magnetic Materials* **2006**, *305* (1), 100–109. https://doi.org/10.1016/J.JMMM.2005.11.042.

(46) Bedanta, S.; Barman, A.; Kleemann, W.; Petracic, O.; Seki, T. Magnetic Nanoparticles: A Subject for Both Fundamental Research and Applications. *Journal of Nanomaterials* **2013**, *2013*. https://doi.org/10.1155/2013/952540.

(47) Kim, J.; Kim, J.; Kim, J.; Hyeon Kim, K. Characterization of As-Synthesized FeCo Magnetic Nanoparticles by Coprecipitation Method. *Journal of Applied Physics* **2013**, *113* (17), 17A313. https://doi.org/10.1063/1.4795321.

(48) Simeonidis, K.; Sarafidis, C.; Papastergiadis, E.; Angelakeris, M.; Tsiaoussis, I.; Kalogirou, O. Evolution of Nd2Fe14B Nanoparticles Magnetism during Surfactant-Assisted Ball-Milling. *Intermetallics* **2011**, *19* (4), 589–595. https://doi.org/10.1016/J.INTERMET.2010.12.012.

(49) Hadef, F. Synthesis and Disordering of B2 TM-Al (TM = Fe, Ni, Co) Intermetallic Alloys by High Energy Ball Milling: A Review. *Powder Technology* **2017**, *311*, 556–578. https://doi.org/10.1016/J.POWTEC.2017.01.082.

(50) Saravanan, P.; Deepika, D.; Hsu, J.-H.; Vinod, V. T. P.; Miroslavˇ, M.; Miroslavčerník, M.; Kamat, S. v. A Surfactant-Assisted High Energy Ball Milling Technique to Produce Colloidal Nanoparticles and Nanocrystalline Flakes in Mn-Al Alloys. **2015**. https://doi.org/10.1039/c5ra16550d.

(51) Soon, G. K.; Piao, Y.; Park, J.; Angappane, S.; Jo, Y.; Hwang, N. M.; Park, J. G.; Hyeon, T. Kinetics of Monodisperse Iron Oxide Nanocrystal Formation by "Heating-up" Process. *Journal of the American Chemical Society* **2007**, *129* (41), 12571–12584. https://doi.org/10.1021/JA074633Q/SUPPL_FILE/JA074633QSI20070731_114736.PDF.

(52) Willard, M. A.; Kurihara, L. K.; Carpenter, E. E.; Calvin, S.; Harris, V. G. Chemically Prepared Magnetic Nanoparticles. **2013**. https://doi.org/10.1179/095066004225021882.

(53) Stanicki, D.; Elst, L. vander; Muller, R. N.; Laurent, S. Synthesis and Processing of Magnetic Nanoparticles. *Current Opinion in Chemical Engineering* **2015**, *C* (8), 7–14. https://doi.org/10.1016/J.COCHE.2015.01.003.

(54) Moumen, N.; Pileni, M. P. Control of the Size of Cobalt Ferrite Magnetic Fluid. *Journal of Physical Chemistry* **1996**, *100* (5), 1867–1873. https://doi.org/10.1021/JP9524136.

(55) Nlebedim, I. C.; Snyder, J. E.; Moses, A. J.; Jiles, D. C. Anisotropy and Magnetostriction in Non-Stoichiometric Cobalt Ferrite. *IEEE Transactions on Magnetics* **2012**, *48* (11), 3084–3087. https://doi.org/10.1109/TMAG.2012.2200884.

(56) Sharifi Dehsari, H.; Asadi, K. Impact of Stoichiometry and Size on the Magnetic Properties of Cobalt Ferrite Nanoparticles. *Journal of Physical Chemistry C* **2018**, *122* (51), 29106–29121. https://doi.org/10.1021/ACS.JPCC.8B09276/SUPPL_FILE/JP8B09276_SI_001.PDF.

(57) Tomar, D.; Jeevanandam, P. Synthesis of Cobalt Ferrite Nanoparticles with Different Morphologies via Thermal Decomposition Approach and Studies on Their Magnetic Properties. *Journal of Alloys and Compounds* **2020**, *843*, 155815. https://doi.org/10.1016/J.JALLCOM.2020.155815.
(58) Goodarz Naseri, M.; Saion, E. B.; Abbastabar Ahangar, H.; Shaari, A. H.; Hashim, M. Simple Synthesis and Characterization of Cobalt Ferrite Nanoparticles by a Thermal Treatment Method. *Journal of Nanomaterials* **2010**, *2010*. https://doi.org/10.1155/2010/907686.
(59) Salunkhe, A. B.; Khot, V. M.; Phadatare, M. R.; Pawar, S. H. Combustion Synthesis of Cobalt Ferrite Nanoparticles—Influence of Fuel to Oxidizer Ratio. *Journal of Alloys and Compounds* **2012**, *514*, 91–96. https://doi.org/10.1016/J.JALLCOM.2011.10.094.
(60) Li, W.; Liu, Y.; Guo, Y. Hollow CoFe 2 O 4 Nanospheres as a High Capacity Anode Material for Lithium Ion Batteries The Synthesis of Magnetically Exchange Coupled CoFe 2 O 4 /CoFe 2 Composites through Low Temperature CaH 2 Reduction. https://doi.org/10.1088/0957-4484/23/5/055402.
(61) Melo, R. S.; Banerjee, P.; Franco, A. Hydrothermal Synthesis of Nickel Doped Cobalt Ferrite Nanoparticles: Optical and Magnetic Properties. *Journal of Materials Science: Materials in Electronics* **2018**, *29* (17), 14657–14667. https://doi.org/10.1007/S10854-018-9602-2.
(62) Ansari, S. M.; Sinha, B. B.; Phase, D.; Sen, D.; Sastry, P. U.; Kolekar, Y. D.; Ramana, C. v. Particle Size, Morphology, and Chemical Composition Controlled CoFe2O4 Nanoparticles with Tunable Magnetic Properties via Oleic Acid Based Solvothermal Synthesis for Application in Electronic Devices. *ACS Applied Nano Materials* **2019**, *2* (4), 1828–1843. https://doi.org/10.1021/ACSANM.8B02009/SUPPL_FILE/AN8B02009_SI_001.PDF.
(63) Lu, L. T.; Dung, N. T.; Tung, L. D.; Thanh, C. T.; Quy, O. K.; Chuc, N. v; Maenosono, S.; Thanh, N. T. K. Synthesis of Magnetic Cobalt Ferrite Nanoparticles with Controlled Morphology, Monodispersity and Composition: The Influence of Solvent, Surfactant, Reductant and Synthetic Conditions. *Nanoscale* **2015**, *7*, 19596. https://doi.org/10.1039/c5nr04266f.
(64) Lamer, V. K.; Dinegar, R. H. Theory, Production and Mechanism of Formation of Monodispersed Hydrosols. *Journal of the American Chemical Society* **2002**, *72* (11), 4847–4854. https://doi.org/10.1021/JA01167A001.
(65) Whitehead, C. B.; Özkar, S.; Finke, R. G. LaMer's 1950 Model for Particle Formation of Instantaneous Nucleation and Diffusion-Controlled Growth: A Historical Look at the Model's Origins, Assumptions, Equations, and Underlying Sulfur Sol Formation Kinetics Data. *Chemistry of Materials* **2019**, *31* (18), 7116–7132. https://doi.org/10.1021/ACS.CHEMMATER.9B01273/SUPPL_FILE/CM9B01273_SI_001.PDF.
(66) Whitehead, C. B.; Özkar, S.; Finke, R. G. LaMer's 1950 Model of Particle Formation: A Review and Critical Analysis of Its Classical Nucleation and Fluctuation Theory Basis, of Competing Models and Mechanisms for Phase-Changes and Particle Formation, and Then of Its Application to Silver Halide, Semiconductor, Metal, and Metal-Oxide Nanoparticles. *Materials Advances* **2021**, *2* (1), 186–235. https://doi.org/10.1039/D0MA00439A.
(67) McDonagh, B. H.; Staudinger, C.; Normile, P. S.; de Toro, J. A.; Bandyopadhyay, S.; Glomm, W. R.; Singh, G. New Insights into Controlling the Twin Structure of Magnetic Iron Oxide Nanoparticles. *Applied Materials Today* **2021**, *24*, 101084. https://doi.org/10.1016/J.APMT.2021.101084.

(68) Sharma, R.; Thakur, P.; Sharma, P.; Sharma, V. Ferrimagnetic Ni2+ Doped Mg-Zn Spinel Ferrite Nanoparticles for High Density Information Storage. *Journal of Alloys and Compounds* **2017**, *704*, 7–17. https://doi.org/10.1016/J.JALLCOM.2017.02.021.

(69) Vreeland, E. C.; Watt, J.; Schober, G. B.; Hance, B. G.; Austin, M. J.; Price, A. D.; Fellows, B. D.; Monson, T. C.; Hudak, N. S.; Maldonado-Camargo, L.; Bohorquez, A. C.; Rinaldi, C.; Huber, D. L. Enhanced Nanoparticle Size Control by Extending LaMer's Mechanism. *Chemistry of Materials* **2015**, *27* (17), 6059–6066. https://doi.org/10.1021/ACS.CHEMMATER.5B02510/SUPPL_FILE/CM5B02510_SI_001.PDF.

(70) Fellows, B. D.; Sandler, S.; Livingston, J.; Fuller, K.; Nwandu, L.; Timmins, S.; Lantz, K. A.; Stefik, M.; Thompson Mefford, O. Extended LaMer Synthesis of Cobalt-Doped Ferrite. *IEEE Magnetics Letters* **2017**, *9*. https://doi.org/10.1109/LMAG.2017.2787683.

(71) st. John, S.; Nan, Z.; Hu, N.; Schaefer, D. W.; Angelopoulos, A. P. A Nanoscale-Modified LaMer Model for Particle Synthesis from Inorganic Tin–Platinum Complexes. *Journal of Materials Chemistry A* **2013**, *1* (31), 8903–8916. https://doi.org/10.1039/C3TA11552F.

(72) Hennous, M.; Venkata Ramana, E.; Tobaldi, D. M.; Costa, B. F. O.; Valente, M. A.; Labrincha, J.; Karmaoui, M. Synthesis, Structure and Magnetic Properties of Multipod-Shaped Cobalt Ferrite Nanocrystals †. *New J. Chem* **2019**, *43*, 10259. https://doi.org/10.1039/c9nj02237f.

(73) Sharma, P.; Holliger, N.; Pfromm, P. H.; Liu, B.; Chikan, V. Size-Controlled Synthesis of Iron and Iron Oxide Nanoparticles by the Rapid Inductive Heating Method. *ACS Omega* **2020**, *5* (31), 19853–19860. https://doi.org/10.1021/ACSOMEGA.0C02793/SUPPL_FILE/AO0C02793_SI_001.PDF.

(74) van Embden, J.; Sader, J. E.; Davidson, M.; Mulvaney, P. Evolution of Colloidal Nanocrystals: Theory and Modeling of Their Nucleation and Growth. https://doi.org/10.1021/jp9027673.

(75) Mantzaris, N. v. Liquid-Phase Synthesis of Nanoparticles: Particle Size Distribution Dynamics and Control. *Chemical Engineering Science* **2005**, *60* (17), 4749–4770. https://doi.org/10.1016/J.CES.2005.04.012.

(76) Arshadi, S.; Moghaddam, J.; Eskandarian, M. LaMer Diagram Approach to Study the Nucleation and Growth of Cu 2 O Nanoparticles Using Supersaturation Theory. *Korean J. Chem. Eng* **2014**, *31* (11), 2020–2026. https://doi.org/10.1007/s11814-014-0130-3.

(77) Prins, P. T.; Montanarella, F.; Dü, K.; Justo, Y.; van der Bok, J. C.; Hinterding, S. O. M.; Geuchies, J. J.; Maes, J.; de Nolf, K.; Deelen, S.; Meijer, H.; Zinn, T.; Petukhov, A. v; Rabouw, F. T.; De, C.; Donega, M.; Vanmaekelbergh, D.; Hens, Z. Extended Nucleation and Superfocusing in Colloidal Semiconductor Nanocrystal Synthesis. **2021**, *29*, 31. https://doi.org/10.1021/acs.nanolett.0c04813.

(78) Leffler, V.; Ehlert, S.; Fö, B.; Dulle, M.; Fö, S. Nanoparticle Heat-Up Synthesis: In Situ X-Ray Diffraction and Extension from Classical to Nonclassical Nucleation and Growth Theory. **2021**. https://doi.org/10.1021/acsnano.0c07359.

(79) Hütten, A.; Sudfeld, D.; Ennen, I.; Reiss, G.; Wojczykowski, K.; Jutzi, P. Ferromagnetic FeCo Nanoparticles for Biotechnology. *Journal of Magnetism and Magnetic Materials* **2005**, *293* (1), 93–101. https://doi.org/10.1016/J.JMMM.2005.01.048.

(80) Barcaro, G.; Monti, S. Modeling Generation and Growth of Iron Oxide Nanoparticles from Representative Precursors through ReaxFF Molecular Dynamics †. **2020**, *12*, 3103. https://doi.org/10.1039/c9nr09381h.

(81) Chang, H.; Hyo Kim, B.; Young Jeong, H.; Hee Moon, J.; Park, M.; Shin, K.; In Chae, S.; Lee, J.; Kang, T.; Kyu Choi, B.; Yang, J.; Bootharaju, M. S.; Song, H.; Hee An, S.; Man Park, K.; Yeon Oh, J.; Lee, H.; Soo Kim, M.; Park, J.; Hyeon, T. Molecular-Level Understanding of Continuous Growth from Iron-Oxo Clusters to Iron Oxide Nanoparticles. **2019**. https://doi.org/10.1021/jacs.9b01670.

(82) Cheng, C.; Yang, Z.; Wei, J. Simultaneous Size-and Phase-Controlled Synthesis of Metal Oxide Nanocrystals through Esterification Reactions. **2021**, *37*, 46. https://doi.org/10.1021/acs.cgd.1c00439.

(83) Sanchez-Lievanos, K. R.; Tariq, M.; Brennessel, W. W.; Knowles, K. E. Heterometallic Trinuclear Oxo-Centered Clusters as Single-Source Precursors for Synthesis of Stoichiometric Monodisperse Transition Metal Ferrite Nanocrystals. **2020**, *49*, 16348. https://doi.org/10.1039/d0dt01369b.

(84) Micha, J. S.; Dieny, B.; Régnard, J. R.; Jacquot, J. F.; Sort, J. Estimation of the Co Nanoparticles Size by Magnetic Measurements in Co/SiO2 Discontinuous Multilayers. *Journal of Magnetism and Magnetic Materials* **2004**, *272–276* (SUPPL. 1), E967–E968. https://doi.org/10.1016/J.JMMM.2003.12.268.

(85) Bruvera, I. J.; Mendoza Zélis, P.; Calatayud, M. P. Determination of the Blocking Temperature of Magnetic Nanoparticles: The Good, the Bad, and the Ugly. *J. Appl. Phys* **2015**, *118*, 184304. https://doi.org/10.1063/1.4935484.

(86) Kiss, L. B.; Niklasson, G. A.; Granqvist, C. G. *New Approach to the Origin of Lognormal Size Distributions of Nanoparticles* *; 1999; Vol. 10.

(87) Rondinone, A. J.; Samia, A. C. S.; Zhang, Z. J. Characterizing the Magnetic Anisotropy constant of Spinel Cobalt Ferrite Nanoparticles. *Appl. Phys. Lett* **2000**, *76*, 3624. https://doi.org/10.1063/1.126727.

(88) Hou, Y.; Gao, S. Monodisperse Nickel Nanoparticles Prepared from a Monosurfactant System and Their Magnetic Properties{. *J. Mater. Chem* **2003**, *13*, 1510–1512. https://doi.org/10.1039/b303226d.

(89) Vopson, M. M. Fundamentals of Multiferroic Materials and Their Possible Applications. *http://dx.doi.org/10.1080/10408436.2014.992584* **2015**, *40* (4), 223–250. https://doi.org/10.1080/10408436.2014.992584.

(90) Yang, Z.; Nakajima, K.; Onodera, R.; Tayama, T.; Chiba, D.; Narita, F. Magnetostrictive Clad Steel Plates for High-Performance Vibration Energy Harvesting. *Applied Physics Letters* **2018**, *112* (7), 073902. https://doi.org/10.1063/1.5016197.

(91) Apicella, V.; Clemente, C. S.; Davino, D.; Leone, D.; Visone, C. Magneto-Mechanical Optimization and Analysis of a Magnetostrictive Cantilever Beam for Energy Harvesting. *Journal of Magnetism and Magnetic Materials* **2019**, *475*, 401–407. https://doi.org/10.1016/J.JMMM.2018.11.076.

(92) Cao, S.; Wang, X.; Zheng, J.; Cao, S.; Sun, J.; Wang, Z.; Zhang, C. Modeling and Design of an Efficient Magnetostrictive Energy Harvesting System With Low Voltage and Low Power; Modeling and Design of an Efficient Magnetostrictive Energy Harvesting System With Low Voltage and Low Power. *IEEE Transactions on Magnetics* **2018**, *54* (11). https://doi.org/10.1109/TMAG.2018.2831000.

(93) Gou, J.; Ma, T.; Liu, X.; Zhang, C.; Sun, L.; Sun, G.; Xia, W.; Ren, X. Large and Sensitive Magnetostriction in Ferromagnetic Composites with Nanodispersive Precipitates. *NPG Asia Materials 2021 13:1* **2021**, *13* (1), 1–13. https://doi.org/10.1038/s41427-020-00276-7.

(94) Chen, Q. N.; Ma, F.; Xie, S.; Liu, Y.; Proksch, R.; Li, J. High Sensitivity Piezomagnetic Force Microscopy for Quantitative Probing of Magnetic Materials at the Nanoscale. *Nanoscale* **2013**, *5* (13), 5747–5751. https://doi.org/10.1039/C3NR00770G.
(95) Sun, N. X.; Srinivasan, G. Voltage Control of Magnetism in Multiferroic Heterostructures and Devices. *http://dx.doi.org/10.1142/S2010324712400048* **2013**, *2* (3). https://doi.org/10.1142/S2010324712400048.
(96) Gao, C.; Zeng, Z.; Peng, S.; Shuai, C. Magnetostrictive Alloys: Promising Materials for Biomedical Applications. *Bioactive Materials* **2022**, *8*, 177–195. https://doi.org/10.1016/J.BIOACTMAT.2021.06.025.
(97) Hart, S.; Bucio, R.; Dapino, M. Magnetostrictive Actuation of a Bone Loading Composite for Accelerated Tissue Formation. *Smart Materials Research* **2012**, *2012*, 1–7. https://doi.org/10.1155/2012/258638.
(98) Moffett, M. B.; Clark, A. E.; Wun-Fogle, M.; Linberg, J.; Teter, J. P.; McLaughlin, E. A. Characterization of Terfenol-D for Magnetostrictive Transducers. *The Journal of the Acoustical Society of America* **1999**, *89* (3), 1448. https://doi.org/10.1121/1.400678.
(99) Iida, S. Magnetostriction Constants of Rare Earth Iron Garnets. *http://dx.doi.org/10.1143/JPSJ.22.1201* **2013**, *22* (5), 1201–1209. https://doi.org/10.1143/JPSJ.22.1201.
(100) Chaudhury, R. P.; Lorenz, B.; Sun, Y. Y.; Bezmaternykh, L. N.; Temerov, V. L.; Chu, C. W. Magnetoelectricity and Magnetostriction Due to the Rare-Earth Moment in TmAl 3 (BO 3) 4. *PHYSICAL REVIEW B 81*. https://doi.org/10.1103/PhysRevB.81.220402.
(101) Cullen, J. R.; Clark, A. E. Magnetostriction and Structural Distortion in Rare-Earth Intermetallics. *Physical Review B* **1977**, *15* (9), 4510. https://doi.org/10.1103/PhysRevB.15.4510.
(102) Jiles, D. C. The Development of Highly Magnetostrictive Rare Earth-Iron Alloys. *Journal of Physics D: Applied* **1994**, *27* (1), 1–11. https://doi.org/10.1088/0022-3727/27/1/001.
(103) Zamborini, F. P.; Alphenaar, B. W.; Kharel, P. L.; Jayne, K. D.; Hatchett, D.; Boutin, K. Soviet Physics Uspekhi REVIEWS OF TOPICAL PROBLEMS Giant Magnetostriction. *3 Sov. Phys. Usp* **1983**, *140*, 271–313.
(104) Wang, Y.; Ren, W. J.; Yang, Y. H.; Li, B.; Li, J.; Zhang, Z. D. Magnetostrictive Properties of the Heavy-Rare-Earth-Free Sm1-XNdxFe2 Compounds. *Journal of Applied Physics* **2013**, *113* (14), 143903. https://doi.org/10.1063/1.4801340.
(105) Wang, J.; Dong, C.; Wei, Y.; Lin, X.; Athey, B.; Chen, Y.; Winter, A.; Stephen, G. M.; Heiman, D.; He, Y.; Chen, H.; Liang, X.; Yu, C.; Zhang, Y.; Podlaha-Murphy, E. J.; Zhu, M.; Wang, X.; Ni, J.; Mcconney, M.; Jones, J.; Page, M.; Mahalingam, K.; Sun, N. X. Magnetostriction, Soft Magnetism, and Microwave Properties in Co-Fe-C Alloy Films. *Physical Review Applied* **2019**, *10*, 34011. https://doi.org/10.1103/PhysRevApplied.12.034011.
(106) Dai, G.; Xing, X.; Shen, Y.; -, al; He, W.; Huang, H.; Koo, B.; Bader, K.; Burkhardt, U. A Review of Magnetostrictive Iron–Gallium Alloys. *Smart Materials and Structures* **2011**, *20* (4), 043001. https://doi.org/10.1088/0964-1726/20/4/043001.
(107) Kellogg, R. A.; Russell, A. M.; Lograsso, T. A.; Flatau, A. B.; Clark, A. E.; Wun-Fogle, M. Tensile Properties of Magnetostrictive Iron–Gallium Alloys. *Acta Materialia* **2004**, *52* (17), 5043–5050. https://doi.org/10.1016/J.ACTAMAT.2004.07.007.
(108) Clark, A. E.; Restorff, J. B.; Wun-Fogle, M.; Lograsso, T. A.; Schlagel, D. L. Magnetostrictive Properties of Body-Centered Cubic Fe-Ga and Fe-Ga-Al Alloys. *IEEE Transactions on Magnetics* **2000**, *36* (5 I), 3238–3240. https://doi.org/10.1109/20.908752.

(109) Datta, S.; Atulasimha, J.; Flatau, A. B. Figures of Merit of Magnetostrictive Single Crystal Iron–Gallium Alloys for Actuator and Sensor Applications. *Journal of Magnetism and Magnetic Materials* **2009**, *321* (24), 4017–4031. https://doi.org/10.1016/J.JMMM.2009.07.067.
(110) Clark, A. E.; Hathaway, K. B.; Wun-Fogle, M.; Restorff, J. B.; Lograsso, T. A.; Keppens, V. M.; Petculescu, G.; Taylor, R. A. Extraordinary Magnetoelasticity and Lattice Softening in Bcc Fe-Ga Alloys. *Journal of Applied Physics* **2003**, *93* (10), 8621. https://doi.org/10.1063/1.1540130.
(111) Kumar, A.; Sundararaghavan, V. Simulation of Magnetostrictive Properties of Galfenol under Thermomechanical Deformation. *Finite Elements in Analysis and Design* **2017**, *127*, 1–5. https://doi.org/10.1016/J.FINEL.2016.11.009.
(112) Zhang, Y. N.; Cao, J. X.; Wu, R. Q. Rigid Band Model for Prediction of Magnetostriction of Iron-Gallium Alloys. *Appl. Phys. Lett* **2010**, *96*, 62508. https://doi.org/10.1063/1.3318420.
(113) Wang, H.; Zhang, Y. N.; Wu, R. Q.; Sun, L. Z.; Xu, D. S.; Zhang, Z. D. Understanding Strong Magnetostriction in Fe 1002x Ga x Alloys. https://doi.org/10.1038/srep03521.
(114) Lograsso, T. A.; Summers, E. M. Detection and Quantification of D03 Chemical Order in Fe–Ga Alloys Using High Resolution X-Ray Diffraction. *Materials Science and Engineering: A* **2006**, *416* (1–2), 240–245. https://doi.org/10.1016/J.MSEA.2005.10.035.
(115) Meisenheimer, P. B.; Steinhardt, R. A.; Sung, S. H.; Williams, L. D.; Zhuang, S.; Nowakowski, M. E.; Novakov, S.; Torunbalci, M. M.; Prasad, B.; Zollner, C. J.; Wang, Z.; Dawley, N. M.; Schubert, J.; Hunter, A. H.; Manipatruni, S.; Nikonov, D. E.; Young, I. A.; Chen, L. Q.; Bokor, J.; Bhave, S. A.; Ramesh, R.; Hu, J. M.; Kioupakis, E.; Hovden, R.; Schlom, D. G.; Heron, J. T. Engineering New Limits to Magnetostriction through Metastability in Iron-Gallium Alloys. *Nature Communications 2021 12:1* **2021**, *12* (1), 1–8. https://doi.org/10.1038/s41467-021-22793-x.
(116) Laver, M.; Mudivarthi, C.; Cullen, J. R.; Flatau, A. B.; Chen, W.-C.; Watson, S. M.; Wuttig, M. Magnetostriction and Magnetic Heterogeneities in Iron-Gallium. https://doi.org/10.1103/PhysRevLett.105.027202.
(117) Khachaturyan, A. G.; Viehland, D. Structurally Heterogeneous Model of Extrinsic Magnetostriction for Fe-Ga and Similar Magnetic Alloys: Part II. Giant Magnetostriction and Elastic Softening. https://doi.org/10.1007/s11661-007-9252-0.
(118) Golovin, I. S.; Balagurov, A. M.; Palacheva, V. v.; Bobrikov, I. A.; Zlokazov, V. B. In Situ Neutron Diffraction Study of Bulk Phase Transitions in Fe-27Ga Alloys. *Materials & Design* **2016**, *98*, 113–119. https://doi.org/10.1016/J.MATDES.2016.03.016.
(119) Steiner, J.; Pokharel, S.; Lisfi, A.; Fleischer, J.; Wyrough, P.; Salamanca-Riba, L.; Cumings, J.; Wuttig, M. R.; Steiner, J.; Fleischer, J.; Wyrough, P.; Salamanca-Riba, L.; Cumings, J.; Wuttig, M. R.; Pokharel, S.; Lisfi, A. Transformation-Induced Magnetoelasticity in FeGa Alloys. *Advanced Engineering Materials* **2019**, *21* (10), 1900399. https://doi.org/10.1002/ADEM.201900399.
(120) Boisse, J.; Zapolsky, H.; Khachaturyan, A. G. Atomic-Scale Modeling of Nanostructure Formation in Fe–Ga Alloys with Giant Magnetostriction: Cascade Ordering and Decomposition. *Acta Materialia* **2011**, *59* (7), 2656–2668. https://doi.org/10.1016/J.ACTAMAT.2011.01.002.
(121) He, Y.; Ke, X.; Jiang, C.; Miao, N.; Wang, H.; Michael David Coey, J.; Wang, Y.; Xu, H.; He, Y. K.; Jiang, C. B.; Miao, N. H.; Wang, H.; D Coey, J. M.; Xu, H. B.; Ke, X. Q.; Wang, Y. Z. Interaction of Trace Rare-Earth Dopants and Nanoheterogeneities Induces Giant Magnetostriction in Fe-Ga Alloys. *Advanced Functional Materials* **2018**, *28* (20), 1800858. https://doi.org/10.1002/ADFM.201800858.

(122) Barua, R.; Taheri, P.; Chen, Y.; Koblischka-Veneva, A.; Koblischka, M. R.; Jiang, L.; Harris, V. G. Giant Enhancement of Magnetostrictive Response in Directionally-Solidified Fe83Ga17Erx Compounds. *Materials* **2018**, *11* (6). https://doi.org/10.3390/MA11061039.
(123) Stadler, B. J. H. Controlled Electrochemical Synthesis Of Giant Magnetostrictive Iron-Gallium Alloy Thin Films And Nanowires. **2012**.
(124) Adolphi, B.; McCord, J.; Bertram, M.; Oertel, C. G.; Merkel, U.; Marschner, U.; Schäfer, R.; Wenzel, C.; Fischer, W. J. Improvement of Sputtered Galfenol Thin Films for Sensor Applications. *Smart Materials and Structures* **2010**, *19* (5), 055013. https://doi.org/10.1088/0964-1726/19/5/055013.
(125) Basantkumar, R. R.; Hills Stadler, B. J.; Robbins, W. P.; Summers, E. M. Integration of Thin-Film Galfenol With MEMS Cantilevers for Magnetic Actuation. *IEEE TRANSACTIONS ON MAGNETICS* **2006**, *42* (10). https://doi.org/10.1109/TMAG.2006.879666.
(126) Estrine, E. C.; Hein, M.; Robbins, W. P. Composition and Crystallinity in Electrochemically Deposited Magnetostrictive Galfenol (FeGa). *J. Appl. Phys* **2014**, *115*, 17–918. https://doi.org/10.1063/1.4865318.
(127) Kay, R. W.; Hoyd-Gigg Ng, J.; Popov, C.; Record, P.; Y Desmulliez, M. P. *Electrochemical Deposition of Galfenol*; 2012. https://doi.org/10.1109/EMAP.2012.6507838.
(128) Estrine, E. C.; Robbins, W. P.; Maqableh, M. M.; Stadler, B. J. H. Electrodeposition and Characterization of Magnetostrictive Galfenol (FeGa) Thin Films for Use in Microelectromechanical Systems. *Journal of Applied Physics* **2013**, *113* (17), 17A937. https://doi.org/10.1063/1.4799775.
(129) Zhou, B.; Li, X.; -, al; Liu, Y.; Zhang, X.; -Combinatorial Electrodeposition of Magnetostrictive Fe, al; Patrick McGary, G. D.; SaiMadhukar Reddy, K.; Haugstad, G. D.; Pohl, D.; Damm, C.; Schultz, L.; Schlörb, H. TEM Investigations on the Local Microstructure of Electrodeposited Galfenol Nanowires. *Nanotechnology* **2015**, *27* (3), 035705. https://doi.org/10.1088/0957-4484/27/3/035705.
(130) Zhang, Z.; Sang, L.; Huang, J.; Wang, L.; Koizumi, S.; Liao, M. Tailoring the Magnetic Properties of Galfenol Film Grown on Single-Crystal Diamond. *Journal of Alloys and Compounds* **2021**, *858*, 157683. https://doi.org/10.1016/J.JALLCOM.2020.157683.
(131) Budhathoki, S.; Sapkota, A.; Law, K. M.; Nepal, B.; Ranjit, S.; KC, S.; Mewes, T.; Hauser, A. J. Low Gilbert Damping and Linewidth in Magnetostrictive FeGa Thin Films. *Journal of Magnetism and Magnetic Materials* **2020**, *496*, 165906. https://doi.org/10.1016/J.JMMM.2019.165906.
(132) Guevara De Jesus, M.; Xiao, Z.; Goiriena-Goikoetxea, M.; Chopdekar, R. v; Panduranga, M. K.; Shirazi, P.; Acosta, A.; Chang, J. P.; Bokor, J.; Carman, G. P.; Candler, R. N.; Lynch, C. Magnetic State Switching in FeGa Microstructures. **2021**. https://doi.org/10.1088/1361.
(133) Acosta, A.; Fitzell, K.; Schneider, J. D.; Dong, C.; Yao, Z.; Sheil, R.; Wang, Y. E.; Carman, G. P.; Sun, N. X.; Chang, J. P. Underlayer Effect on the Soft Magnetic, High Frequency, and Magnetostrictive Properties of FeGa Thin Films. *Journal of Applied Physics* **2020**, *128* (1), 013903. https://doi.org/10.1063/5.0011873.
(134) Livesey, K. L.; Ruta, S.; Anderson, N. R.; Baldomir, D.; Chantrell, R. W.; Serantes, D. Beyond the Blocking Model to Fit Nanoparticle ZFC/FC Magnetisation Curves. *Scientific Reports 2018 8:1* **2018**, *8* (1), 1–9. https://doi.org/10.1038/s41598-018-29501-8.
(135) Lacroix, L.-M.; Lachaize, S.; Falqui, A. Ultrasmall Iron Nanoparticles: Effect of Size Reduction on Anisotropy and Magnetization ARTICLES YOU MAY BE INTERESTED IN. *J. Appl. Phys* **2008**, *103*, 7–521. https://doi.org/10.1063/1.2837625.

(136) Chen, Y.; Fu, Z.; Wu, Y.; Xu, Y.; Xiao, Y.; Wang, J.; Zhang, R.; Jiang, C. Giant Heterogeneous Magnetostriction Induced by Charge Accumulation-Mediated Nanoinclusion Formation in Dual-Phase Nanostructured Systems. *Acta Materialia* **2021**, *213*, 116975. https://doi.org/10.1016/J.ACTAMAT.2021.116975.
(137) Tsoukalas, D. From Silicon to Organic Nanoparticle Memory Devices. *Trans. R. Soc. A* **2009**, *367*, 4169–4179. https://doi.org/10.1098/rsta.2008.0280.
(138) Gandhi, A. C.; Pradeep, R.; Yeh, Y.-C.; Li, T.-Y.; Wang, C.-Y.; Hayakawa, Y.; Wu, S. Y. Understanding the Magnetic Memory Effect in Fe-Doped NiO Nanoparticles for the Development of Spintronic Devices. **2018**. https://doi.org/10.1021/acsanm.8b01898.
(139) Sun, S.; Murray, C. B.; Weller, D.; Folks, L.; Moser, A. Monodisperse FePt Nanoparticles and Ferromagnetic FePt Nanocrystal Superlattices. *Science* **2000**, *287* (5460), 1989–1992. https://doi.org/10.1126/SCIENCE.287.5460.1989.
(140) Farahmandjou, M. The Effect of 1, 2- Hexadecadeniol and LiBEt3H Superhydride on the Size of FePt Nanoparticles. *AIP Conference Proceedings* **2011**, *1415* (1), 193. https://doi.org/10.1063/1.3667254.
(141) Hayashi, Y.; Ogawa, T.; Ishiyama, K. Preparation and Characterization of SiO 2-Coated Submicron-Sized L1 0 Fe-Pt Particles. *AIP Advances* **2018**, *8*, 56416. https://doi.org/10.1063/1.5006376.
(142) Shima, T.; Moriguchi, T.; Mitani, S.; Takanashi, K. Low-Temperature Fabrication of L10 Ordered FePt Alloy by Alternate Monatomic Layer Deposition. *Applied Physics Letters* **2002**, *80* (2), 288. https://doi.org/10.1063/1.1432446.
(143) Wittig, J. E.; Bentley, J.; Allard, L. F.; Bentley, J. In Situ Investigation of Ordering Phase Transformations in FePt Magnetic Nanoparticles. *Ultramicroscopy* **2017**, *176*, 218–232. https://doi.org/10.1016/J.ULTRAMIC.2016.11.025.
(144) Yang, Y.; Song, B.; Ke, X.; Xu, F.; Bozhilov, K. N.; Hu, L.; Shahbazian-Yassar, R.; Zachariah, M. R. Aerosol Synthesis of High Entropy Alloy Nanoparticles. *Langmuir* **2020**, *36*, 10. https://doi.org/10.1021/acs.langmuir.9b03392.
(145) Yao, Y.; Huang, Z.; Xie, P.; Lacey, S. D.; Jacob, R. J.; Xie, H.; Chen, F.; Nie, A.; Pu, T.; Rehwoldt, M.; Yu, D.; Zachariah, M. R.; Wang, C.; Shahbazian-Yassar, R.; Li, J.; Hu, L. Carbothermal Shock Synthesis of High-Entropy-Alloy Nanoparticles. *Science* **2018**, *359*, 1489–1494.
(146) Guo, H.; Li, H.; Jarvis, K.; Wan, H.; Kunal, P.; Dunning, S. G.; Liu, Y.; Henkelman, G.; Humphrey, S. M. Microwave-Assisted Synthesis of Classically Immiscible Ag−Ir Alloy Nanoparticle Catalysts. **2022**, *12*, 36. https://doi.org/10.1021/acscatal.8b02103.
(147) Pacchioni, G. High-Entropy Materials Go Nano. *Nature Reviews Materials 2022 7:3* **2022**, *7* (3), 156–156. https://doi.org/10.1038/s41578-022-00429-w.
(148) Zheng, H.; Luo, G.; Zhang, A.; Lu, X.; He, L. The Synthesis and Catalytic Applications of Nanosized High-Entropy Alloys. *ChemCatChem* **2021**, *13* (3), 806–817. https://doi.org/10.1002/CCTC.202001163.
(149) Heuer-Jungemann, A.; Feliu, N.; Bakaimi, I.; Hamaly, M.; Alkilany, A.; Chakraborty, I.; Masood, A.; Casula, M. F.; Kostopoulou, A.; Oh, E.; Susumu, K.; Stewart, M. H.; Medintz, I. L.; Stratakis, E.; Parak, W. J.; Kanaras, A. G. The Role of Ligands in the Chemical Synthesis and Applications of Inorganic Nanoparticles. *Chemical Reviews* **2019**, *119* (8), 4819–4880. https://doi.org/10.1021/ACS.CHEMREV.8B00733/ASSET/IMAGES/ACS.CHEMREV.8B00733.SOCIAL.JPEG_V03.
(150) Bian, B.; Xia, W.; Du, J.; Zhang, J.; Liu, J. P.; Guo, Z.; Yan, A. Growth Mechanisms and Size Control of FePt Nanoparticles Synthesized Using Fe(CO)x (x < 5)-Oleylamine and

Platinum(II) Acetylacetonate. *Nanoscale* **2013**, *5* (6), 2454–2459. https://doi.org/10.1039/C3NR33602F.
(151) Vodyashkin, A. A.; Rizk, M. G. H.; Kezimana, P.; Kirichuk, A. A.; Stanishevskiy, Y. M. Application of Gold Nanoparticle-Based Materials in Cancer Therapy and Diagnostics. *ChemEngineering 2021, Vol. 5, Page 69* **2021**, *5* (4), 69. https://doi.org/10.3390/CHEMENGINEERING5040069.
(152) Cardoso, V. F.; Francesko, A.; Ribeiro, C.; Bañobre-López, M.; Martins, P.; Lanceros-Mendez, S. Advances in Magnetic Nanoparticles for Biomedical Applications. *Advanced Healthcare Materials* **2018**, *7* (5), 1700845. https://doi.org/10.1002/ADHM.201700845.
(153) Gul, S.; Khan, S. B.; Rehman, I. U.; Khan, M. A.; Khan, M. I. A Comprehensive Review of Magnetic Nanomaterials Modern Day Theranostics. *Frontiers in Materials* **2019**, *6*, 179. https://doi.org/10.3389/FMATS.2019.00179/BIBTEX.
(154) Mitchell, M. J.; Billingsley, M. M.; Haley, R. M.; Wechsler, M. E.; Peppas, N. A.; Langer, R. Engineering Precision Nanoparticles for Drug Delivery. *Nature Reviews Drug Discovery*. https://doi.org/10.1038/s41573-020-0090-8.
(155) Zhu, L. D.; Hiltunen, E.; Li, Z. Using Magnetic Materials to Harvest Microalgal Biomass: Evaluation of Harvesting and Detachment Efficiency. *https://doi.org/10.1080/09593330.2017.1415379* **2017**, *40* (8), 1006–1012. https://doi.org/10.1080/09593330.2017.1415379.
(156) Liu, P.; Wang, T.; Yang, Z.; Hong, Y.; Xie, X.; Hou, Y. Effects of Fe3O4 Nanoparticle Fabrication and Surface Modification on Chlorella Sp. Harvesting Efficiency. *Science of The Total Environment* **2020**, *704*, 135286. https://doi.org/10.1016/J.SCITOTENV.2019.135286.
(157) Monroe, J. G.; Kumari, S.; Fairley, J. D.; Walters, K. B.; Berg, M. J.; Thompson, S. M. On the Energy Harvesting and Heat Transfer Ability of a Ferro-Nanofluid Oscillating Heat Pipe. *International Journal of Heat and Mass Transfer* **2019**, *132*, 162–171. https://doi.org/10.1016/J.IJHEATMASSTRANSFER.2018.11.096.
(158) Gloag, L.; Mehdipour, M.; Chen, D.; Tilley, R. D.; Justin Gooding, J.; Gloag, L.; Mehdipour, M.; Chen, D.; Tilley, R. D.; Gooding, J. J. Advances in the Application of Magnetic Nanoparticles for Sensing. *Advanced Materials* **2019**, *31* (48), 1904385. https://doi.org/10.1002/ADMA.201904385.
(159) Khan, I.; Khalil, A.; Khanday, F.; Shemsi, A. M.; Qurashi, A.; Siddiqui, K. S. Synthesis, Characterization and Applications of Magnetic Iron Oxide Nanostructures. *Arabian Journal for Science and Engineering 2017 43:1* **2017**, *43* (1), 43–61. https://doi.org/10.1007/S13369-017-2835-1.
(160) Kim, S.; Kim, N.; Seo, J.; Park, J. E.; Song, E. H.; Choi, S. Y.; Kim, J. E.; Cha, S.; Park, H. H.; Nam, J. M. Nanoparticle-Based Computing Architecture for Nanoparticle Neural Networks. *Science Advances* **2020**, *6* (35). https://doi.org/10.1126/SCIADV.ABB3348/SUPPL_FILE/ABB3348_SM.PDF.
(161) Heiligtag, F. J.; Niederberger, M. The Fascinating World of Nanoparticle Research. *Materials Today* **2013**, *16* (7–8), 262–271. https://doi.org/10.1016/J.MATTOD.2013.07.004.
(162) MacFarlane, L. R.; Shaikh, H.; Garcia-Hernandez, J. D.; Vespa, M.; Fukui, T.; Manners, I. Functional Nanoparticles through π-Conjugated Polymer Self-Assembly. *Nature Reviews Materials 2020 6:1* **2020**, *6* (1), 7–26. https://doi.org/10.1038/s41578-020-00233-4.
(163) Shao, X.; Li, X.; Ma, J.; Zhang, R.; He, H. Terminal Hydroxyl Groups on Al2O3 Supports Influence the Valence State and Dispersity of Ag Nanoparticles: Implications for Ozone Decomposition. *ACS Omega* **2021**, *6* (16), 10715–10722. https://doi.org/10.1021/ACSOMEGA.1C00220.

(164) Ellis, C. E.; Fukui, T.; Cordoba, C.; Blackburn, A.; Manners, I. Towards Scalable, Low Dispersity, and Dimensionally Tunable 2D Platelets Using Living Crystallization-Driven Self-Assembly. *Polymer Chemistry* **2021**, *12* (25), 3650–3660. https://doi.org/10.1039/D1PY00571E.
(165) Fu, X.; Cai, J.; Zhang, X.; Li, W. di; Ge, H.; Hu, Y. Top-down Fabrication of Shape-Controlled, Monodisperse Nanoparticles for Biomedical Applications. *Advanced Drug Delivery Reviews* **2018**, *132*, 169–187. https://doi.org/10.1016/J.ADDR.2018.07.006.
(166) Muzzio, M.; Li, J.; Yin, Z.; Delahunty, I. M.; Xie, J.; Sun, S. Monodisperse Nanoparticles for Catalysis and Nanomedicine. *Nanoscale* **2019**, *11* (41), 18946–18967. https://doi.org/10.1039/C9NR06080D.
(167) Lee, J.; Lee, E. J.; Hwang, T. Y.; Kim, J.; Choa, Y. H. Anisotropic Characteristics and Improved Magnetic Performance of Ca–La–Co-Substituted Strontium Hexaferrite Nanomagnets. *Scientific Reports 2020 10:1* **2020**, *10* (1), 1–9. https://doi.org/10.1038/s41598-020-72608-0.
(168) Vorobiov, S.; Tomasova, D.; Girman, V.; You, H.; Čižmár, E.; Orendáč, M.; Komanicky, V. Optimization of the Magnetocaloric Effect in Arrays of Ni3Pt Nanomagnets. *Journal of Magnetism and Magnetic Materials* **2019**, *474*, 63–69. https://doi.org/10.1016/J.JMMM.2018.10.137.
(169) Moro, F.; Kaminski, D.; Tuna, F.; Whitehead, G. F. S.; Timco, G. A.; Collison, D.; Winpenny, R. E. P.; Ardavan, A.; Mc Innes, E. J. L. Coherent Electron Spin Manipulation in a Dilute Oriented Ensemble of Molecular Nanomagnets: Pulsed EPR on Doped Single Crystals. *Chemical Communications* **2013**, *50* (1), 91–93. https://doi.org/10.1039/C3CC46326E.
(170) Choi, J. H.; Kim, T. H.; Seo, J.; Kuk, Y.; Suh, M. S. In Situ Fabrication of Single-Crystal Fe Nanomagnet Arrays. *Applied Physics Letters* **2004**, *85* (15), 3235. https://doi.org/10.1063/1.1803622.
(171) Prabhakaran, D.; Boothroyd, A. T.; Coldea, R.; Helme, L. M.; Tennant, D. A. Magnetic Studies of Polycrystalline and Single-Crystal Na x CoO 2.
(172) Kudr, J.; Haddad, Y.; Richtera, L.; Heger, Z.; Cernak, M.; Adam, V.; Zitka, O. Magnetic Nanoparticles: From Design and Synthesis to Real World Applications. *Nanomaterials* **2017**, *7* (9). https://doi.org/10.3390/NANO7090243.
(173) Lisjak, D.; Mertelj, A. Anisotropic Magnetic Nanoparticles: A Review of Their Properties, Syntheses and Potential Applications. *Progress in Materials Science* **2018**, *95*, 286–328. https://doi.org/10.1016/J.PMATSCI.2018.03.003.
(174) Yang, H.; Vu, A. D.; Hallal, A.; Rougemaille, N.; Coraux, J.; Chen, G.; Schmid, A. K.; Chshiev, M. Anatomy and Giant Enhancement of the Perpendicular Magnetic Anisotropy of Cobalt–Graphene Heterostructures. *Nano Letters* **2015**, *16* (1), 145–151. https://doi.org/10.1021/ACS.NANOLETT.5B03392.
(175) Yao, Y. D.; Chen, Y. Y.; Tai, M. F.; Wang, D. H.; Lin, H. M. Magnetic Anisotropy Effects in Nano-Cluster Nickel Particles. *Materials Science and Engineering: A* **1996**, *217–218*, 281–285. https://doi.org/10.1016/S0921-5093(96)10326-9.
(176) Neugebauer, N.; Fabian, A.; Elm, M. T.; Hofmann, D. M.; Czerner, M.; Heiliger, C.; Klar, P. J. Investigation of the Dipole Interaction in and between Ordered Arrangements of Magnetic Nanoparticles. *Physical Review B* **2020**, *101* (10), 104409. https://doi.org/10.1103/PHYSREVB.101.104409/FIGURES/6/MEDIUM.
(177) Bender, P.; Wetterskog, E.; Honecker, D.; Fock, J.; Frandsen, C.; Moerland, C.; Bogart, L. K.; Posth, O.; Szczerba, W.; Gavilán, H.; Costo, R.; Fernández-Díaz, M. T.; González-Alonso, D.; Fernández Barquín, L.; Johansson, C. Dipolar-Coupled Moment Correlations in Clusters

of Magnetic Nanoparticles. *Physical Review B* **2018**, *98* (22), 224420. https://doi.org/10.1103/PHYSREVB.98.224420/FIGURES/7/MEDIUM.
(178) Blanco-Mantecón, M.; O'Grady, K. Interaction and Size Effects in Magnetic Nanoparticles. *Journal of Magnetism and Magnetic Materials* **2006**, *296* (2), 124–133. https://doi.org/10.1016/J.JMMM.2004.11.580.
(179) Belemuk, A.; Udalov, O.; Chtchelkatchev NM; Beloborodov, I. Competition of Magneto-Dipole, Anisotropy and Exchange Interactions in Composite Multiferroics. *Journal of Physical Condense Matter* **2016**, *28* (126001). https://doi.org/10.1088/0953-8984/28/12/126001.
(180) Jeong, H. S.; You, C. Y.; Suh, B. J.; Kim, K. P.; Jang, J.; Jeong, S.; Choi, J. H.; Koo, J. Two-Dimensional Superlattice-like Sheets of Superparamagnetic Graphene Oxide/Magnetic Nanoparticle Hybrids. *Journal of Nanoparticle Research* **2020**, *22* (7), 1–9. https://doi.org/10.1007/S11051-020-04910-X/FIGURES/5.
(181) Lewandowski, W.; Wójcik, M.; Gorecka, E.; Górecka, E. Metal Nanoparticles with Liquid-Crystalline Ligands: Controlling Nanoparticle Superlattice Structure and Properties. https://doi.org/10.1002/cphc.201301194.
(182) Micha, J. S.; Dieny, B.; Régnard, J. R.; Jacquot, J. F.; Sort, J. Estimation of the Co Nanoparticles Size by Magnetic Measurements in Co/SiO2 Discontinuous Multilayers. *Journal of Magnetism and Magnetic Materials* **2004**, *272–276* (SUPPL. 1), E967–E968. https://doi.org/10.1016/J.JMMM.2003.12.268.
(183) Kiss, L. B.; Niklasson, G. A.; Granqvist, C. G. *New Approach to the Origin of Lognormal Size Distributions of Nanoparticles **; 1999; Vol. 10.
(184) Goudarzi, M.; Mir, N.; Mousavi-Kamazani, M.; Bagheri, S.; Salavati-Niasari, M. PARTICLE SIZE CHARACTERIZATION OF NANOPARTICLES – A PRACTICALAPPROACH. *Iranian Journal of Materials Science and Engineering* **2011**, *8* (2), 48–56. https://doi.org/10.1038/srep32539.
(185) Bienert, R.; Emmerling, F.; Thünemann, A. F. The Size Distribution of "gold Standard" Nanoparticles. *Analytical and Bioanalytical Chemistry* **2009**, *395* (6), 1651–1660. https://doi.org/10.1007/S00216-009-3049-5/FIGURES/7.
(186) Medrano, J. J. A.; Aragón, F. F. H.; Leon-Felix, L.; Coaquira, J. A. H.; Rodríguez, A. F. R.; Faria, F. S. E. D. V.; Sousa, M. H.; Ochoa, J. C. M.; Morais, P. C. Evidence of Particle-Particle Interaction Quenching in Nanocomposite Based on Oleic Acid-Coated Fe3O4 Nanoparticles after over-Coating with Essential Oil Extracted from Croton Cajucara Benth. *Journal of Magnetism and Magnetic Materials* **2018**, *466*, 359–367. https://doi.org/10.1016/J.JMMM.2018.07.036.
(187) Virumbrales-Del Olmo, M.; Delgado-Cabello, A.; Andrada-Chacón, A.; Sánchez-Benítez, J.; Urones-Garrote, E.; Blanco-Gutiérrez, V.; Torralvo, M. J.; Sáez-Puche, R. Effect of Composition and Coating on the Interparticle Interactions and Magnetic Hardness of MFe 2 O 4 (M = Fe, Co, Zn) Nanoparticles. *Physical Chemistry Chemical Physics* **2017**, *19* (12), 8363–8372. https://doi.org/10.1039/C6CP08743D.
(188) Polichetti, M.; Modestino, M.; Galluzzi, A.; Pace, S.; Iuliano, M.; Ciambelli, P.; Sarno, M. Influence of Citric Acid and Oleic Acid Coating on the Dc Magnetic Properties of Fe3O4 Magnetic Nanoparticles. *Materials Today: Proceedings* **2020**, *20*, 21–24. https://doi.org/10.1016/J.MATPR.2019.08.152.
(189) Morales, F.; Márquez, G.; Sagredo, V.; Torres, T. E.; Denardin, J. C. Structural and Magnetic Properties of Silica-Coated Magnetite Nanoaggregates. *Physica B: Condensed Matter* **2019**, *572*, 214–219. https://doi.org/10.1016/J.PHYSB.2019.08.007.

(190) Muscas, G.; Peddis, D.; Cobianchi, M.; Lascialfari, A.; Cannas, C.; Musinu, A.; Omelyanchik, A.; Rodionova, V.; Fiorani, D.; Mameli, V. Magnetic Interactions Versus Magnetic Anisotropy in Spinel Ferrite Nanoparticles. *IEEE Magnetics Letters* **2019**, *10*. https://doi.org/10.1109/LMAG.2019.2956908.
(191) Aslibeiki, B.; Kameli, P.; Salamati, H.; Concas, G.; Fernandez, M. S.; Talone, A.; Muscas, G.; Peddis, D. Co-Doped MnFe2O4 Nanoparticles: Magnetic Anisotropy and Interparticle Interactions. *Beilstein Journal of Nanotechnology 10:86* **2019**, *10* (1), 856–865. https://doi.org/10.3762/BJNANO.10.86.
(192) Franco, A.; Zapf, V. Temperature Dependence of Magnetic Anisotropy in Nanoparticles of CoxFe(3−x)O4. *Journal of Magnetism and Magnetic Materials* **2008**, *320* (5), 709–713. https://doi.org/10.1016/J.JMMM.2007.08.009.
(193) Sharifi Dehsari, H.; Asadi, K. Impact of Stoichiometry and Size on the Magnetic Properties of Cobalt Ferrite Nanoparticles. **2018**. https://doi.org/10.1021/acs.jpcc.8b09276.
(194) Inoue, J. I.; Yanagihara, H.; Kita, E. Magnetic Anisotropy and Magnetostriction in Cobalt-Ferrite with Lattice Deformation. *Materials Research Express* **2014**, *1* (4), 046106. https://doi.org/10.1088/2053-1591/1/4/046106.
(195) Zener, C. Classical Theory of the Temperature Dependence of Magnetic Anisotropy Energy".
(196) Yoon, S.; Krishnan, K. M. Temperature Dependence of Magnetic Anisotropy Constant in Manganese Ferrite Nanoparticles at Low Temperature. *J. Appl. Phys* **2011**, *109*, 7–534. https://doi.org/10.1063/1.3563068.
(197) Yoon, S. Temperature Dependence of Magnetic Anisotropy Constant in Cobalt Ferrite Nanoparticles. *Journal of Magnetism and Magnetic Materials* **2012**, *324* (17), 2620–2624. https://doi.org/10.1016/J.JMMM.2012.03.019.
(198) Wang, J.; Duan, H.; Lin, X.; Aguilar, V.; Mosqueda, A.; Zhao, G. M. Temperature Dependence of Magnetic Anisotropy Constant in Iron Chalcogenide Fe3Se4: Excellent Agreement with Theories. *Journal of Applied Physics* **2012**, *112* (10), 103905. https://doi.org/10.1063/1.4759352.
(199) Lu, L. T.; Dung, N. T.; Tung, L. D.; Thanh, C. T.; Quy, O. K.; Chuc, N. v; Maenosono, S.; Thanh, N. T. K. Synthesis of Magnetic Cobalt Ferrite Nanoparticles with Controlled Morphology, Monodispersity and Composition: The Influence of Solvent, Surfactant, Reductant and Synthetic Conditions. *Nanoscale* **2015**, *7*, 19596. https://doi.org/10.1039/c5nr04266f.
(200) Hou, Y.; Gao, S. Monodisperse Nickel Nanoparticles Prepared from a Monosurfactant System and Their Magnetic Properties. *Journal of Materials Chemistry* **2003**, *13* (7), 1510–1512. https://doi.org/10.1039/B303226D.
(201) Rondinone, A. J.; Samia, A. C. S.; Zhang, Z. J. Characterizing the Magnetic Anisotropy Constant of Spinel Cobalt Ferrite Nanoparticles. *Appl. Phys. Lett* **2000**, *76*, 3624. https://doi.org/10.1063/1.126727.
(202) Santos, P. J.; Macfarlane, R. J. Reinforcing Supramolecular Bonding with Magnetic Dipole Interactions to Assemble Dynamic Nanoparticle Superlattices. *Journal of the American Chemical Society* **2020**, *142* (3), 1170–1174. https://doi.org/10.1021/JACS.9B11476/SUPPL_FILE/JA9B11476_SI_001.PDF.
(203) Morales, F.; Márquez, G.; Sagredo, V.; Torres, T. E.; Denardin, J. C. Structural and Magnetic Properties of Silica-Coated Magnetite Nanoaggregates. *Physica B: Condensed Matter* **2019**, *572*, 214–219. https://doi.org/10.1016/J.PHYSB.2019.08.007.
(204) Polichetti, M.; Modestino, M.; Galluzzi, A.; Pace, S.; Iuliano, M.; Ciambelli, P.; Sarno, M. Influence of Citric Acid and Oleic Acid Coating on the Dc Magnetic Properties of Fe3O4

Magnetic Nanoparticles. *Materials Today: Proceedings* **2020**, *20*, 21–24. https://doi.org/10.1016/J.MATPR.2019.08.152.
(205) Maaz, K.; Karim, S.; Lee, K. J.; Jung, M. H.; Kim, G. H. Effect of Temperature on the Magnetic Characteristics of Ni0.5Co0.5Fe2O4 Nanoparticles. *MATERIALS CHEMISTRY AND PHYSICS* **2012**, *133* (2–3), 1006–1010. https://doi.org/10.1016/J.MATCHEMPHYS.2012.02.007.
(206) Maaz, K.; Mumtaz, A.; Hasanain, S. K.; Bertino, M. F. Temperature Dependent Coercivity and Magnetization of Nickel Ferrite Nanoparticles. *Journal of Magnetism and Magnetic Materials* **2010**, *322* (15), 2199–2202. https://doi.org/10.1016/J.JMMM.2010.02.010.
(207) Zhang, D.; Klabunde, K. J.; Sorensen, C. M.; Hadjipanayis, G. C. Magnetization Temperature Dependence in Iron Nanoparticles.
(208) Peddis, D.; Orrù, F.; Ardu, A.; Cannas, C.; Musinu, A.; Piccaluga, G. Interparticle Interactions and Magnetic Anisotropy in Cobalt Ferrite Nanoparticles: Influence of Molecular Coating. *Chemistry of Materials* **2012**, *24* (6), 1062–1071. https://doi.org/10.1021/CM203280Y/SUPPL_FILE/CM203280Y_SI_001.PDF.
(209) Tung, L. D.; Kolesnichenko, V.; Caruntu, D.; Chou, N. H.; O'Connor, C. J.; Spinu, L. Magnetic Properties of Ultrafine Cobalt Ferrite Particles. *Journal of Applied Physics* **2003**, *93* (10), 7486. https://doi.org/10.1063/1.1540145.
(210) Singh, J.; Patel, T.; Kaurav, N.; Determinations, N.; Okram, G. S. Synthesis and Magnetic Properties of Nickel Nanoparticles. *Journal of Applied Physics* **2016**, *1731*, 103913. https://doi.org/10.1063/1.4947690.
(211) Mckeever, C.; Ogrin, F. Y.; Aziz, M. M.; Pérez, N.; Guardia, P.; Roca, A. G.; Morales, M. P.; Serna, C. J.; Iglesias, O.; Bartolomé, F.; García, L. M.; Batlle, X.; Labarta, A. Surface Anisotropy Broadening of the Energy Barrier Distribution in Magnetic Nanoparticles . *IOP PUBLISHING NANOTECHNOLOGY Nanotechnology* **2008**, *19*, 8. https://doi.org/10.1088/0957-4484/19/47/475704.
(212) Vivas, L. G.; Escrig, J.; Trabada, D. G.; Badini-Confalonieri, G. A.; Vázquez, M. Magnetic Anisotropy in Ordered Textured Co Nanowires. *Applied Physics Letters* **2012**, *100* (25), 252405. https://doi.org/10.1063/1.4729782.
(213) Kumar, A.; Fähler, S.; Schlörb, H.; Leistner, K.; Schultz, L. Competition between Shape Anisotropy and Magnetoelastic Anisotropy in Ni Nanowires Electrodeposited within Alumina Templates. *Physical Review B - Condensed Matter and Materials Physics* **2006**, *73* (6), 064421. https://doi.org/10.1103/PHYSREVB.73.064421/FIGURES/5/MEDIUM.
(214) Osaorn, J. A. Demagnetizing Factors of the General Ellipsoid. *Phys. Rev.* **1945**, *67* (11–12), 351–357.
(215) Santos, P. J.; Macfarlane, R. J. Reinforcing Supramolecular Bonding with Magnetic Dipole Interactions to Assemble Dynamic Nanoparticle Superlattices. *Journal of the American Chemical Society* **2020**, *142* (3), 1170–1174. https://doi.org/10.1021/JACS.9B11476/SUPPL_FILE/JA9B11476_SI_001.PDF.
(216) Bhagat, S. M.; Hirst, L. L.; Anderson, J. R. Ferromagnetic Resonance in Nickel and Iron . *Journal of Applied Physics* **1966**, *37*, 194. https://doi.org/10.1063/1.1707805.
(217) Talagala, P.; Fodor, P. S.; Naik, H. R.; Wenger, L. E.; Vaishnava, P. P.; Naik, V. M.; Fodor, P. S.; Haddad, D.; Naik, R.; Wenger, L. E. Determination of Magnetic Exchange Stiffness and Surface Determination of Magnetic Exchange Stiffness and Surface Anisotropy Constants in Epitaxial Ni_ {1-X} Co_ {x}(001) Films . **2002**. https://doi.org/10.1103/PhysRevB.66.144426.